

I. Impact Spallation Experiments:
Fracture Patterns and Spall Velocities
II. Craters in Carbonate Rocks:
An Electron Paramagnetic Resonance Analysis
of Shock Damage

Thesis by
Carol Ann Polanskey

In Partial Fulfillment of the Requirements
for the Degree of
Doctor of Philosophy

California Institute of Technology
Pasadena, California

1989

(submitted September 22, 1988)

(revised May 24, 1989)

*The following is dedicated to my parents, Walter and Mary Polansky,
my grandmother, Laura Gaul,
and
my friend, Maria Ines Etchegaray*

ACKNOWLEDGEMENTS

- *when you come right to it,
it's a lot easier to die
than it is to use your head.*
Robert A. Heinlein

I would like to thank my thesis advisor, Dr. Thomas Ahrens, for giving me a second chance many years ago when I really needed one. I am indebted to Dr. Jay Melosh, not only for publishing the theory which provided the framework for the first part of my dissertation, but more importantly for the support and encouragement he has given since the first day we met. I am also very grateful to my academic advisor, Dr. Donald Burnett for his gentle guidance and the little extras he threw my way.

My educational experience was greatly enhanced by the influence of Dr. Gene Shoemaker and Dr. Robert Sharp. Gene Shoemaker provided valuable help with the Meteor Crater project, but was an inspiration to me long before I arrived at Caltech. Bob Sharp introduced me to the wonders of California (giving the word "fieldtrip" a whole new meaning), while also indulging me in one of my favorite past times - singing around the campfire. Furthermore, I will never equal the experience he made possible for me at the lava lake on Hawaii. I would also like to acknowledge the remainder of the planetary science faculty for their tolerance of my graduate career, despite the torturous path it sometimes took. In particular, I would like to thank Dr. Andrew Ingersoll and Dr. David Stevenson for stepping in when the chips were down and helping me through the finals stages of my dissertation.

The shock wave lab is an immense operation and I am indebted to all of the people who work together to keep things running smoothly. A handful of these people include: the "senior students" in the lab, Jim Tuberczy, Mark Boslough, and Bob Svendsen; and the shock wave lab personnel: Papo Gelle, Mike Long, Chuck Manning,

and Leon Young. I particularly benefitted from Leon's insight and his experiences. I am also grateful to the wonderful people who were so cooperative in the machine shop, for instance: Bill Barber, Dick Wickes, and Gunther Haehn. I especially thank Dick for working above and beyond the call of duty on my experiments, as well as helping me fix my car and trusting me to use the lathe. Finally, I thank Sue Yamada, Kay Campbell and Donna Lathrop for being infinitely useful in dealing with all of the tricky administrative details.

I also thank some very helpful and personable people with which I interacted during my research on the Enewetak carbonates: Woody Henry, Dave Roddy, Colonel Robert Couch, and Byron Ristvet. Without their help, the research on OAK crater would have been impossible.

On a more personal note, I give a general thanks to my fellow students, friends and support network. I was very fortunate in being blessed with the world's two greatest officemates: Randy Kirk and Don Rudy. From day one, Randy was a constant source of assistance and support. My thanks (and amazement) also go to Randy for being able to find the answer to every question I ever asked – even if it took him a year. I am very grateful to Don, initially for his valliant efforts in pulling me through my oral exams, and in more recent months, for his \TeX expertise. In general, I thank Don for being the helpful kind of guy that he is. Outside of the office, I was also fortunate to have the aid and alliance of Howard Stone. I thank Howard foremost for forcing me to think and for standing in as resident EPR expert. Furthermore, I could not have survived all those late nights without our 4:00 am coffee breaks.

For their help during the final leg of my stint as a graduate student, I am eternally grateful to Maria Ines Etchegaray, Tim Dowling, and Kathy Pierce. Tim and Maria acted as “tag-team midwives” to the delivery of my thesis, while Kathy held down the

fort at home and patiently listened to me recount every gory detail of my progress. Two other kind souls who supported me during this time were Pamela Clark and Carlotta Glackin. I will never be able to thank all of these people enough for their endurance and their combined energy which carried me through the final eight months before my defense.

I give deep thanks Dr. Jacqueline Miles, Dr. Jan Aura and Steve Snyder for their valuable advice which enabled me to tackle and survive the demands of graduate student life. I am also grateful to Monica Hubbard, director of the women's glee club, for her understanding and for providing the opportunity for me to do *something* I knew I could do well. That also applies to all of my friends in the Occasional Consort who cheered me on while providing a delightful diversion from my work.

Finally, I must acknowledge the three people who early on influenced the career path I have chosen. The first is my cousin, Dr. Stan Cisowski, who began sending me NASA literature at a very early age. The second is Bruce Crocker who introduced me to oölitic chert as an undergraduate and consequently turned my head from physics towards geology. And the third is Dr. Peter Schultz whose contagious enthusiasm for experimental impact cratering sent me on to make craters of my own.

Carol A. Polanskey

TABLE OF CONTENTS

Acknowledgements	iv
Table of Contents	vii
Table of Figures	x
Table of Tables	xii
Abstract	xiv
1 Impact Spallation Experiments:	1
1.1 Introduction	5
1.2 Experimental Procedures	7
1.3 Results	12
1.3.1 Fractures in targets	15
1.3.2 Spall velocity measurements	16
1.4 Discussion	21
1.5 Summary and Conclusions	33
1.6 References	36
2 Craters in Carbonate Rocks:	39
2.1 Introduction	43

2.2	The EPR Spectrum of Mn^{2+} in Carbonates	45
2.2.1	Powdered calcite	45
2.2.2	Coralline limestone samples from OAK Crater	47
2.2.3	Kaibab dolomitic limestone samples from Meteor Crater	47
2.3	Sample Preparation and Spectrometer Measurements	48
2.4	Shock-wave calibration experiments	49
2.4.1	Description of shocked Solenhofen limestone spectra	52
2.4.2	Description of shocked Kaibab limestone spectra	55
2.5	Pressure calibration by differencing spectra	55
2.6	OAK Crater	63
2.6.1	Core sample selection	65
2.6.2	Results of core sample analysis	67
2.6.3	Results of the ejecta sample analysis	71
2.6.4	Interpretation of OAK Crater	73
2.7	Meteor Crater	75
2.7.1	Results of the Meteor Crater sample analysis	76
2.8	Summary	78
2.9	References	81

A	OAK Sample Descriptions, Results and Spectra	86
B	Meteor Crater Sample Descriptions, Results, and Spectra	114

TABLE OF FIGURES

1.1	Sketch of experimental configuration for spall velocity measurements	9
1.2	Three frames from the film of shot 840904	11
1.3	The ratio of t_{max} to l_{max} is plotted as a function of mass for each of the collected spall fragments.	13
1.4	Relationship between a corrected form of the displaced mass and the kinetic energy of the impact	14
1.5	Cross section of the target from shot 840904 illustrating the classification of internal fractures	17
1.6	Results of the spall velocity measurements for five experimental impacts	20
1.7	Sketch of an experimental crater profile	23
1.8	Illustration of the range in values of the two major variables (d and τ) for the present and some previous experiments.	25
1.9a	Sketches of the fractures found inside targets 840901, 840902, and 840904	26
1.9b	Sketches of the fractures found inside targets 840905, 840906, and 790837	27
1.9c	Sketches of the fractures found inside targets 790839, 840909, and 603	28
1.10	Vertical spall velocity is plotted as a function of s	32
2.1	EPR spectrum of powdered single-crystal calcite.	46
2.2	Hugoniot data for three carbonate rocks	51

2.3a	Comparison of Solenhofen limestone spectra shocked in the laboratory	53
2.3b	Comparison of Kaibab limestone spectra shocked in the laboratory . .	54
2.4	Example of the differencing technique	58
2.5a	Plot of the summed differences for the low and high field components of the Solenhofen limestone samples as a function of shock pressure. . .	59
2.5b	Plot of the summed differences for the low and high field components of the Kaibab dolomitic limestone samples as a function of shock pressure. . .	60
2.6	Location map of Enewetak Atoll and OAK crater	64
2.7	Map of OAK crater showing the location of the boreholes sampled in this study	66
2.8a	Results of the borehole sample analysis	69
2.8b	Results of the core sample analysis	70
2.9	Map of OAK crater showing ejecta recovery sites	72
2.10	Results of the OAK Crater ejecta sample analysis	74
2.11	Results of the Meteor Crater ejecta sample analysis	77
2.12	Particle velocity at the shock front, as a function of the position of the shock front as taken from Moss (1988)	79

TABLES

1.1	Experimental Parameters	8
1.2	Spall Fragment Dimensions	12
1.3	Spall Velocity Measurements	19
1.4	Rise Times and Depth of Burst	24
2.1	Shock Wave Data	52
2.2	Pressure and Integrated Difference Data for High-Resolution Spectra	62
A.1	Results for Borehole OAR-2A Samples	88
A.2	Results for Borehole OBZ-4 Samples	92
A.3	Results for Borehole OCT-5 Samples	96
A.4	Results for Borehole OET-7 Samples	100
A.5	Results for Borehole OFT-8 Samples	102
A.6	Results for Borehole OPZ-18 Samples	106
A.7	Results for OAK Debris Samples	111
B.1	Results for Diablo Canyon Samples	116
B.2	Results for Meteor Crater Wall Samples	118
B.3	Results for Meteor Crater Ejecta Samples	120

B.4 Results for Miscellaneous Meteor Crater Samples 123

ABSTRACT

This work is divided into two independent papers.

PAPER 1.

Spall velocities were measured for nine experimental impacts into San Marcos gabbro targets. Impact velocities ranged from 1 to 6.5 km/sec. Projectiles were iron, aluminum, lead, and basalt of varying sizes. The projectile masses ranged from a 4 g lead bullet to a 0.04 g aluminum sphere. The velocities of fragments were measured from high-speed films taken of the events. The maximum spall velocity observed was 30 m/sec, or 0.56 percent of the 5.4 km/sec impact velocity. The measured velocities were compared to the spall velocities predicted by the spallation model of Melosh (1984). The compatibility between the spallation model for large planetary impacts and the results of these small scale experiments are considered in detail.

The targets were also bisected to observe the pattern of internal fractures. A series of fractures were observed, whose location coincided with the boundary between rock subjected to the peak shock compression and a theoretical "near surface zone" predicted by the spallation model. Thus, between this boundary and the free surface, the target material should receive reduced levels of compressive stress as compared to the more highly shocked region below.

PAPER 2.

Carbonate samples from the nuclear explosion crater, OAK, and a terrestrial impact crater, Meteor Crater, were analyzed for shock damage using electron para-

magnetic resonance, EPR. The first series of samples for OAK Crater were obtained from six boreholes within the crater, and the second series were ejecta samples recovered from the crater floor. The degree of shock damage in the carbonate material was assessed by comparing the sample spectra to spectra of Solenhofen limestone, which had been shocked to known pressures.

The results of the OAK borehole analysis have identified a thin zone of highly shocked carbonate material underneath the crater floor. This zone has a maximum depth of approximately 200 ft below sea floor at the ground zero borehole and decreases in depth towards the crater rim. A layer of highly shocked material is also found on the surface in the vicinity of the reference borehole, located outside the crater. This material could represent a fallout layer. The ejecta samples have experienced a range of shock pressures.

It was also demonstrated that the EPR technique is feasible for the study of terrestrial impact craters formed in carbonate bedrock. The results for the Meteor Crater analysis suggest a slight degree of shock damage present in the β member of the Kaibab Formation exposed in the crater walls.

Paper 1

Impact Spallation Experiments: Fracture Patterns and Spall Velocities

IMPACT SPALLATION EXPERIMENTS:
FRACTURE PATTERNS AND SPALL VELOCITIES

Carol A. Polanskey and Thomas J. Ahrens
Division of Geological and Planetary Sciences
California Institute of Technology
Pasadena, California 91125

Submitted to *Icarus*

Contribution number 4405 from the Division of Geological and Planetary Sciences,
California Institute of Technology, Pasadena, California 91125

Abstract

Spall velocities were measured for nine experimental impacts into San Marcos gabbro targets. Impact velocities ranged from 1 to 6.5 km/sec. Projectiles were iron, aluminum, lead, and basalt of varying sizes. The projectile masses ranged from a 4 g lead bullet to a 0.04 g aluminum sphere. The velocities of fragments were measured from high-speed films taken of the events. The maximum spall velocity observed was 30 m/sec, or 0.56 percent of the 5.4 km/sec impact velocity. The measured velocities were compared to the spall velocities predicted by the spallation model of Melosh (1984). The compatibility between the spallation model for large planetary impacts and the results of these small-scale experiments are considered in detail.

The targets were also bisected to observe the pattern of internal fractures. A series of fractures were observed, whose location coincided with the boundary between rock subjected to the peak shock compression and a theoretical "near-surface zone" predicted by the spallation model. Thus, between this boundary and the free surface, the target material should receive reduced levels of compressive stress as compared to the more highly shocked region below.

1.1 Introduction

In this paper we present results of experiments designed to constrain theories of spallation in high-velocity impacts. Spallation, the separation of large fragments from a free surface as a result of dynamic tensile failure, is of interest because it is a mechanism that may eject lightly shocked material from planetary and asteroidal surfaces.

Much of the recent interest in spallation has resulted from the discovery that the meteorite ALHA81005 is a lunar rock (Marvin, 1984), and the SNC meteorites (shergottites, nakhlites, and Chassigny) may have originated on Mars (McSween and Stolper, 1980; Wood and Ashwal, 1981). For background information on SNC meteorites, McSween (1985) gives an extensive review of the literature pertaining to their composition and unique characteristics. In particular, the absence of shock metamorphism of the nakhlite meteorites has motivated a search for mechanisms capable of accelerating impact ejecta to a Martian escape velocity of 5 km/sec without subjecting it to high, peak-shock pressures. These criteria pose a problem because the Hugoniot equation of state for one-dimensional planar flow determines a direct relation between particle and free surface velocities and the shock pressure. This relation implies that achieving particle velocities near 5 km/sec by direct shock requires shock pressures of 20 to 30 GPa. Several models have been proposed to accelerate impact ejecta to the Martian escape velocity. One of these is the Melosh (1984) impact spallation model. We will address the predictions of this model for ejection velocity, fragment size, and peak shock-pressure distributions at length below.

In the past, spallation has been studied at near-surface and surface explosion craters in alluvium (Stump and Reinke, 1984). Evidence of impact spallation could be inferred from numerical models (Ahrens and O'Keefe, 1978), showing the production of lightly shocked ejecta originating near the free surface. Moreover, Vickery (1986)

finds evidence for relatively high-velocity spalls from analyses of lunar and Martian secondary craters, but concludes that fragments on the order of tens of meters could not escape from either the Moon or Mars by this mechanism. However, there are no published values of spall velocities measured from experimental impacts.

Aside from determining the origin of the SNC meteorites, another context in which spallation is of interest is in the evolution of asteroids (and by implication, planetesimals in the early solar system). Here we are concerned not with the production of a small quantity of exceptional ejecta, but with impacts under such low gravity that strength effects are important on a large scale. As crater size decreases, the fraction of material ejected by spallation increases. On the largest asteroids (surface gravity 0.1 m/s^2), not only is gravity less important for craters with depths as great as 50 m (Gaffney, 1978), but the likely low strength of the regolith on these bodies may lead to the escape of a substantial fraction of the ejecta by spallation (Cintala *et al.*, 1979). This process may be important in the evolution of asteroid families and belts (Capaccioni *et al.*, 1986).

This paper will begin with a description of the spallation experiments. A qualitative description of the targets will be presented along with the results of the spall velocity measurements. A preliminary discussion of the measured spall velocities was given by Polanskey and Ahrens (1985). Next, the Melosh (1984) spallation model will be reviewed with respect to its application to the present experiments. This section will include a discussion of the relationship between the proposed lightly shocked region of the target and the internal fractures observed beneath several of the experimental impact craters in this study. Vertical spall velocities predicted by the hydrodynamic ejection version of the spallation model will then be compared to the measured, experimental spall velocities.

1.2 Experimental Procedures

The spall-velocity experiments were conducted in two phases. In February 1984, preliminary spall velocity measurements were made at the Caltech shock wave laboratory for two low-velocity impacts. The remaining experiments spanned a range of impact velocities and were conducted in September 1984 at the NASA Ames Vertical Gun Range (AVGR).

In all cases, the target material was San Marcos gabbro. This material has a density, ρ_t , of 2.9 g/cm³, dynamic tensile strength, σ_t , of 0.15 GPa, and longitudinal wave velocity, c_L , of 6.4 km/sec (Lange *et al.*, 1984b). To the level of approximation used in this paper, c_L is considered to be independent of stress. The compressive strength is between 3 and 6 MPa. Birch (1966) calculates the Poisson ratio, μ , for San Marcos gabbro as 0.32. A detailed characterization of the mineralogy of this rock can be found in Lange *et al.* (1984b).

For the low-velocity experiments, a 30/06 rifle was used to obtain impact velocities near 1 km/sec. The projectiles were a 4.1 g lead bullet measuring 7.8 mm in diameter and 2.4 cm in length, and a 7.9 mm diameter aluminium sphere with a mass of 0.65 g. The aluminium projectile had been chosen to reduce the density difference between the projectile and the gabbro target. The gabbro was cut into cubes roughly 16 cm on a side and mounted with concrete into sections of 27 cm diameter PVC pipe. The total target mass was just under 30 kg. The targets were mounted in a vacuum tank kept at atmospheric pressure. The tank contained three He-Ne lasers to measure projectile velocity (Figure 1.1a). Two x-ray tubes were positioned approximately 1m outside the tank (1.5 m from the point of impact). The first x-ray tube was timed to photograph the target immediately before impact, and the second x-ray photograph was taken of the ejecta and spall fragments 300 msec later. Spall velocities were determined by measuring the distance traveled by the spall fragments from the target surface during

TABLE 1.1

Experimental Parameters

	603	608	840901	840902	840904	840905	840906	840907	840909
Projectile									
Material	Pb	Al	Al	Fe	Fe	Fe	Fe	basalt	steel
a (cm)	0.391	0.397	0.159	0.159	0.159	0.159	0.159	0.238	0.318
m_p (g)	4.10	0.65	0.0443	0.1292	0.1297	0.1297	0.1297	0.1557	1.0571
ρ_p (g/cm ³)	11.3	2.56	2.64	7.74	7.74	7.74	7.74	2.75	7.90
U (km/sec)	0.89	1.01	6.49	4.60	5.44	4.60	4.76	2.26	1.69
KE (10^{10} ergs)	1.62	0.33	0.93	1.37	1.92	1.37	1.47	0.40	1.51
Target									
M_t (kg)	23	23	24	25	29	23	13	23	24
KE/M_t (10^5 erg/g)	7.0	1.4	3.9	5.5	6.6	6.0	11	1.7	6.3
Crater Dimensions									
Depth (cm)	0.95	0.35	1.0	1.50	1.65	1.45	1.40	0.70	1.40
Diameter (cm)	6.3	2.2	6.5	9.8	10.5	8.0	9.2	3.5	8.3
Volume (cm ³)	9.5	0.5	9.0	30	36	19	23	2.3	25.5
Displaced Mass									
M_e (g)	27.0	1.4	25.8	86	103	54.5	65.9	6.6	73.1
M_{spall} (g)	—	—	10.1	40.6	47.4	36.4	30.8	—	28.8
M_{spall}/M_e	—	—	0.39	0.47	0.46	0.67	0.47	—	0.39

that time interval (Figures 1.1b,1.1c).

Both the low-velocity powder gun and the light gas gun were used at the AVGR, thus providing a range in impact velocities from 1.7 km/sec to 6.5 km/sec. The projectiles for these experiments were primarily 3.2 mm diameter spheres of iron and aluminium with the addition of two slightly larger projectiles of steel and basalt. Projectile masses were between 1.06 and 0.04 g and are listed along with other experimental parameters in Table 1.1. The targets were 23 to 30 kg unmounted blocks of San Marcos gabbro placed in a tank evacuated to 5 mm Hg. The interior of the vacuum tank measured 2.5 m in diameter and 1.8 m in height. The cratering events were recorded by a Dynafax model 350 35-mm framing camera with variable framing rates

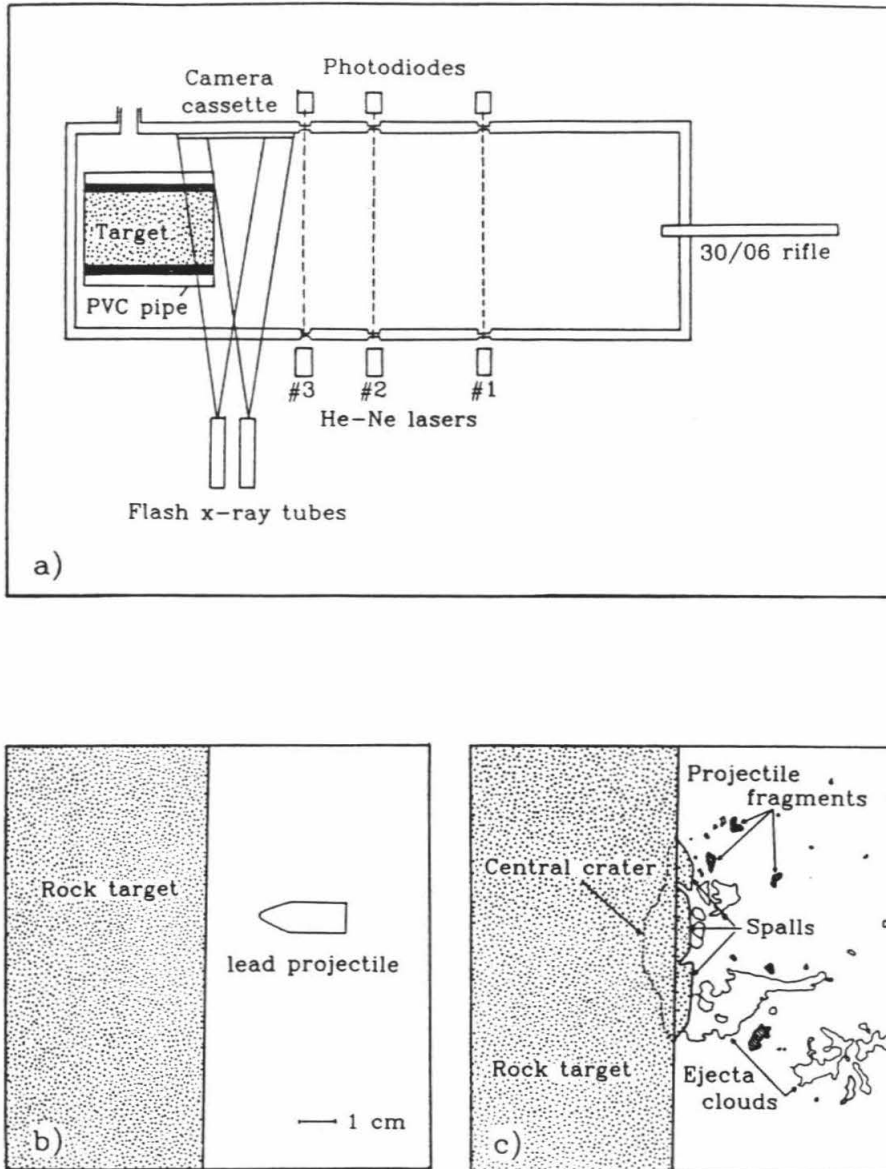


FIGURE 1.1 : a) Sketch of experimental configuration for spall velocity measurements. The projectile velocity is determined by a counter, measuring time intervals as the projectile breaks the laser beams. The lasers also activate other counters which then trigger the x-ray tubes. b) Drawing of the first x-ray exposure showing the projectile in flight at approximately $20 \mu\text{sec}$ before impact. c) Drawing of the second x-ray exposure taken approximately 300 msec later. Spall velocities are measured directly from this exposure. In addition to the spall fragments, high-speed ejecta and projectile fragments are also visible.

from 9000 to 35,000 frames/sec. Illumination was provided by a Cordin model 359 strobe. The photographic equipment was located outside the vacuum tank approximately 1.5 m from the target. Figure 1.2 shows a series of three frames taken at 2 msec intervals from one of these films. The consecutive positions of one prominent spall fragment are marked on each frame.

After each shot, the ejecta fragments were inspected for evidence of spallation. Because spallation is a near-surface phenomenon, a spall fragment was defined to be any ejecta fragment containing part of the original surface of the target. In most cases, the top surface of the target had been polished and was easily identified. Most of the ejecta fitting the above criteria were recovered, and their locations within the tank were recorded. However, no attempt was made to search the tank in a systematic fashion, so it is unlikely that this data set is complete. The mass of each identified spall fragment, m_{spall} , was determined, and both the maximum length, l_{max} , and the thickness from the top surface to its maximum depth, t_{max} , were measured. These parameters are listed in Table 1.2. The total mass of spall fragments collected from each impact, M_{spall} , is listed in Table 1.1. The ratio of t_{max} to l_{max} is plotted in Figure 1.3 as a function of spall mass. The average value of t_{max}/l_{max} for all the collected ejecta was 0.2, and is also very close to the average value for the fragment set from each individual experiment.

Crater volumes were determined by measuring the volume of dry #120 Ottawa sand required to fill each crater. This crater volume was used to calculate the total mass of material ejected from each crater, M_e . This result was then compared to the total mass of spall fragments collected, M_{spall} , and listed in Table 1.1. For these experiments, between 39 and 67% of the excavation was due to spallation. Next, the displaced mass, M_e , was scaled by the ratio of projectile to target density, and plotted as a function of projectile energy in Figure 1.4. These results plot close to the curve Gault (1973) fit to data from 64 earlier impact experiments. Finally, several

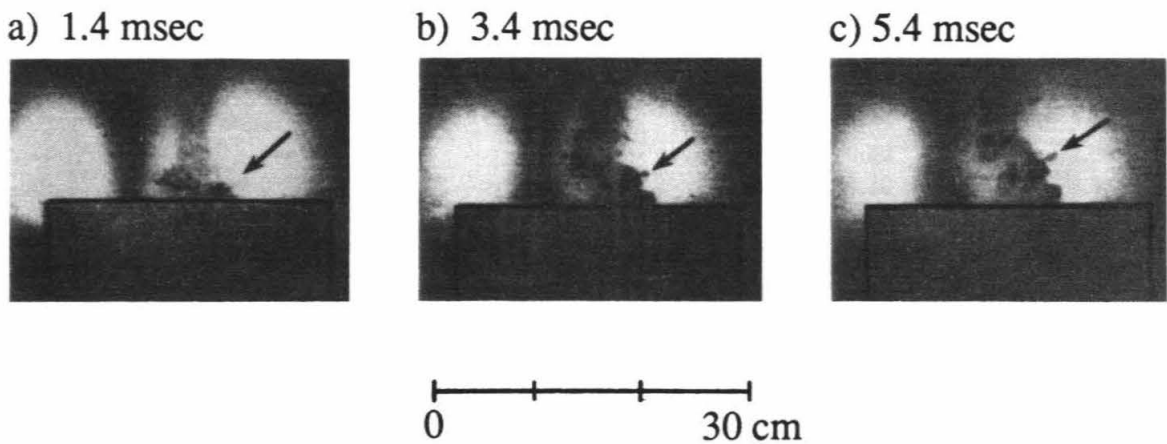


FIGURE 1.2 : Three frames from the film of shot 840904 are shown to illustrate the film coverage of the Ames experiments. The time elapsed since impact is given above each frame, and the time interval between frames is 2 msec. The spall fragment indicated by the arrows is traveling at an average vertical velocity of 8.9 m/sec. The target outline has been enhanced.

TABLE 1.2

Spall Fragment Dimensions

m_{spall} (g)	l_{max} (cm)	t_{max} (mm)	m_{spall} (g)	l_{max} (cm)	t_{max} (mm)	m_{spall} (g)	l_{max} (cm)	t_{max} (mm)
840901			840902			840904		
4.40	5.25	4.47	10.50	5.50	8.89	15.30	5.06	9.19
0.80	1.80	4.32	8.00	4.30	8.13	9.20	4.55	7.21
0.70	1.65	3.43	7.80	4.60	8.38	5.00	4.10	6.78
0.65	1.95	3.66	6.30	3.80	6.22	4.10	3.00	7.62
0.40	1.40	3.20	2.00	2.75	5.36	2.60	2.90	6.40
0.40	1.95	2.24	1.60	2.10	5.31	2.00	2.65	6.12
0.20	1.15	2.64	1.00	2.15	6.40	1.40	2.30	5.28
0.10	0.90	1.88	0.60	1.65	4.44	0.90	2.20	4.06
0.05	0.50	0.66	0.20	1.20	1.98	0.70	2.40	2.54
0.50	0.85	1.27	0.05	0.60	0.68	0.60	2.45	4.27
						0.40	1.40	3.25
						0.30	1.25	3.00
						0.30	1.55	2.34
						0.25	1.15	3.00
840905			840906			840909		
3.00	2.70	6.65	17.60	6.70	9.40	9.50	4.00	8.71
3.00	2.60	5.16	4.70	3.65	7.47	5.50	3.45	6.88
2.40	3.40	7.92	2.55	3.20	5.64	3.00	2.60	5.79
1.90	2.05	5.74	2.30	2.65	5.69	2.30	2.95	5.82
1.70	2.15	3.99	1.40	2.55	5.41	1.30	2.25	4.32
1.15	2.65	2.89	1.00	1.60	4.70	1.10	1.40	5.54
0.80	1.90	5.28	0.30	1.20	3.91	1.05		3.99
0.70	1.50	4.88	0.05	2.20	0.89	0.90	1.60	4.93
0.55	1.90	2.97				0.90	1.55	4.37
0.50	1.65	3.94				0.40	1.40	3.50
0.50	1.70	2.84				0.30	1.40	3.76
0.45	1.65	2.49				0.25	1.60	5.64
0.35	1.55	2.97				0.25	1.60	2.44
0.15	1.20	4.01				0.15	1.55	1.62
0.15	0.90	3.71				0.10	2.25	1.57
0.10		1.98				0.10	1.15	1.24

targets were bisected through the center of the crater in order to observe the internal fractures. The results of the fracture analysis will be presented in the next section.

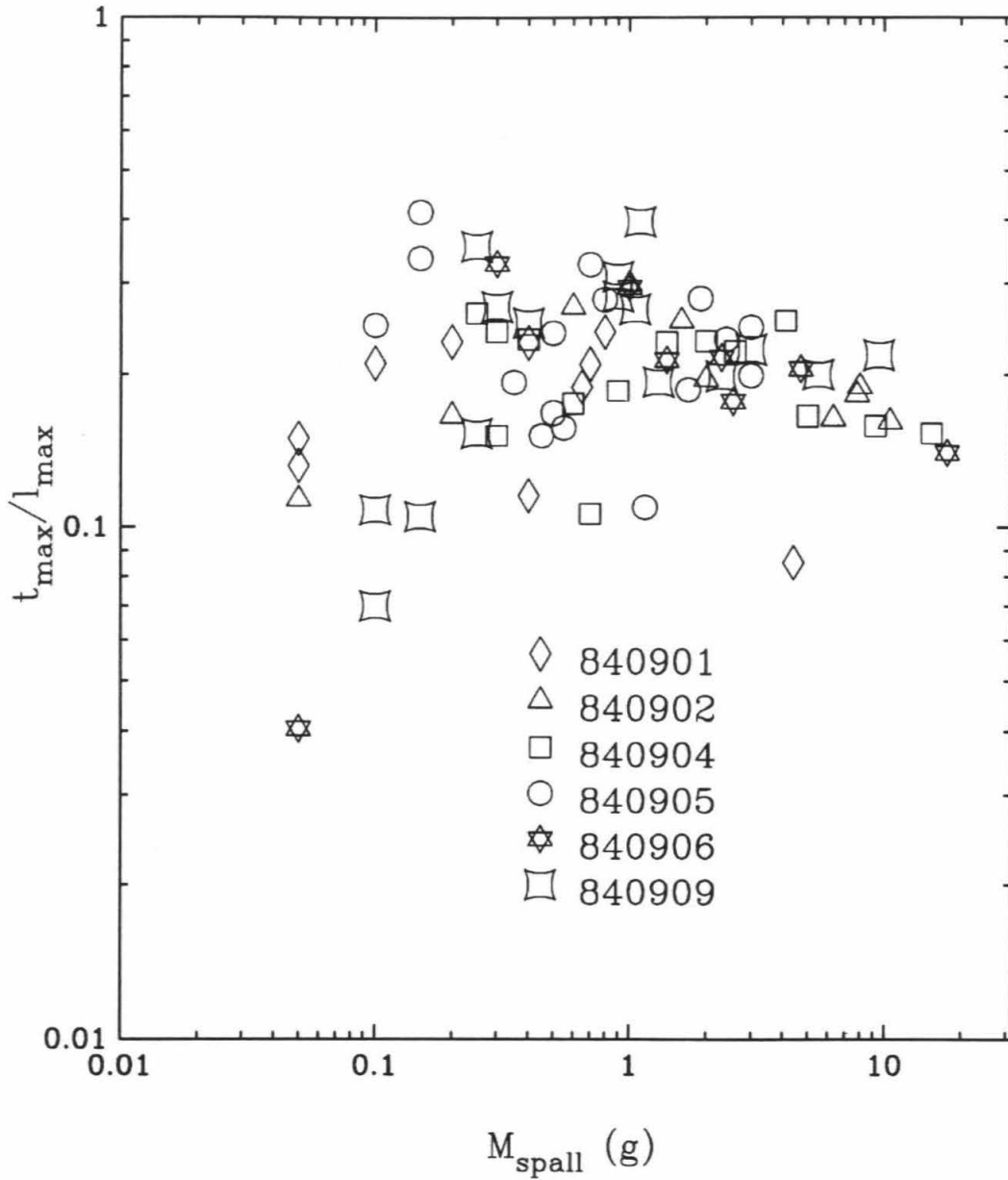


FIGURE 1.3 : The ratio of maximum vertical spall thickness, t_{max} , to maximum spall length, l_{max} , is plotted as a function of mass for each of the collected spall fragments.

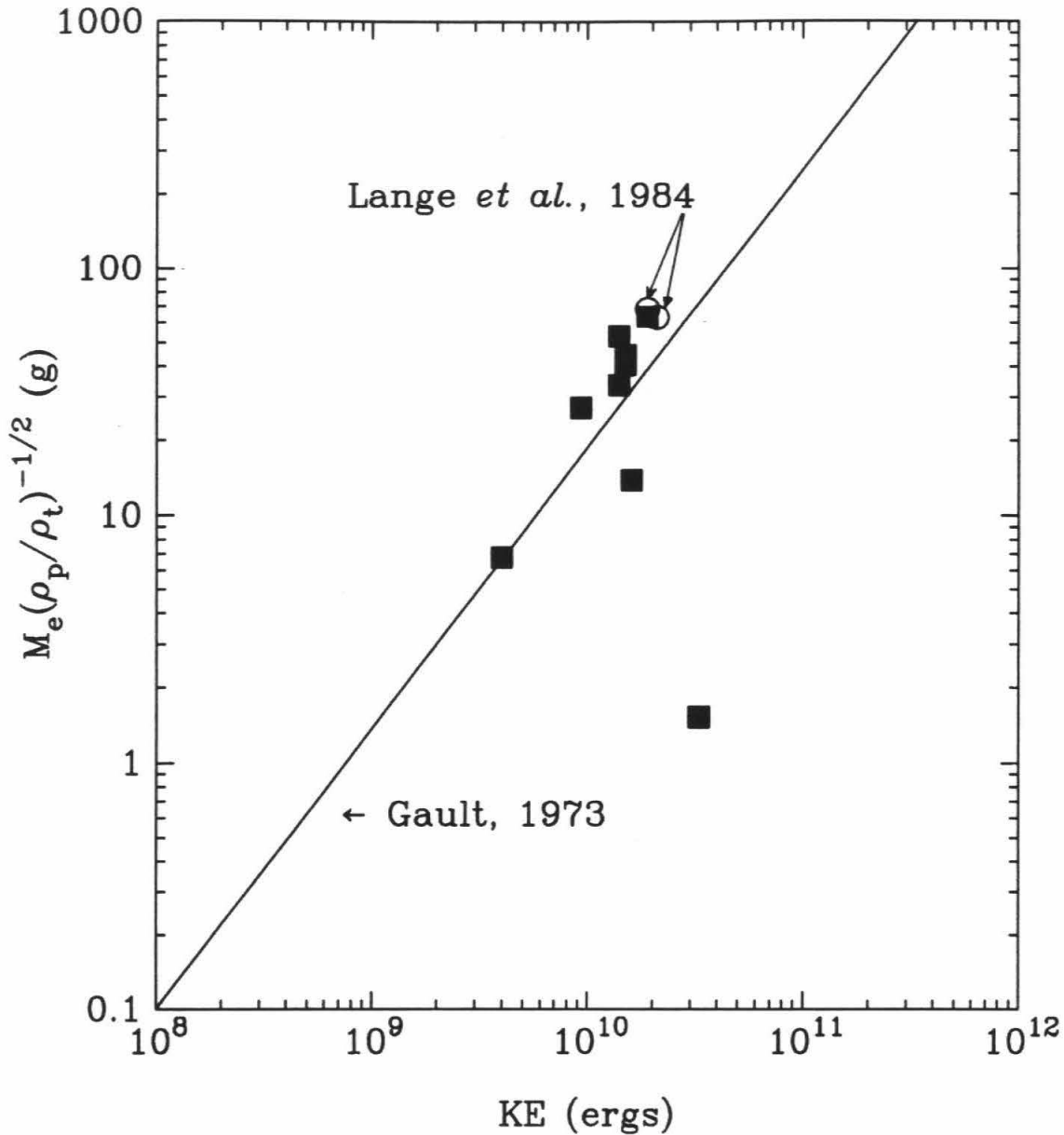


FIGURE 1.4 : Relationship between a corrected form of the displaced mass and the kinetic energy of the impact. The current results, solid squares, are plotted along with data from Lange *et al.* (1984), open circles, and a linear fit to the Gault (1973) data.

1.3 Results

In all cases, the craters displayed two distinct zones. The floor at the central pit of the crater was highly fractured and covered with finely crushed rock, whereas the wide, shallow, outer zone had a relatively fresh surface. It is proposed that this outer zone is the result of spallation, while the inner zone was excavated by downward and then outward and upward flow. In several cases the plan view of the outer crater perimeter was very irregular. There is also evidence of incomplete spalls in the outer zone, which were either partially separated from the target or visible only as surface cracks. Based on the ratio of projectile energy to target mass (given in Table 1.1), these experiments fall into the classification of crater formation, where $KE/M_t \leq 1 \times 10^6$, and the target suffers no additional damage aside from the actual crater (Gault and Wedekind, 1969; Fujiwara *et al.*, 1977). It is also important to note that these craters fall into the energy range of the strength regime where $\sigma_t/\rho g D \gg 1$ (Gault and Wedekind, 1969). Values for the present impacts are on the order of 10^5 and are listed in Table 1.1. The features described above are consistent with descriptions of other impact craters produced in competent rock targets by Lange *et al.* (1984b); Gault (1973); Horz (1969); and Moore *et al.* (1963).

1.3.1 Fractures in targets

Bisecting the targets gave a detailed view of the internal fragmentation resulting from each impact. An example map of the distribution of these fractures in one of the gabbro targets is given in Figure 1.5. The fractures visible without aid of magnification fall into seven classifications, which can be grouped into three different regions of the target. Most of the fractures occur in Region 1, a hemispherical area immediately below the crater extending outwards for at least 10 projectile diameters. This region is characterized by a high density of small fractures, with the rock immediately be-

low the crater floor being the most heavily crushed. These fractures are classified as "shear fractures" after the description in Moore *et al.* (1963). Also within this region are closely spaced "radial fractures" and larger "concentric fractures." Vertical cracks were found beneath the pit of several of the experimental craters. This phenomenon has been described by Fujiwara (1980) as a "central spallation fracture" resulting from the crossing of the two rarefaction waves formed by reflection at the vertical, free surfaces.

Outside Region 1 there are relatively few other visible fractures, and these fall into one of three very distinct categories. A series of vertical fractures are located close to and parallel to the vertical sides of the target blocks. These cracks are labeled as "side spallation fractures" after Fujiwara (1980), and are presumably due to reflections of the shock waves from the sides of the target. These fractures form the boundary for Region 2, which is the area where reflections from the target sides interfere with normal processes. This region will be virtually ignored in the remainder of the paper.

The third region is not really a region but a thin band of fractures starting at the crater wall and arcing down into the target. Subhorizontal fractures are found below and parallel to the floor of the proposed "spalled" zone. These fractures resemble the "spall fractures" observed by Maurer and Rinehart (1960) in several targets from very low-velocity, experimental impacts. The remaining fractures constitute a distinct category labeled "near-surface fractures" in Figure 1.5. The origin of this terminology will become clear later in the Discussion section. The near-surface fractures are also radial in nature, although in general, they extend farther from the crater than those classified as "radial" above. In most cases, the fractures are bordered above and below by regions where the target is not visibly fractured. Finally, these fractures are much wider than most of the radial fractures immediately below the crater. In many cases, these fractures are the most prominent feature in the target cross section.

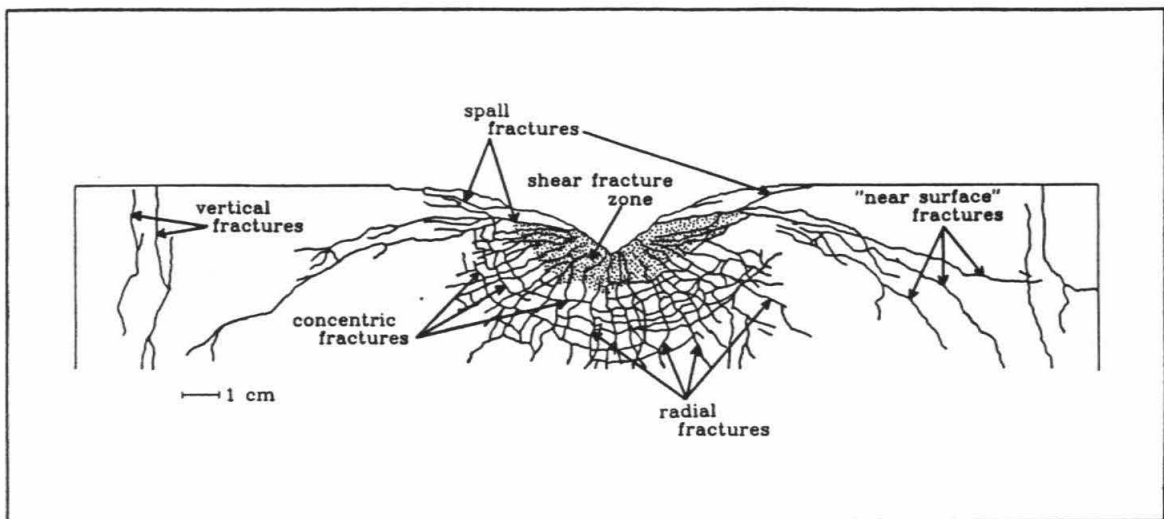


FIGURE 1.5 : Cross section of the target from shot 840904 illustrating the classification of internal fractures. Note that all fractures have been drawn with the same line thickness despite actual variations in the target. The shaded area immediately below the crater indicates a highly fractured region.

1.3.2. Spall velocity measurements

Analysis of the x-ray records from the two low velocity shots gives vertical spall velocity measurements of 11 m/sec and 17 m/sec for the lead and aluminium projectiles, respectively. These velocities are both less than 2% of the impact velocity. In these photographs large spall fragments are clearly distinguished from the smaller ejecta. The spall fragments appear to be ejected at an angle close to 90° from the target surface; however, at the time of the second x-ray exposure, the spalls had not yet completely separated from the target.

Vertical velocities were also measured from the framing camera films of the high-velocity Ames experiments. As evident in Figure 1.2, the distinction between the spall fragments and the other ejecta is less obvious. This loss of resolution was partially the consequence of the scale of the photographs, and of a malfunction in the strobe system that underexposed the films. However, since practically all of the larger fragments collected were spall fragments, it is likely that these velocity measurements correspond to spall fragments. Approximately ten velocity measurements were taken for each particular fragment. In some cases there were large variations in velocity for a single fragment; therefore, the extremes in velocity as well as the average velocity are listed in Table 1.3. The average vertical velocities ranged between 0.9 and 30 m/sec for the complete set of measurements. The results of the velocity measurements are plotted in Figure 1.6. The error bars indicate not only the measurement errors but the range in velocities measured for each fragment. It is important to note that these velocities do not constitute a complete sampling of the spalls ejected from each event. Only the velocities of the largest fragments could be measured from the films. In addition, variations in velocity with time were observed for individual spall fragments. This may be partly a consequence of the spinning and tumbling of the fragments in flight.

Ejection angles could not be measured directly from only the two-dimensional

TABLE 1.3

Spall Velocity Measurements

Shot #	Spall #	v_{min} (m/sec)	v_{ave} (m/sec)	v_{max} (m/sec)
603	1	8.7	11.0	13.5
608	1	17.0	17.3	17.6
840902	1	16.3	20.6	27.4
	2	10.2	14.8	17.2
840904	1	28.7	30.0	31.3
	2	17.5	23.1	26.4
	3	14.9	20.2	21.5
	4	9.0	11.7	17.6
	5	5.1	8.9	14.4
	6	0.7	2.6	3.6
840905	1a	22.4	23.6	24.1
	1b	20.8	22.8	25.3
	1c	19.3	21.5	23.7
	2	12.2	13.0	14.4
	3	9.4	10.8	12.3
	4	3.9	5.8	7.8
	5	0.7	1.2	2.6
6	0.5	0.9	1.3	
840907	1	15.6	17.6	18.8
	2	10.5	14.5	18.9
	3	9.8	13.0	16.5
	4	2.3	4.3	6.7

films; however, ejection angles were determined for two of the spalls from shot 840905 by correlating the fragments on the films with those located after the event. The ejection angles measured for spall #3 and #5 were 90 and 88°, respectively. Both fragments were ejected at low velocities, so they did not interact with the tank walls.

Finally, in some cases the spalls were observed to fragment in flight as predicted by Melosh (1984). This appears to be the case for spalls #1a, 1b, and 1c from shot 840905. In addition to the appearance of fragmentation on the film, these three fragments are also traveling at approximately the same velocity with very little vari-

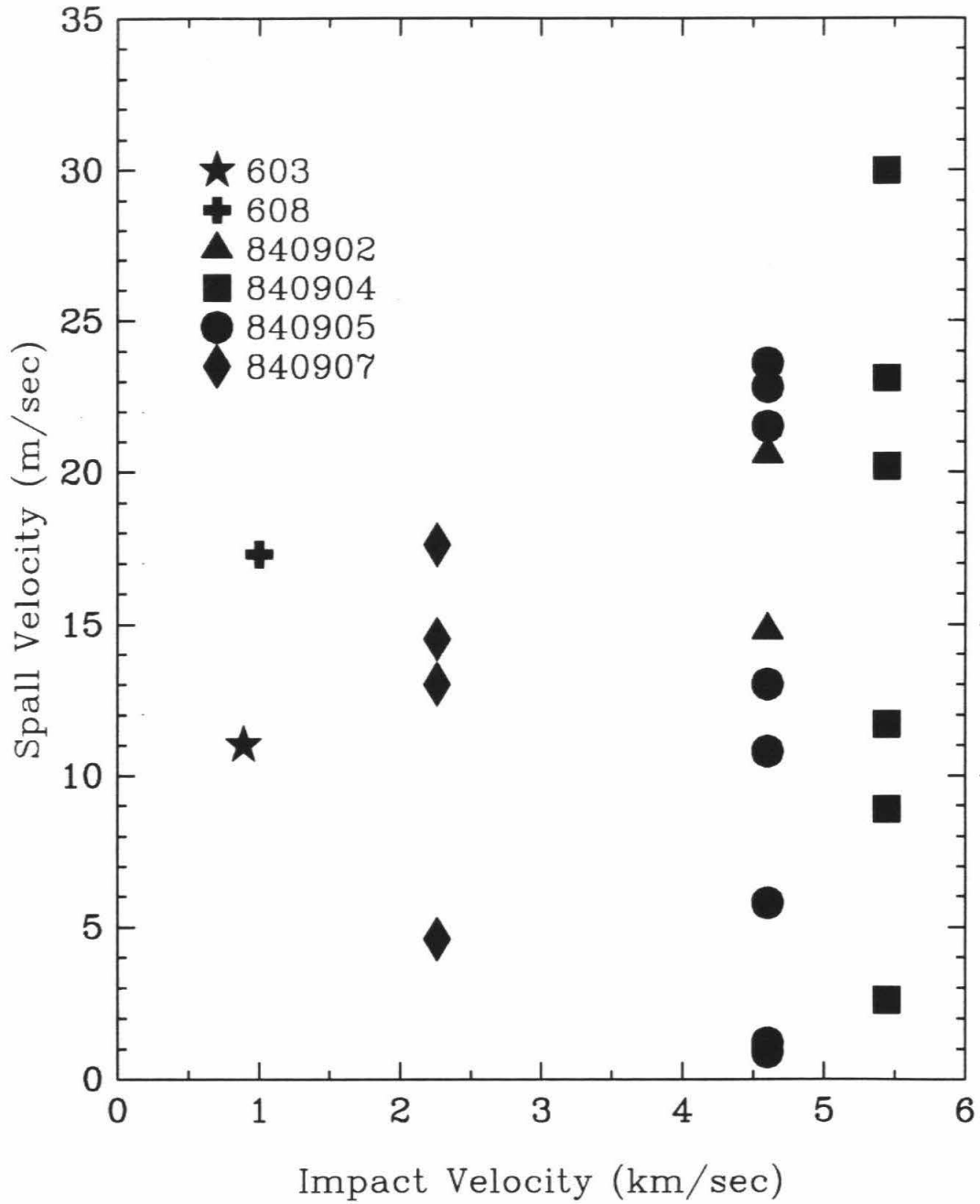


FIGURE 1.6 : Results of the spall velocity measurements for five experimental impacts.

ation in individual velocities. However, it cannot be proven that this was actually fragmentation as opposed to merely an effect that was due to the resolution of the films.

1.4 Discussion

Melosh (1984) derives two versions of a model based on the concept that the stress waves from an impact event are similar to those of an explosive source buried at some depth. First, a hydrodynamic ejection version of the model is presented using the interaction between a compressive wave and the corresponding tensile wave reflected from the target's free surface to predict spall velocities and thicknesses. Next, a stress wave ejection model is developed by adding the effect of a reflected shear wave to calculate ejection angles and fragment sizes. Fragment size is predicted to be inversely proportional to ejection velocity, and ejection angle is found to be a function of the target tensile strength and Poisson ratio. Although Melosh concludes that spallation is an unlikely mechanism for removing significant quantities of material from the Martian surface, it is potentially an important process for ejecting material from asteroids and possibly the Moon. The spallation model is also described and applied in Melosh (1987) and Vickery and Melosh, (1987).

In order to explain the application of the spallation model to the present experiments, we first briefly review the relevant aspects of Melosh (1984) with emphasis on the hydrodynamic ejection version of the spallation model. One important feature of the spallation model is that there exists a region, the near-surface zone, where the target material experiences reduced compressive stress as a consequence of its proximity to a free surface. To satisfy the free surface boundary condition of zero stress, the compressive wave generated by a buried source is exactly canceled at the surface

by the reflection of a tensile wave of equal magnitude. The actual definition of the depth of the source, the equivalent depth of burst, is up to dispute, but here we will use the form used in the spallation model, $d = 2a(\rho_p/\rho_t)^{1/2}$, for a projectile density ρ_p . It then follows that below the surface the two waves will superimpose by virtue of their finite rise and decay times. The near-surface zone is the region where the delay between the two waves is less than the rise time of the compressive wave. This region never experiences the peak of the compressive stress pulse, and is therefore the proposed source of the lightly shocked ejecta.

The depth of the near-surface zone is strongly controlled by the shape of the triangular stress pulse. The pulse shape will be characterized by a rise time, τ , and a decay time, τ_D , where τ is generally less than τ_D . For an impact, τ is modeled as being equal to a/U , where a is the projectile radius, and U is the impact velocity, and $\tau_D = d/c_L$. In this model the rise time is taken to remain constant as the shock propagates, although this may not be strictly true for small-scale impacts (Melosh,1984). The depth of the near-surface zone boundary is defined by the hyperbola in the s - z plane:

$$z_P = \frac{c_L \tau}{2} \left[\frac{4(d^2 + s^2) - c_L^2 \tau^2}{4d^2 - c_L^2 \tau^2} \right]^{\frac{1}{2}}, \quad (1)$$

where s is measured from the point of impact along the target surface. Figure 1.7 illustrates schematically the geometric relationships between s , d , and z_P . The values of τ and d calculated for each experiment are listed in Table 1.4. The last two entries in Table 1.4 are two experiments taken from Lange *et al.*(1986b). The shot numbers 790837 and 790839 correspond to shot no. 1 and 3, respectively, in Table II of Lange *et al.*(1986b). In order to illustrate the range of impact parameters between the eight experiments described above, the values for the depth of burst and the rise time are plotted in Figure 1.8. These two parameters completely determine the shape of the near-surface boundary.

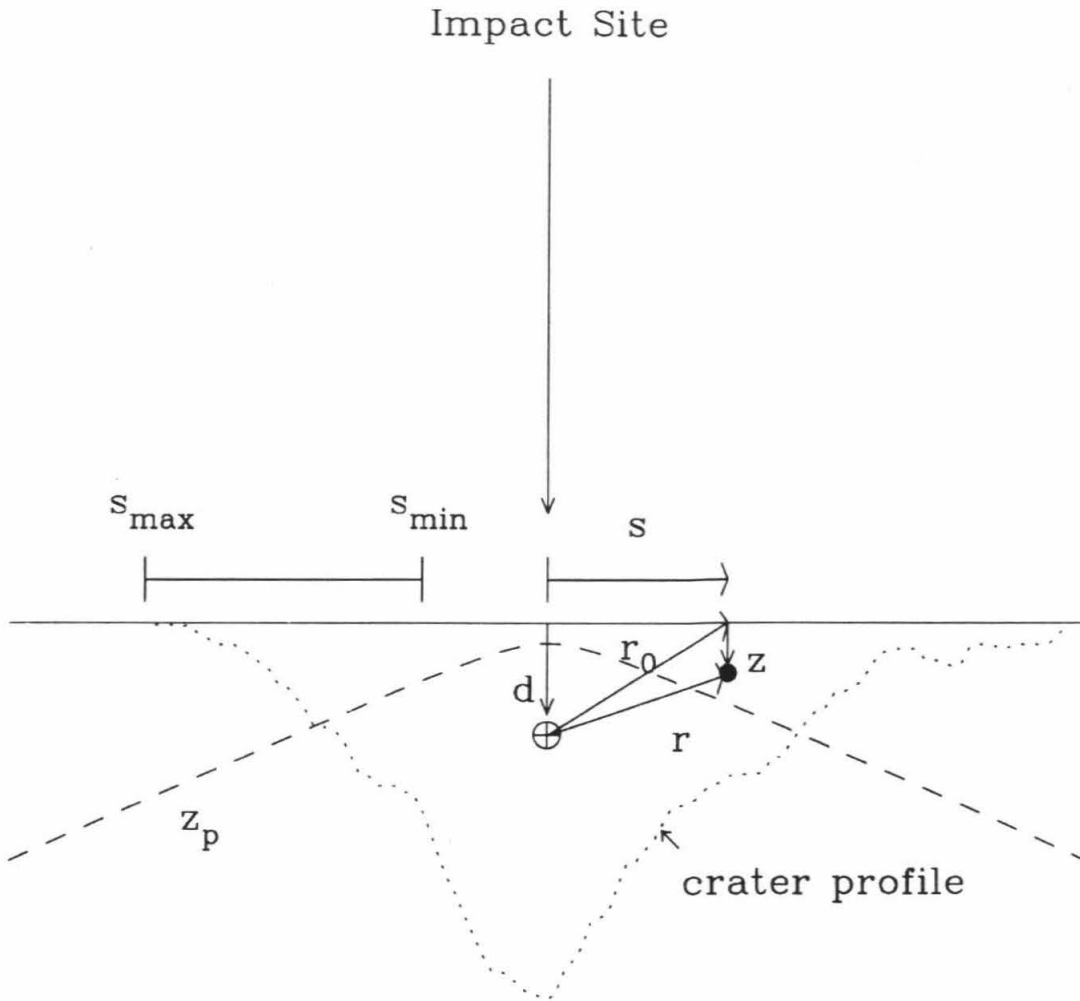


FIGURE 1.7 : Sketch of an experimental crater profile adapted from Melosh (1984). The relationships between the geometrical quantities s , z , r , r_0 , and d are shown in relation to the crater depth profile from shot 840904. Also shown is an example of the range of s values, s_{min} to s_{max} , considered applicable for calculating spall velocities for this impact.

TABLE 1.4

Rise Times and Depth of Burst

Shot #	τ (μsec)	d (cm)
603	4.4	1.55
608	3.9	0.75
840901	0.24	0.30
840902	0.34	0.52
840904	0.29	0.52
840905	0.34	0.52
840906	0.33	0.52
840907	1.0	0.47
840909	1.9	1.06
790837	0.30	0.54
790839	0.34	0.64

Physical evidence for the existence of the near-surface zone was suggested by the distribution of fractures observed in the bisected targets. As mentioned above, the category of "near-surface fractures" consisted of a set of major cracks forming a conspicuous pattern closely following the boundary of the near-surface zone as defined by Equation (1). It is also interesting to note that no cracks were found above this region. A straightforward calculation of z_P for the relevant experimental parameters gives a remarkable fit of the near-surface zone boundary to the actual cracks observed in seven high-velocity experiments 840901, 840902, 840904, 840905, 840906, 790837 and 790839 (Figure 1.9a,b,c). Two of these targets, 790837 and 790839, are shots no. 1 and 3 taken from Lange *et al.*(1984b).

The first exception to this trend is in the target from 840909. Figure 1.9c shows that the near-surface fractures lie significantly above the calculated z_P curve for the relevant impact parameters. Although the total energy of this impact was comparable to that of the previous experiments, the impact velocity for this shot was substantially lower.

The second exception, 603, was also the result of a low-velocity impact. The

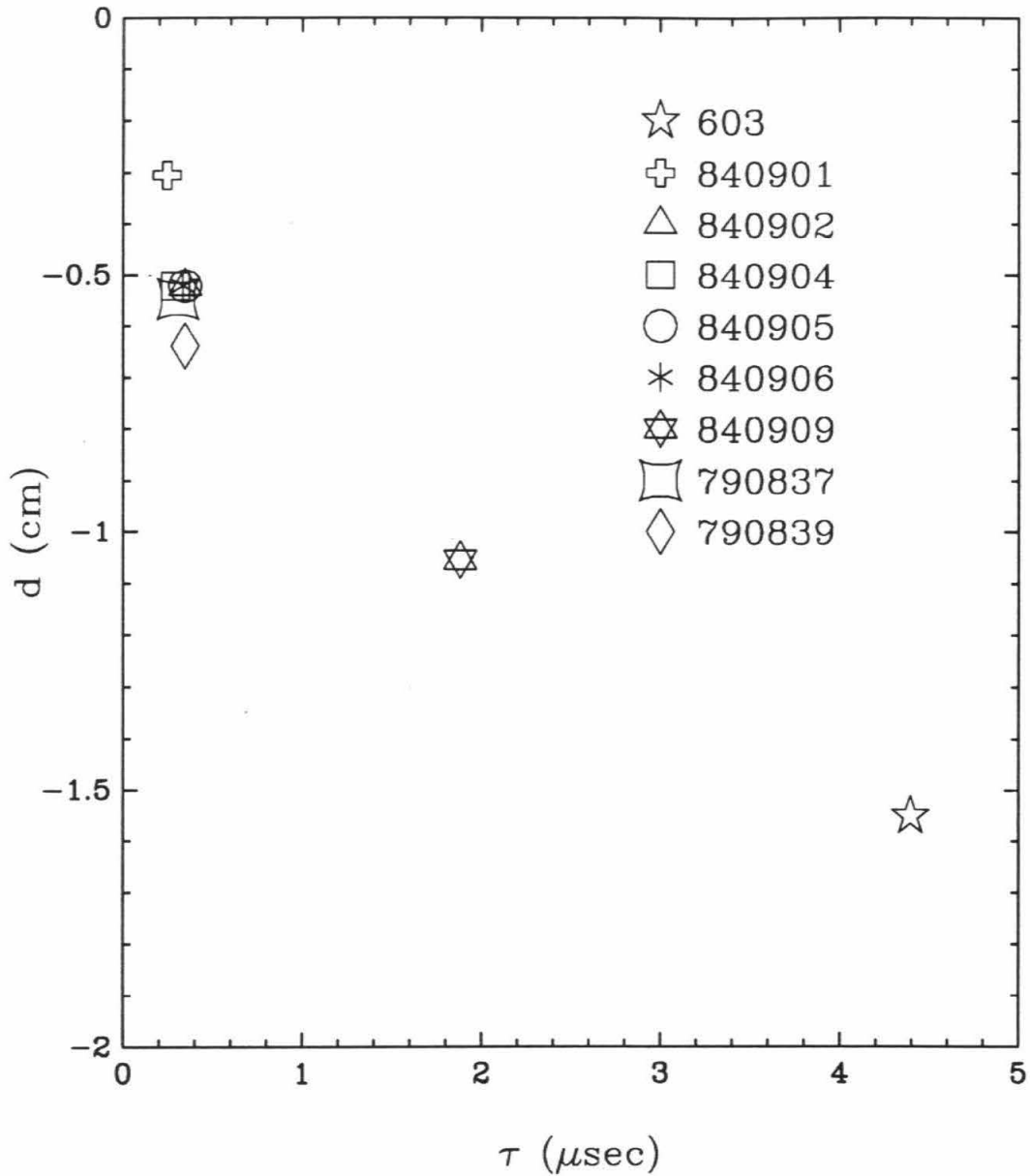


FIGURE 1.8 : Illustration of the range in values of the two major variables (depth of burst, d , and risetime, τ) for the present and some previous experiments.

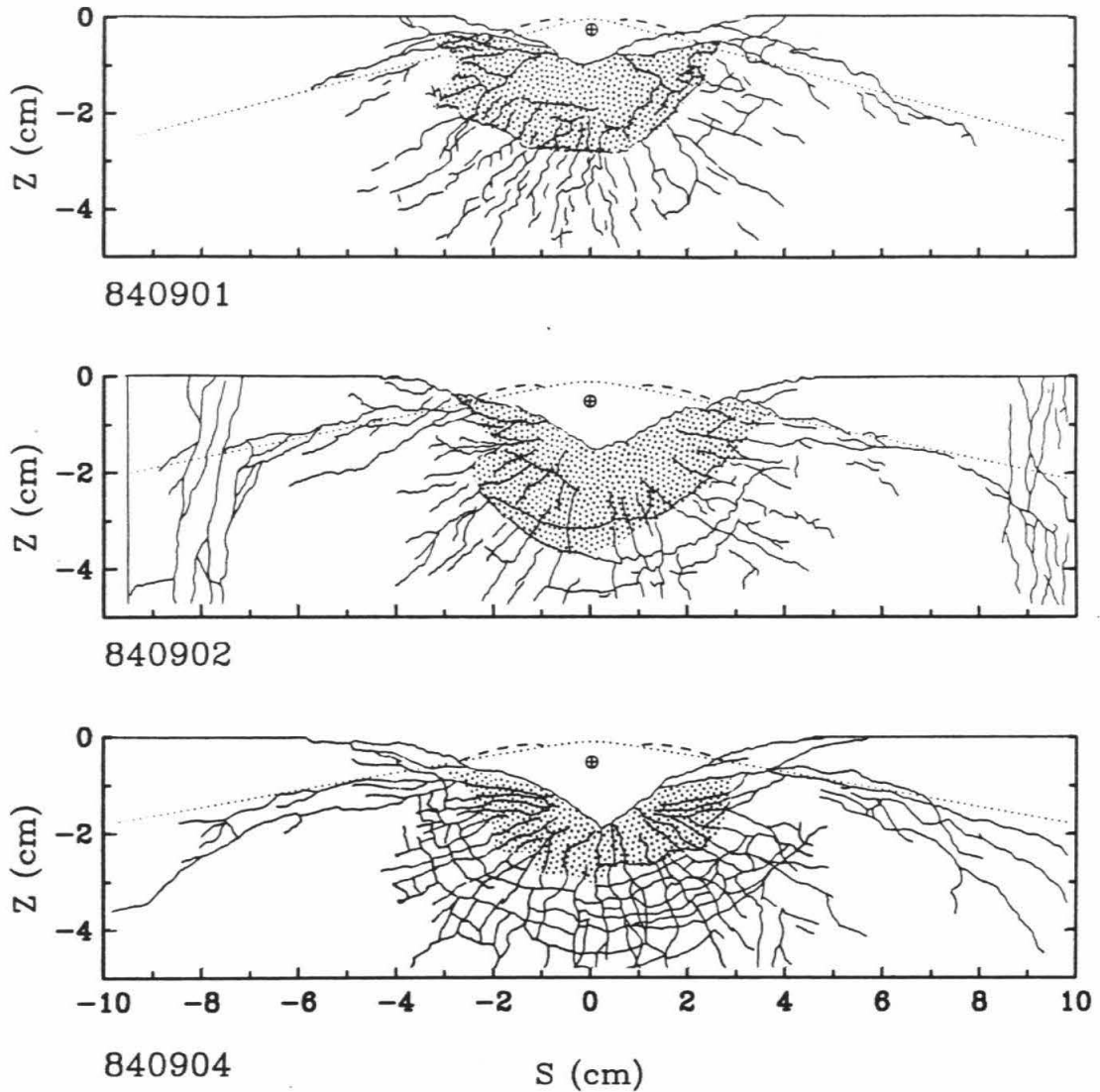


FIGURE 1.9a: Sketches of the fractures found inside targets 840901, 840902, and 840904. The shaded area indicates the highly fractured region immediately surrounding each crater. A plot of z_P , the theoretical near-surface zone (dotted line), is superimposed over the fractures. The calculated spall thickness, z_S , is also plotted (dashed line) within the near-surface zone. The symbol below the surface of each target at $s = 0$ marks the equivalent depth of burst, d , used to calculate the curves.

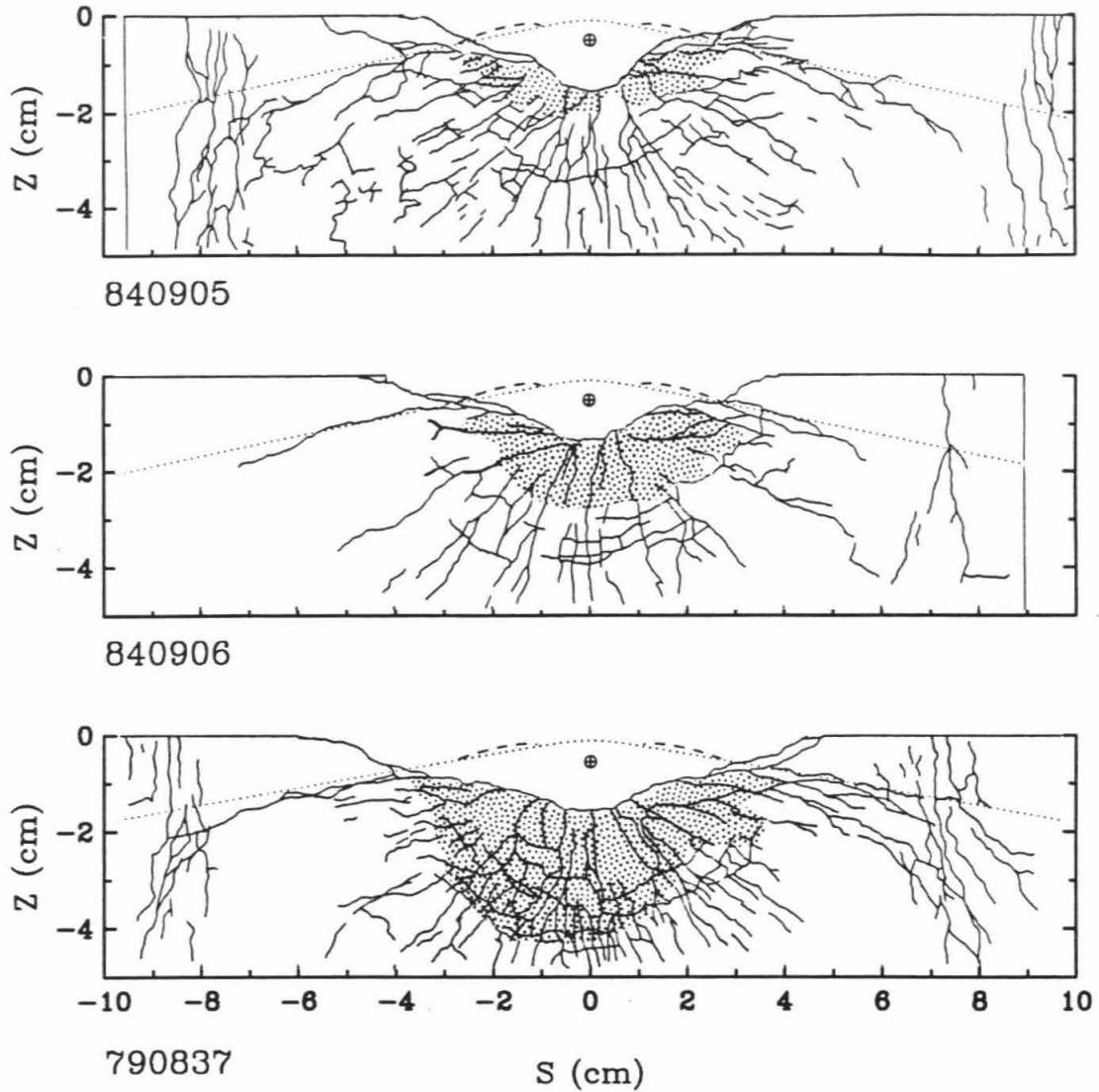


FIGURE 1.9b: Sketches of the fractures found inside targets 840905, 840906, and 790837. The shaded area indicates the highly fractured region immediately surrounding each crater. A plot of z_P , the theoretical near-surface zone (dotted line), is superimposed over the fractures. The calculated spall thickness, z_S , is also plotted (dashed line) within the near-surface zone. The symbol below the surface of each target at $s = 0$ marks the equivalent depth of burst, d , used to calculate the curves.

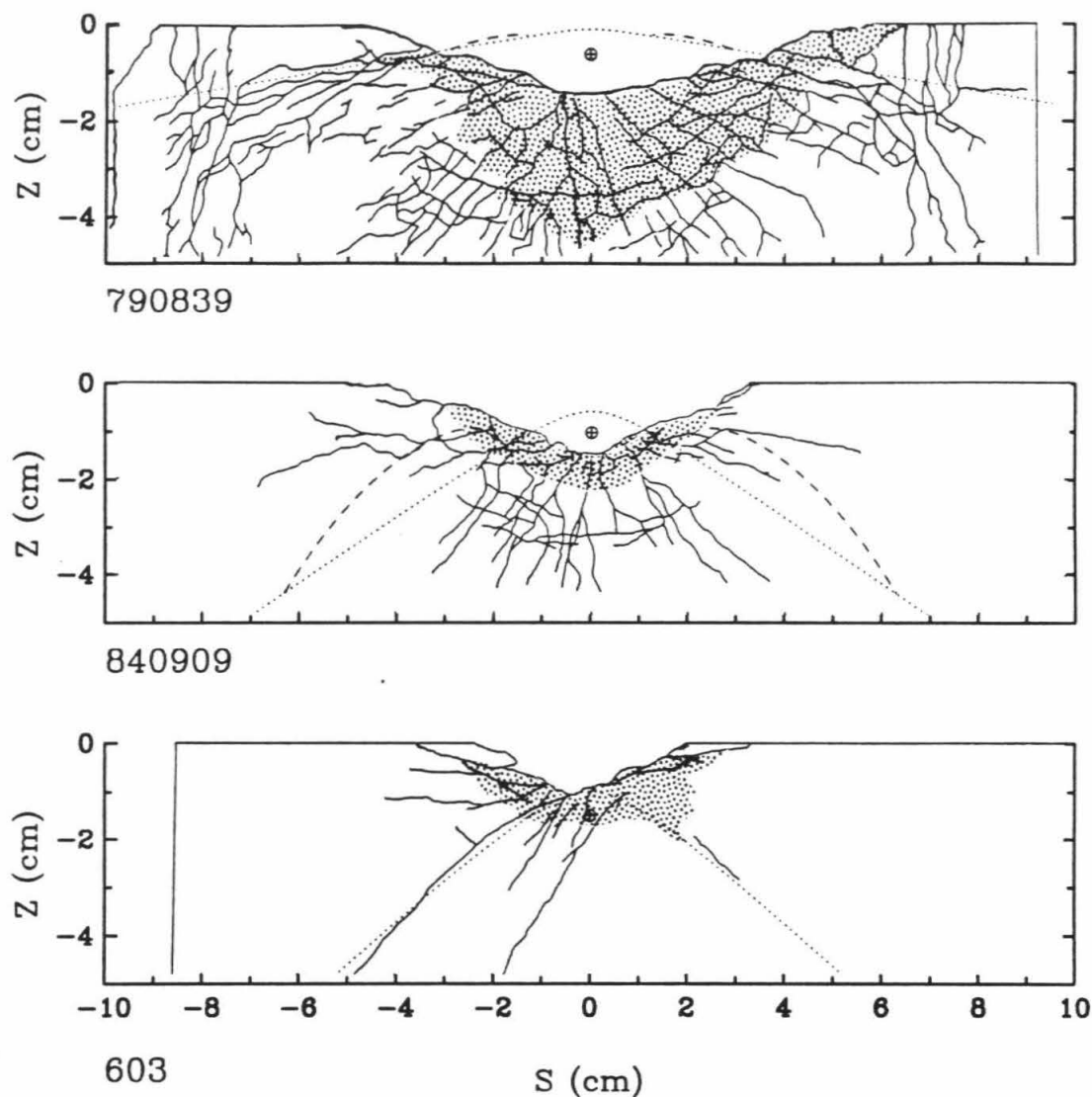


FIGURE 1.9c: Sketches of the fractures found inside targets 790839, 840909, and 603. The shaded area indicates the highly fractured region immediately surrounding each crater. A plot of z_P , the theoretical near-surface zone (dotted line), is superimposed over the fractures. The calculated spall thickness, z_S , is also plotted (dashed line) within the near-surface zone. The symbol below the surface of each target at $s = 0$ marks the equivalent depth of burst, d , used to calculate the curves.

target for shot 603 was qualitatively similar to those described above, although the radially fractured zone was significantly smaller. The most obvious feature in this target was one large crack beginning at the floor of the crater and extending in an arc to a depth of 6cm. Although this crack had the same general form as the z_p boundary, it was asymmetric and did not match the curve defined by the parameters for that experiment. This is not unreasonable, since the projectile was a commercial bullet having a high density and a nonspherical shape. Determining the rise time of the stress wave from the geometry of the bullet is not straightforward. The radius of the bullet is not the same as the length over which the bullet starts as a point and reaches the maximum radius, which is also different from the bullet length. The curve for 603 in Figure 1.9c was fit to this fracture by specifying the values of a and d to be 0.28 cm and 1.5 cm, respectively. This value for a , however, gives a rise time 28 percent less than that based on the bullet radius. Also, this depth of burst falls below the crater floor and is slightly greater than it would be if it were calculated with a 0.28 cm projectile radius. However, manipulating the equations to fit the fracture from this shot is not as important as recognizing its qualitative resemblance to the fractures in the two other targets.

The same wave interaction should occur at the sides of the target as it does at the top surface, and a near-surface zone could be calculated as well. The vertical fractures near the target edges would be a candidate for this effect. However, the resulting boundary curve is much flatter and closer to the target surface. An example of this curve is plotted for shot 840906 in Figure 1.9b; however, the boundary does not correlate with the vertical fractures observed.

Returning to the hydrodynamic ejection model, we consider its predictions for spall thicknesses as a function of s , and vertical spall velocity as a function of s and z . The spall thickness, defined as the depth at which the tensile stress reaches the

dynamic tensile strength of the target material, is given as a function of s by

$$z_S = \left(\frac{\sigma_t}{P(r_0)} \right) \left(\frac{\tau_d c_L}{2d} \right) \left[\frac{r_0}{1 - 1.87 \tau_D c_L / r_0} \right], \quad (2)$$

where $r_0 = \sqrt{s^2 + d^2}$, and is shown schematically in Figure 1.7. The pressure at r_0 is determined by $P(r_0) = \rho_t c_L v_p(r_0)$, where $v_p(r) = (U/2)(\rho_p/\rho_t)(a/r)^{1.87}$ is the particle velocity at that point. This equation for z_S is valid only for z above the z_P boundary. The empirical quantity -1.87 comes from the exponent of pressure decay of the stress pulse. Recent calculations by Ahrens and O'Keefe (1987) find this decay exponent to vary with impact velocity. Their results predict a pressure decay exponent of -1.87 for the impact of a silicate projectile on a silicate target at 9.8 km/sec. The relationship between z_P and z_S is also shown in the seven high velocity experiments in Figure 1.9. It is interesting to note that in agreement with the spallation model, z_S intersects the z_P curve at the edge of the observed crater.

Finally, the spall velocity is given for any $r = \sqrt{s^2 + (d - z)^2}$ within the near surface region as

$$v_{V|SPALL} = 2v_P(r) \frac{d}{r_0} \left[1 - \frac{2dz_S}{r_0 c_L \tau} \right]. \quad (3)$$

The second term in the parentheses is negligible when the spall thickness is much smaller than all other dimensions. Then the spall velocity approaches the maximum value, $v_{V|SPALLmax} = 2v_P(r)d/r_0$. The spall thickness term can be neglected for large planetary scale impacts; however, it becomes significantly large in the calculations simulating the laboratory scale impacts. This term varies from 0.38 to beyond the limiting value of 1.0 in the present experiments. Therefore, the predicted velocities for the laboratory impacts can be at most 62% of the maximum spall velocity. It must also be noted that Equations (2) and (3) are not valid for s less than approximately four projectile radii from the point of impact. For small s , z_S becomes negative as a result of certain approximations made earlier in the model. This artifact of the approximations will have important implications later in this paper.

Although $v_{V|SPALL}$ is a function of both s and z , the calculated spall velocities in Figure 1.10 are the results of the spallation model applied to the laboratory parameters for the limiting case of $z = 0$. This limiting case represents the maximum velocity possible at any given s . The appropriate experimental values of U , a and ρ_p were used with Equation (3) to generate each curve in Figure 1.10. The steep decrease in velocity towards the center of the crater is a result of z_s becoming negative at small s . This portion of the curve can be neglected. Shaded rectangles are included on each plot to compare the spallation model results with the experimental results. The vertical sides of each rectangle represent the range of spall velocities measured experimentally. The horizontal sides of the rectangles limit the range of s to the spalled region measured from each of the craters (Figure 1.7). In all the high-velocity experiments, the model velocity curves intersect the measured velocity fields and reach from 64 to 76% of the peak in the velocity profile predicted by the spallation model. The spall velocities measured for the low-velocity experiments account for a lower percentage of the predicted velocities; however, it is important to note that these two experiments have only one velocity measurement per impact. Although the spall velocities measured in these experiments are only a fraction of the velocities predicted by the model (Figure 1.10); it is important to realize that the model curves represent the maximum surface velocity at any distance from the impact. Furthermore, the spallation model predicts a strong decrease of spall velocity with depth. Since each spall fragment has a finite thickness, its average velocity would be lower than that predicted for a point on the surface. Therefore, the present results compare well with the spallation model, despite the fact that these equations were formulated for conditions much different from those found in small-scale laboratory impacts.

The effect of this scale difference becomes more severe for low-velocity impacts. Equations (2) and (3) are difficult to apply to shots 603 and 608, because the projectile

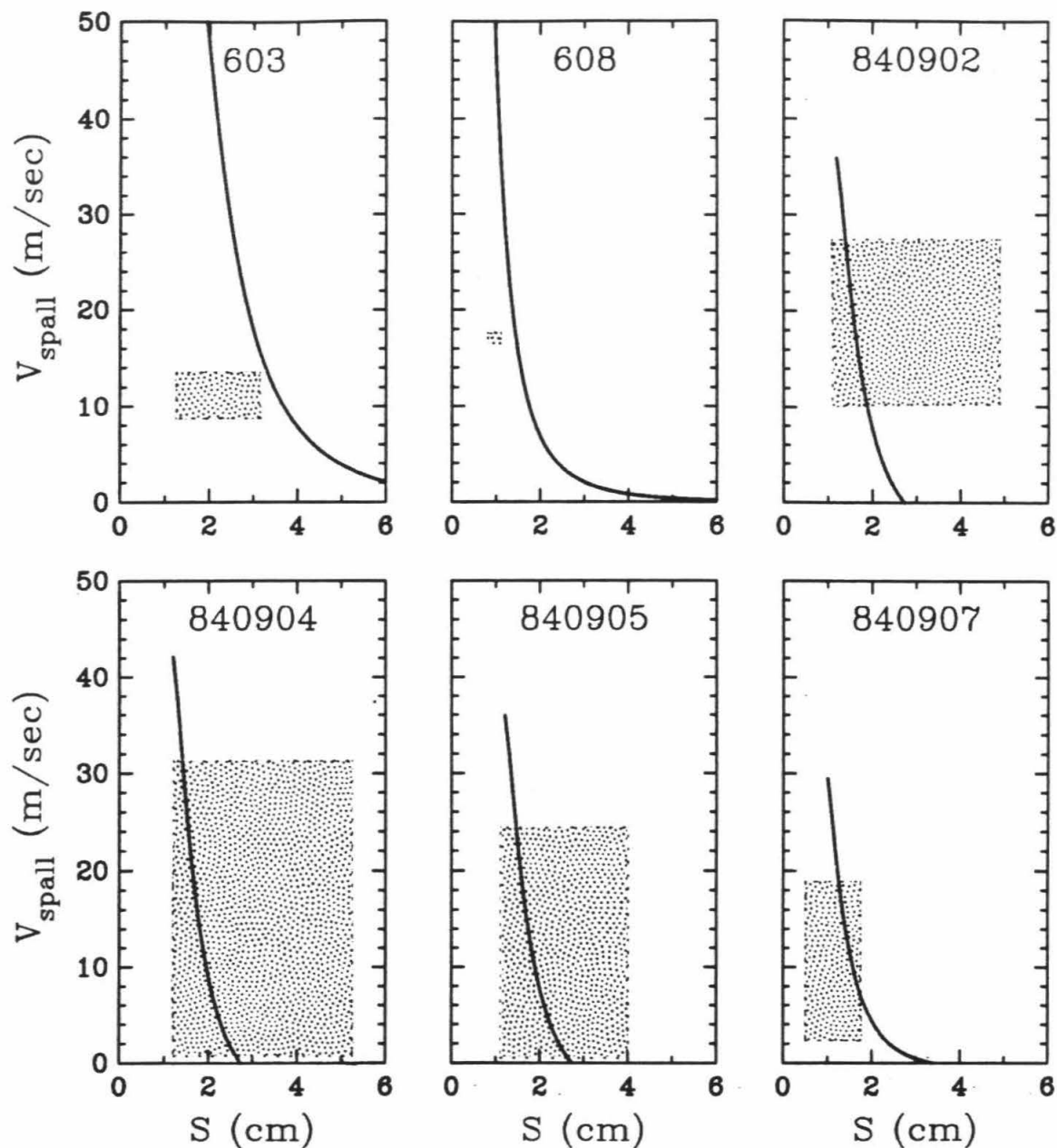


FIGURE 1.10 : Vertical spall velocity, as calculated from the Melosh equations evaluated at $z = 0$, is plotted as a function of s to model five of the experimental impacts. The rectangles provide a comparison of the experimental results to the dotted model curves. The range of measured spall velocities for each event is indicated by the height of the rectangles. The horizontal extent of the rectangles represents the range of s , s_{min} to s_{max} , measured from the spalled zone of each crater (as illustrated in Figure 1.3).

radius is quite large compared to the resulting crater. Thus, the depth of burst calculated according to the above formula is also greater than the actual crater depth. Nevertheless, for these shots, rough estimates of spall velocity were calculated for Figure 10 by adjusting d to equal the depth of the crater. In the case of shot 603, this d turns out to be above the depth of burst determined earlier when fitting the z_P curve to the large fracture.

Although the assumption that spall thicknesses are much smaller than the projectile radius has been violated in most cases, the Ames experiments are more similar to the conditions described by the spallation model. The higher impact velocities in these experiments lead to the strong stress waves needed to satisfy the hydrodynamic approximations. In addition, the Ames projectile radii were smaller than those of the preliminary experiments. This feature, combined with the higher impact velocities, produced shorter rise times for these impacts, which is desirable because the approximations also require that r be greater than $c_L\tau$. Therefore, Equations (2) and (3) could be applied throughout a greater fraction of the crater volume in the high-velocity experiments.

1.5 Summary and Conclusions

Analysis of the interior of six out of eight targets revealed the absence of visible fractures above the predicted boundary of the near surface zone. Furthermore, in the six high-velocity experiments the theoretical z_P boundary could be linked to definite fractures observed in the targets. This correlation gives physical support to the spallation model, and indicates that the material above this boundary may be less highly shocked than target material at a similar radial distance below the boundary. However, a physical mechanism for the formation of these fractures is not obvious.

The measured spall velocities are consistent with the vertical spall velocities predicted by the hydrodynamic spallation model. This statement is valid despite the assumptions inherent in this model, which restrict its application to laboratory impacts. The spall velocities measured were all less than a few percent of the respective impact velocities. The greatest average spall velocity measured, 30 m/sec, was for shot 840904 and was only 0.6% of the 5.4 km/sec impact velocity.

Scaling this measured spall velocity to that expected for a large impact is difficult if we are restricted only to the equations presented in the above discussion. One simple alternative is to examine the basic functional dependencies of Equation (3). We see that spall velocities are primarily a function of impact velocity and the distance from the impact point normalized to the projectile radius, suggesting that spall velocities resulting from the impact of an asteroid traveling at 5 km/sec on a silicate planet would directly scale with s/a to those velocities measured experimentally. If we now consider impacts upon small bodies in the solar system we must first neglect the effects of a regolith. In such a case, the 27 m/sec spall velocity we measure would enable fragments to escape only parent satellites or asteroids less than 46 km in diameter. While this criteria would include the Martian satellites Phobos and Deimos, it would exclude the larger, presumably igneous and differentiated, asteroids such as Ceres and Vesta.

However we note that a more detailed stress-wave ejection version of the spallation model for impacts of larger bodies may permit the possibility of high-speed spallation fragments. Although these were not observed in the present experiments or calculations, a more detailed model would not suffer from the restriction that the fragments must originate from regions farther than four projectile radii from the point of impact. Melosh (1987) has constructed such a model and provides a plot of spall velocities as a function of depth for s between one and five projectile radii. His more recent results predict spall velocities in excess of 13% of the impact velocity for s/a

less than 1.4. For the present experimental impacts, the projectile radii are as small as 0.159 cm. Therefore, if these high-velocity spalls exist, they could not be observed on the films. Even for large impacts, the high-velocity fragments would be a small fraction of the spall fragments ejected. Using this argument, Melosh predicts spalls capable of escaping the Moon but not Mars. However, the present results support the spallation model velocity only at its lower limits where the spall fragments are large enough to be observed.

Acknowledgements

We both have benefited from many helpful technical discussions with Dr. Jay Melosh. We thank Dr. Peter Schultz for his assistance in utilizing the Ames facility. This research was supported by NASA Grant NGL-05-002-105. Contribution no. 4405, Division of Geological and Planetary Sciences, California Institute of Technology, Pasadena, California.

1.6 References

- Ahrens, T. J. and J. D. O'Keefe (1987). Impact on the Earth, ocean, and atmosphere. Proc. 1986 Hypervelocity Impact Symp., *Int. J. Impact Engineering* 5, 13-32.
- Ahrens, T. J. and J. D. O'Keefe (1978). Energy and mass distributions of impact ejecta blankets on the Moon and Mercury. *Proc. Lunar Planet. Sci. Conf. 9th*, 3787-3802.
- Birch, F. (1966). Compressibility; Elastic constants. In *Handbook of Physical Constants* (S. Clark, Jr., Ed.), *Geol. Soc. Amer. Mem.* 97, 97-173.
- Capaccioni, F.; P. Cerroni; M. Coradini; M. Di Martino; P. Farinella; E. Flamini; G. Martelli; P. Paolicchi; P. N. Smith; A. Woodward; and V. Zappala (1986). Asteroidal catastrophic collisions simulated by hypervelocity impact experiments. *Icarus* 66, 487-514.
- Cintala, M. J.; J. W. Head; and L. Wilson (1979). The nature and effects of impact cratering on small bodies. In *Asteroids* (T. Gehrels, Ed.), pp. 579-600. Univ. of Arizona Press, Tuscon.
- Fujiwara, A. (1980). On the mechanism of catastrophic destruction of minor planets by high-velocity impact. *Icarus* 41, 356-364.
- Fujiwara, A.; G. Kamimoto; and A. Tsukamoto (1977). Destruction of basaltic bodies by high-velocity impact. *Icarus* 31, 277-288.
- Gaffney, E. S. (1978). Effects of gravity on explosion craters. *Proc. Lunar Planet. Sci. Conf. 9th*, 3831-3842.
- Gault, D. E. (1973). Displaced mass, depth, diameter; and effects of oblique trajec-

- ories for impact craters formed in dense crystalline rocks. *Moon* 6, 32-44.
- Gault, D. E. and J. A. Wedekind (1969). The destruction of tektites by micrometeoroid impact. *J. Geophys. Res.* 74, 6780-6794.
- Horz, F. (1969). Structural and mineralogical evaluation of an experimentally produced crater in granite. *Contrib. Min. Petrol.* 21, 265-277.
- Lange, M. A.; T. J. Ahrens; and M. B. Boslough (1984a). Cratering and spall fracture in gabbro. Chapter XI:7, In *Shock Waves in Condensed Matter 1983* (J. R. Asay, R. A. Graham, and G. K. Straub, Eds.), pp. 525-528. Elsevier Science Publishers B.V.
- Lange, M. A.; T. J. Ahrens; and M. B. Boslough (1984b). Impact cratering and spall failure of gabbro. *Icarus* 58, 383-395.
- Marvin, U. B. (1984). A meteorite from the moon. *Smithson. Contrib. Earth Sci.* 26, 95-103.
- Maurer, W. C. and J. S. Rinehart (1960). Impact crater formation in rock. *J. Appl. Phys.* 31, 1247-1252.
- McSween, H. Y. (1985). SNC Meteorites: Clues to Martian petrologic environment? *Rev. Geophys.* 23, 391-416.
- McSween, H. Y. and E. Stolper (1980). Basaltic meteorites. *Sci. Amer.* 242, 54-63.
- Melosh, H. J. (1987). High-velocity solid ejecta fragments from hypervelocity impacts. Proc. 1986 Hypervelocity Impact Symp., *Int. J. Impact Engineering* 5, 483-492.

- Melosh, H. J. (1985). Ejection of rock fragments from planetary bodies. *Geology* **13**, 144-148.
- Melosh, H. J. (1984). Impact ejection, spallation, and the origin of meteorites. *Icarus* **59**, 234-260.
- Moore, H. J.; D. E. Gault; and R. V. Lugin (1963). Experimental impact craters in basalt. *Trans Soc. Mining Engineers* **226**, 258-262.
- O'Keefe, J. D. and T. J. Ahrens (1985). Impact and explosion crater ejecta, fragment size, and velocity. *Icarus* **62**, 328-338.
- Polansky, C. A. and T. J. Ahrens (1985). Spall velocity measurements of laboratory scale impact craters (abstract). In *Lunar Planet. Sci. XVI*, p. 671-672. Lunar and Planetary Institute, Houston.
- Stump, B. W. and R. E. Reinke (1984). Spall observations and mechanisms in alluvium. *J. Geophys. Res.* **89**, 495-506.
- Vickery, A. M. (1986). Size-velocity distribution of large ejecta fragments. *Icarus* **67**, 224-236.
- Vickery, A. M. and H. J. Melosh (1987). The large crater origin of SNC meteorites. *Science* **237**, 738-743.
- Wood, C. A. and L. D. Ashwal (1981). SNC meteorites: Igneous rocks from Mars. *Proc. Lunar Planet. Sci. Conf. 12B*, 1359-1375.

Paper 2

**Craters in Carbonate Rocks:
An Electron Paramagnetic Resonance Analysis
of Shock Damage**

CRATERS IN CARBONATE ROCKS:
AN ELECTRON PARAMAGNETIC RESONANCE ANALYSIS
OF SHOCK DAMAGE

Carol A. Polanskey and Thomas J. Ahrens
Division of Geological and Planetary Sciences
California Institute of Technology
Pasadena, California 91125

Contribution number 4704 from the Division of Geological and Planetary Sciences,
California Institute of Technology, Pasadena, California 91125

Abstract

Carbonate samples from the nuclear explosion crater, OAK, and a terrestrial impact crater, Meteor Crater, were analyzed for shock damage using electron paramagnetic resonance, EPR. The first series of samples for OAK Crater were obtained from six boreholes within the crater, and the second series were ejecta samples recovered from the crater floor. The degree of shock damage in the carbonate material was assessed by comparing the sample spectra to spectra of Solenhofen limestone, which had been shocked to known pressures.

The results of the OAK borehole analysis have identified a thin zone of highly shocked carbonate material underneath the crater floor. This zone has a maximum depth of approximately 200 ft below sea floor at the ground zero borehole and decreases in depth towards the crater rim. A layer of highly shocked material is also found on the surface in the vicinity of the reference borehole, located outside the crater. This material could represent a fallout layer. The ejecta samples have experienced a range of shock pressures.

It was also demonstrated that the EPR technique is feasible for the study of terrestrial impact craters formed in carbonate bedrock. The results for the Meteor Crater analysis suggest a slight degree of shock damage present in the β member of the Kaibab Formation exposed in the crater walls.

2.1 Introduction

The purpose of this paper is to analyze shock deformation in carbonate samples taken from OAK Crater, a nuclear explosion crater located on Enewetak Atoll in the equatorial Pacific Ocean, and Meteor Crater, a terrestrial impact crater located near Flagstaff, Arizona. Electron paramagnetic resonance (EPR) spectrometry was used to measure the peak shock stress experienced by a variety of carbonate samples from both craters; however, the focus of this analysis is on the results from OAK Crater. The OAK results are based on EPR spectra from 136 samples taken from six boreholes within and around the crater and 18 ejecta samples recovered from the crater floor. The sampling of Meteor Crater was less comprehensive and consists of eight samples from the crater wall, 12 samples from the continuous ejecta blanket, and eight miscellaneous samples. The Meteor Crater study presented here is a preliminary investigation into the feasibility of applying the EPR analysis technique developed for recent explosion craters to the study of ancient, terrestrial impact craters.

Earlier work relating EPR data to shock deformation was developed by Vizgirda *et al.*, (1980) using core material from beneath a 30 kiloton surface explosion crater, CACTUS Crater. Their work demonstrated a linear relationship between shock pressure and the hyperfine splitting in the EPR spectra that was due to Mn^{2+} substituting for Ca^{2+} in the calcite component of the carbonate. CACTUS was a simple, bowl-shaped crater, and the results of the EPR analysis were fit to a power curve directly relating sample depth to hyperfine splitting. This paper expands upon the previous calibration technique and extends its application to the study of a much larger, gravity-dominated crater.

In this study, shock pressures were determined for the carbonate samples from

OAK Crater by numerically comparing the sample spectrum to standard spectra of Solenhofen limestone, which had been shocked to known pressures in the laboratory. Similarly, several experimentally shocked Kaibab samples were used as a pressure calibration for the Meteor Crater samples. The present approach is an improvement in both sample signal strength and in data reduction.

There is abundant literature linking the study of explosion craters to the study of impact structures, a significant portion of which can be found in Roddy and Pepin (1977). Roddy (1977) shows that impact and explosion craters can be similar in both morphology and structure. In addition, the EPR technique described here can be a useful tool in the analysis of terrestrial impact craters. Of the 150 terrestrial craters suspected to be impact structures (Grolier, 1985), at least 27 were formed within carbonate target rock (Grieve, 1982; Short and Bunch, 1968). There are 14 structures in carbonate rock in the United States alone. The impact crater included in this study, Meteor Crater, Arizona, was formed in sedimentary rocks containing the Kaibab limestone, a sandy dolomitic limestone (Shoemaker and Kieffer, 1974). The Kaibab formation makes up a significant portion of the crater wall and is strongly represented in the continuous ejecta blanket.

OAK Crater is almost the same diameter as Meteor Crater (1200m vs 1100m, respectively); however, it is much shallower (60 m vs 197 m, respectively). Therefore, the diameter/depth ratio for OAK Crater is much higher than that of Meteor Crater (20 vs 6.0, respectively). OAK Crater's high aspect ratio may be a result of the lower energy coupling of a surface nuclear explosion as compared to an impact. The empirical energy coupling factor for nuclear explosives is given as 0.08 by Knowles and Brode (1977), and is close to the value given by O'Keefe and Ahrens (1982), who find an energy-coupling factor of slightly less than 0.1 for a model cometary impactor of density 0.01 g/cm^3 . We infer that the study of explosion craters such

as OAK may increase our understanding of similar craters from cometary impacts. Here, we initially discuss properties of the EPR spectrum of Mn^{2+} in carbonate rocks and the details of how the spectra were obtained and analyzed. Then we discuss the specifics of the OAK crater sample analysis. These results will be used to interpret the structure of OAK crater. Finally, we will discuss the feasibility of applying this technique to the study of Meteor Crater.

2.2 The EPR Spectrum of Mn^{2+} in Carbonates

2.2.1 Powdered calcite

The EPR (also referred to as electron spin resonance, or ESR) spectrum of powdered calcium carbonate, CaCO_3 , is a result of Mn^{2+} substituting for Ca^{2+} in a single site in the crystal lattice. The theory of Mn^{2+} resonance absorption in single-crystal calcite is described by Hurd *et al.* (1954). The Mn^{2+} ion has an effective spin of $\frac{S=5}{2}$ and a nuclear spin of $\frac{I=5}{2}$, which give rise to a total of 30 transitions. The calcite spectrum exhibits both fine and hyperfine structure but is dominated by the six hyperfine peaks from the central transitions $M_S = \pm\frac{1}{2}$, and $\Delta m_I = 0$, where M_S is the electronic magnetic quantum number, and m_I is the nuclear magnetic quantum number. The hyperfine peak splitting results from the coupling between electronic and nuclear magnetic moments (Hurd *et al.*, 1954). Another feature of the spectrum are the forbidden transition peaks, $\Delta m_I = 1$, which are less prominent and occur in pairs between the central transitions (Mankowitz and Low, 1970). The spectrum of a powdered sample of single-crystal calcite, Iceland spar, is shown in Figure 2.1. The central transitions are labeled along with the forbidden transitions. Of particular

CALCITE POWDER SPECTRUM

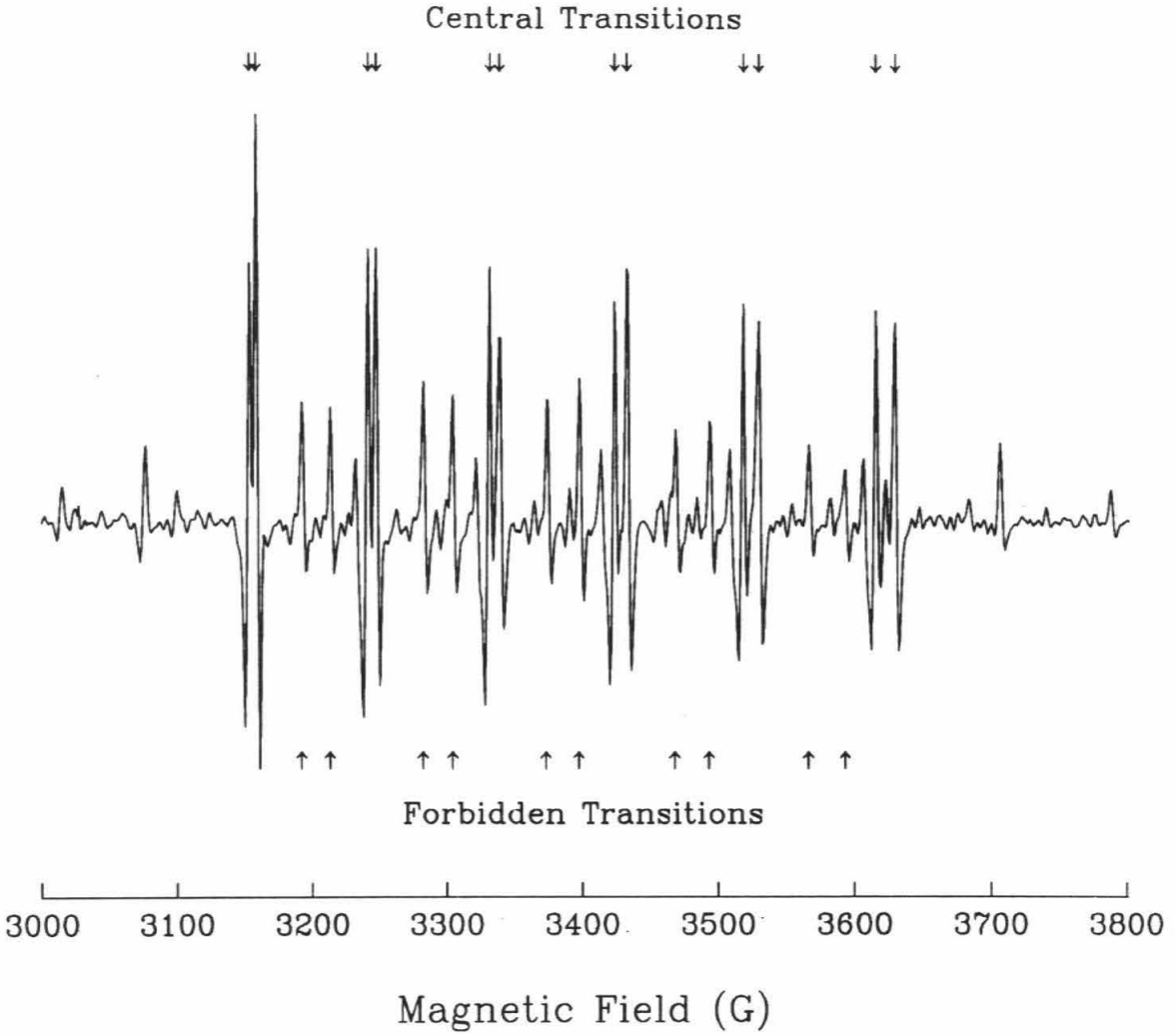


FIGURE 2.1 : EPR spectrum of powdered single-crystal calcite. The central transitions are due to $M_S = \pm\frac{1}{2}$, $\Delta m_I = 0$, where M_S and m_I are the electronic and nuclear magnetic quantum numbers, respectively. The forbidden transitions occur when $\Delta m_I = 1$.

interest to this study are the two outermost peak doublets at the lowest and highest magnetic field positions of the sextet.

2.2.2 Coralline limestone samples from OAK Crater

The material hereafter referred to as "carbonate" in the OAK study is a coralline limestone composed of a mixture of calcite and aragonite. Blanchard and Chasteen (1976) have studied both the calcite and the aragonite components of a sea shell using EPR methods. The spectra of Mn^{2+} in the calcite portion of the shell resemble that of single-crystal calcite; however, no EPR signal was obtained at either room temperature or liquid nitrogen temperatures for powdered samples of the aragonitic portion. Work by Low and Zeira (1972) also describe the lack of an EPR spectrum that is due to Mn^{2+} in both single crystals and powdered aragonite. They also state that calcite formed from aragonite at low temperatures, such as the case in the Enewetak samples, shows the typical Mn^{2+} calcite spectrum. Therefore, it is assumed that the spectra obtained in this study are due entirely to the calcite component of the sample.

2.2.3 Kaibab dolomitic limestone samples from Meteor Crater

Meteor Crater was formed in sedimentary bedrock containing the Kaibab Formation. The Kaibab consists of fossiliferous marine sandy dolomites, dolomitic limestones, and calcareous sandstones (Shoemaker and Kieffer, 1974). This formation is exposed on the crater walls and is part of the remaining continuous ejecta blanket. The EPR spectrum of Mn^{2+} in dolomite is similar to the OAK carbonates; however, it differs in two important respects. First, the spectrum is affected by the presence of two different cations, Mg^{2+} and Ca^{2+} , within the dolomite structure (Wildeman, 1970).

Because of the difference between the Mg^{2+} and Ca^{2+} ions, the dolomite spectrum has a different character from that of the pure calcite limestone spectrum. Secondly, the Mn^{2+} impurities occupy the Mg^{2+} sites as well as the Ca^{2+} sites. Past measurements indicate a preference for Mn^{2+} to occupy the Mg site over the Ca site (Vinokurov *et al.*, 1961; Prissok and Lehmann, 1986).

2.3 Sample Preparation and Spectrometer Measurements

Carbonate samples were ground into a coarse powder and placed into Wilmad 707SQ fused-quartz EPR tubes. EPR spectra were taken at room temperature with a Varian E-Line Century Series spectrometer. The Mn^{2+} feature occurs from approximately 3150 to 3650 Gauss, and is centered near 3400 Gauss (where the spectroscopic splitting factor is $g = 2$). The spectrometer was set at a microwave frequency of 9.56 GHz, microwave power of 20 mWatt, modulation amplitude of 3.2 G, and time constant of 0.25 sec. To remove the slope from the spectrum and reduce the line width of the signal, the spectrometer was operated in the second derivative mode. The second derivative of the signal is obtained by setting the modulation frequency of the cavity 90 degrees out of phase with the receiver frequency.

A spectrometer scan time of 8 minutes was used to obtain the full spectrum over a 1000 G scan range; however, high-resolution spectra were also recorded of both the extreme lower and the higher field components of the spectrum. For the high-resolution spectra, the magnetic field was swept over 100 G in 4 minutes. These spectra provided greater detail of the modification of the hyperfine doublets from the shocked samples, and were used in all the subsequent quantitative analyses. In addition, all spectra were recorded digitally. Therefore, it was possible to average

several scans to improve the signal-to-noise ratio in samples with low signal strength. Signal averaging proved to be extremely useful for the highly shocked coralline samples, as there is a correlation between decreasing signal strength and increasing shock pressure.

2.4 Shock-wave calibration experiments

The calibration data set is a combination of three series of shock-wave experiments. The first series consisted of carbonate samples from Cactus crater shocked in the laboratory over 10 years ago. The samples were taken from two different depths, 10' and 146', from the borehole XRU-3 located outside of CACTUS crater on Enewetak Atoll. These samples and experiments are described in detail by Vizgirda *et al.* (1980). The principal motivation for reprocessing these samples was to answer the question of whether or not the shock effects observed by Vizgirda *et al.* had changed with time. New spectra were taken of each sample, and the results confirmed that the effect of shock on the hyperfine splitting had not altered on the timescale of a decade. Secondly, high-resolution, digital spectra were taken of these samples in order to test the pressure calibration technique.

The second series of experiments provided the data used to develop the pressure calibration technique used in this paper. The pressure calibration for the coralline Enewetak carbonates was based on six Solenhofen limestone samples shocked to known pressures in the laboratory. Solenhofen limestone was chosen as a calibration standard for the OAK analysis because its EPR spectrum, which was also due to Mn^{2+} substitution, is orders of magnitude more intense than the spectra from the Enewetak carbonates. The limestone is also more chemically homogeneous, although

it is still a polycrystalline material.

The third series of calibration samples consisted of shocked Kaibab dolomitic limestone taken from the walls of Meteor Crater. This calibration was used to determine the degree of shock damage in the remainder of the Meteor Crater samples. However, the standard Kaibab comparison spectra were constructed from averages of spectra from five samples taken from Diablo Canyon. Diablo Canyon is far enough away from the crater so that the samples should not have been affected by the impact. The Kaibab EPR spectra also has a strong Mn^{2+} signature of similar amplitude to the Solenhofen limestone.

Cores of sample material, 0.64 cm in diameter, were cut into cylinders 1 cm in length and pressed into stainless steel sample chambers. The sample chambers were sealed in the rear by a stainless steel plug which was notched to vent any impact generated gases. The sample chamber was then inserted into a large stainless steel momentum trap and mounted in a 40 mm propellant gun. Lexan projectiles containing flyer plates of aluminum or lexan impacted the target assembly at velocities between 0.8 and 1.6 km/sec to yield initial shock pressures of 1.3 to 9.8 GPa and 0.7 to 2.0 GPa for the Solenhofen and Kaibab samples, respectively. Initial shock pressure, rather than final, reverberated shock pressure is quoted because most of the entropy generated by the shock, and hence the shock damage, is associated with the initial shock wave.

Shock pressures were calculated using the projectile velocities and the impedance match technique (Stoffler, 1972). The average bulk density of the limestone samples was 2.61 g/cm^3 , and the Hugoniot data for Solenhofen limestone were taken from Tyburczy and Ahrens (1986) and Ahrens and Gregson (1964). A Hugoniot for the alpha member of the Kaibab limestone (2.22 g/cm^3) was measured by Isbell *et*

HUGONIOT DATA FOR CARBONATE ROCKS

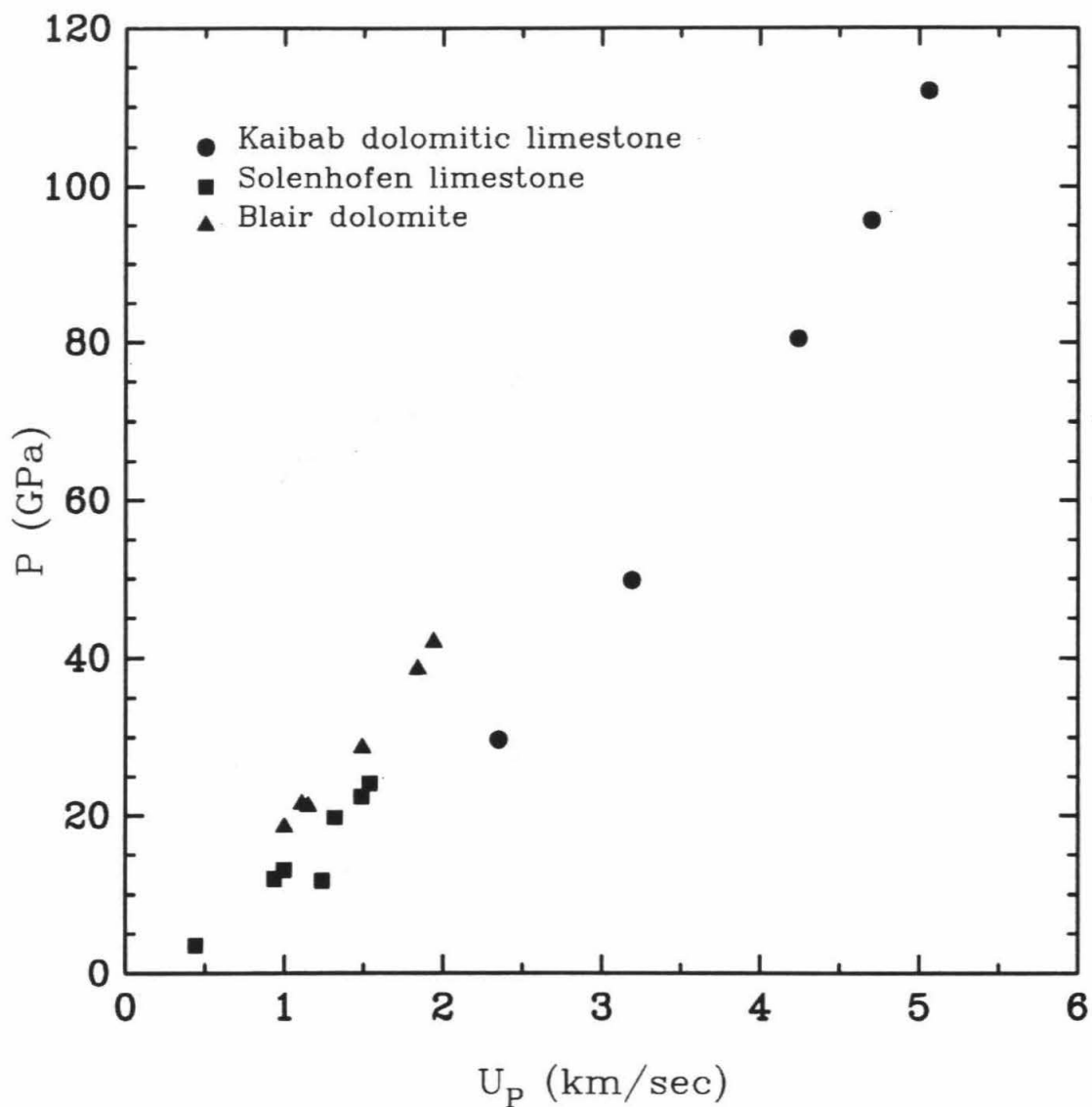


FIGURE 2.2 : Hugoniot data for three carbonate rocks: Solenhofen limestone, Kaibab dolomitic limestone, and Blair dolomite.

TABLE 2.1

Shock Wave Data

Material	Density (g/cm ³)	C ₀ (km/sec)	s
lexan	1.196	2.631	1.295
aluminium (2024)	2.784	5.370	1.290
steel (304)	7.890	4.580	1.490
Solenhofen limestone	2.61	3.269	1.796
Kaibab dolomitic limestone	2.22	2.10	1.53

al.(1966) for shock pressures between 30 to 112 GPa. Figure 2.2 shows a comparison between the Solenhofen and Kaibab Hugoniot. The Hugoniot for Blair dolomite is also included for comparison (Grady *et al.*, 1976). The remaining Hugoniot for lexan, aluminum 2024, and stainless steel 304 were found in Marsh (1980). The shock wave data are listed in Table 2.1.

2.4.1 Description of shocked Solenhofen limestone spectra

Figure 2.3a shows the series of shocked limestone spectra. The spectra have all been normalized such that the highest peak of each sample is equal to one. The shocked limestone spectra not only reflect the decrease in the hyperfine splitting observed earlier by Vizgirda *et al.* (1980) in the carbonate spectra, but also reveal that the relative signal strength and width of the two subpeaks vary in a consistent manner with increasing pressure. It is clear from the second and third column in Figure 2.3a that the outermost peak in each doublet decreases in relative amplitude and broadens with increasing shock pressure. This alone may be the cause of the decrease in splitting observed, and an actual shift in line position may not be required.

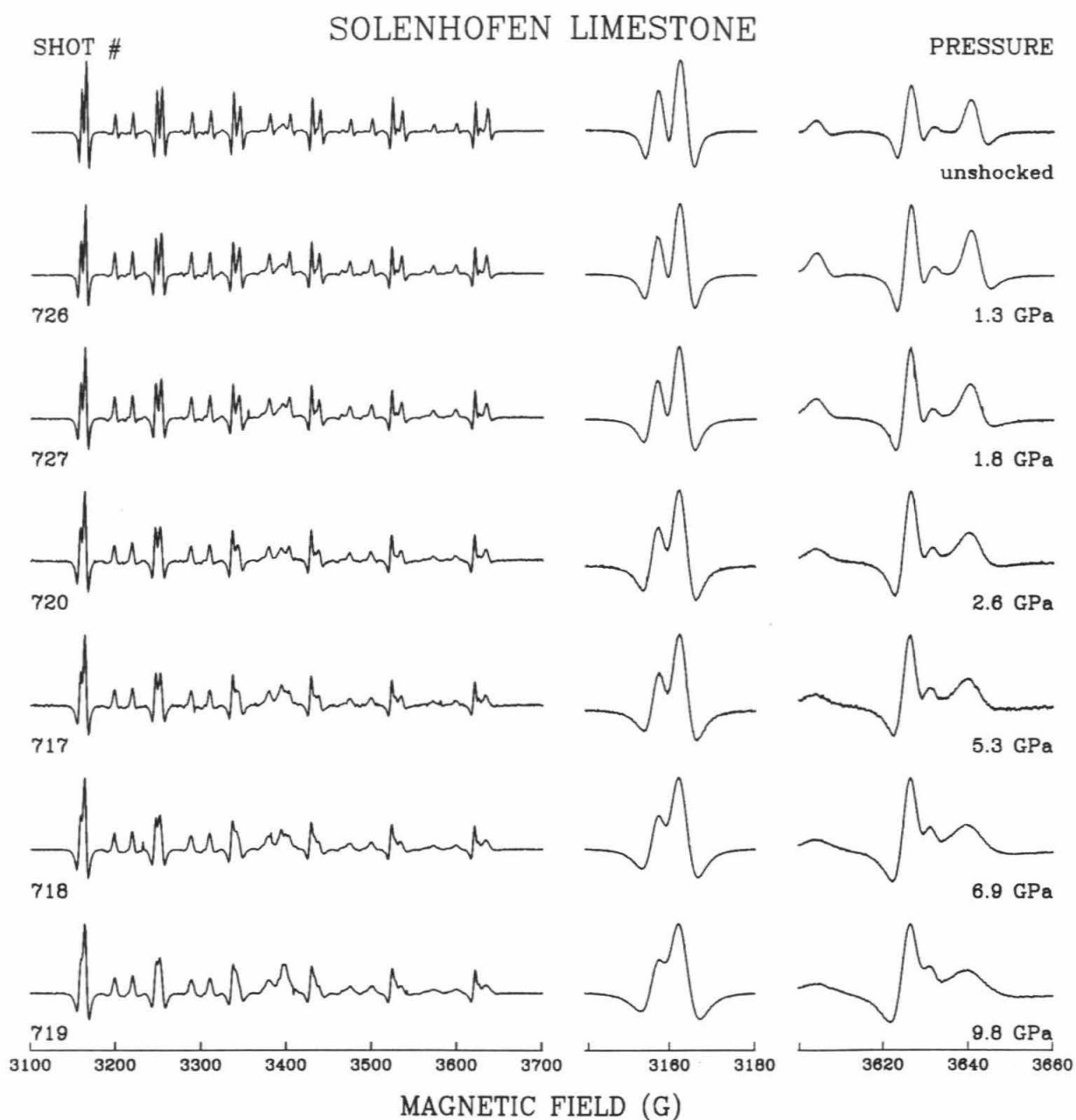


FIGURE 2.3a: Comparison of Solenhofen limestone spectra shocked in the laboratory. The first column shows the full spectrum centered at 3400 G, while the second and third columns show the high-resolution spectra of the lowest and highest field components centered at 3160 G and 3630 G, respectively.

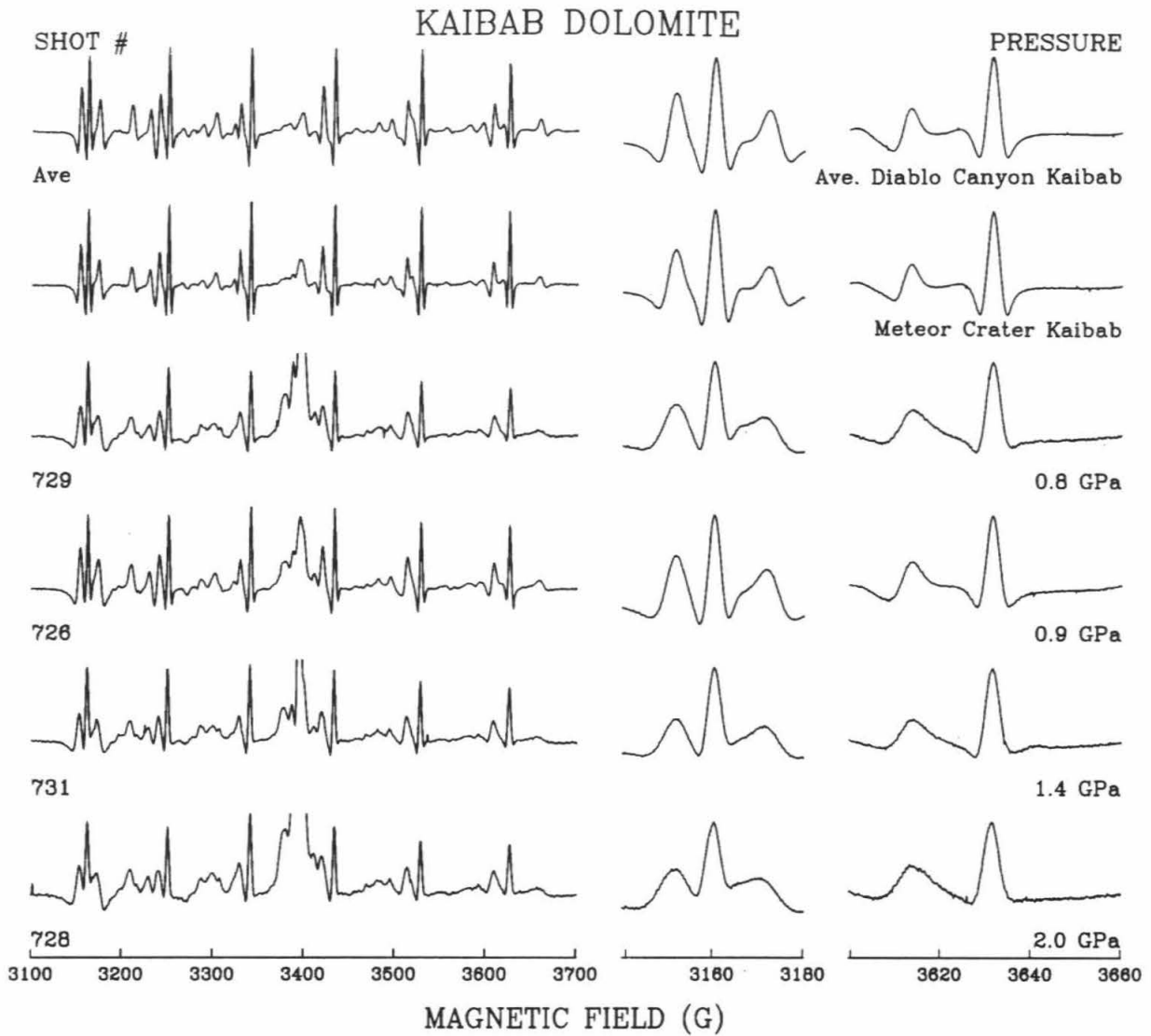


FIGURE 2.3b: Comparison of Kaibab limestone spectra shocked in the laboratory. The first column shows the full spectrum centered at 3400 G, while the second and third columns show the high-resolution spectra of the lowest and highest field components centered at 3160 G and 3630 G, respectively.

The specific behavior of the subpeaks in the high-field doublet of the carbonate samples from OAK crater is less obvious and becomes difficult to detect in samples subjected to high shock pressures. The high field doublet eventually becomes completely lost in the noise (as seen in the sample shocked to 10 GPa). A second observation, mentioned earlier, is that the amplitude of the entire spectrum tends to decrease with increasing shock pressure. This effect is much more obvious in the carbonate samples than in the limestone. A loss of signal could be due to a reduction of the Mn^{2+} concentration in the Ca^{2+} lattice sites or the phase transition of calcite to aragonite during shock loading. However, the specific mechanism responsible for this reduction has not yet been identified.

2.4.2 Description of shocked Kaibab limestone spectra

Similarly, the series of shocked Kaibab samples is shown in Figure 2.3b. One obvious difference in the Kaibab spectra is that the low field component of the sextet is a triplet rather than a doublet. In general, although the sextet is still present, each of its components differs from its counterpart in the Solenhofen spectrum. In addition, the forbidden transitions are not as well defined. Despite these differences, the effect of increasing shock pressure appears to have a similar effect on the spectra. Both the low and the high field components broaden with increasing shock pressure, and the relative heights of the lesser subpeaks in each sextet decrease with respect to the highest subpeak.

2.5 Pressure calibration by differencing spectra

The previous calibration technique of Vizgirda *et al.* (1980) relied on measuring

the separation, in Gauss, of the two subpeaks of the highest field component of each spectrum. The hyperfine peak splitting, HPS, was related to shock pressure, P, by the relationship,

$$HPS(G) = -0.60P(GPa) + 13.85 \quad (\text{high field}).$$

Although the decrease in hyperfine splitting is most evident in the high field component, the signal strength of this peak is also the lowest. Therefore, as the signal intensity decreases, the error in measuring hyperfine peak splitting increases. The following technique was developed to incorporate the variations in hyperfine splitting as well as relative peak amplitudes and widths. In addition, the analysis will work equally well for the lowest field component of the spectrum, which generally has a higher amplitude than the highest field component.

Digital spectra were used to compare each carbonate sample to a standard. The standard chosen for the Solenhofen limestone and Enewetak carbonates was single-crystal calcite, while the the standard for the Meteor Crater samples was the wall sample used as material for the shock-wave experiments. Both high-resolution spectra from each end of the spectrum were used in the comparison. The digital spectra consisted of 1000 amplitude values evenly spaced over a 100 G field range. Both sample and standard spectra were first normalized by the amplitude of their respective highest subpeaks. The sample spectrum was then translated along the magnetic field axis until the position of its highest subpeak coincided with that of the standard spectrum. Next, the absolute value of the difference in amplitude between the two spectra was calculated for each point over the extent of the doublet. Finally, these individual differences were summed to determine a measure of the "likeness" or the "unlikeness" of the sample spectrum to the standard. This number shall be referred

to as the integrated difference, or ID, of the sample, which is given analytically by

$$ID = \sum_{i=n_0}^{n_0+N} \frac{|Y_{standard}(i) - Y_{sample}(i)|}{N + 1}, \quad (1)$$

where n_0 is the index of the amplitude array corresponding to a magnetic field value 20 G below that of the highest peak of the standard spectrum. $Y_{standard}(i)$ and $Y_{sample}(i)$ are the normalized amplitudes of the standard and sample spectra, respectively, and N is the number of data points that are integrated. In the case of the calcite spectra, N was chosen as 400, corresponding to 40 G. However, the peaks in the Kaibab spectra are broader than the limestone spectra, so ID was calculated for 60 G, or $N = 600$. The error in ID is determined by performing a similar calculation, where $Y_{sample}(i)$ are points in the flat baseline signal on either side of the Mn^{2+} peak.

Figure 2.4 illustrates the application of this procedure on two spectra from the limestone calibration experiments. Figure 2.4 a shows an unshocked, Solenhofen limestone spectrum normalized, translated, and plotted over the standard, calcite spectrum. The absolute value of the difference between the amplitudes at each point over a 40 G range in magnetic field is shown in Figure 2.4 b. Figures 2.4 c and d demonstrate the same technique applied to a limestone sample that has been shocked to 9.8 GPa. The error is determined by using the same scheme to calculate the integrated difference along a flat portion of the spectrum. This value gives an estimate of the contribution of noise to the ID over the region containing the signal.

The results of these calculations for the limestone calibration experiments are plotted in Figure 2.5a. The ID values are plotted versus pressure for both the low and the high field components of the spectrum. To determine the pressure to integrated-difference calibration, a line was fit to each data set, using linear least squares. The resulting equations are

$$P_{Solenhofen}(GPa) = 116(ID) - 5.97 \quad \text{low field}; \quad (2a)$$

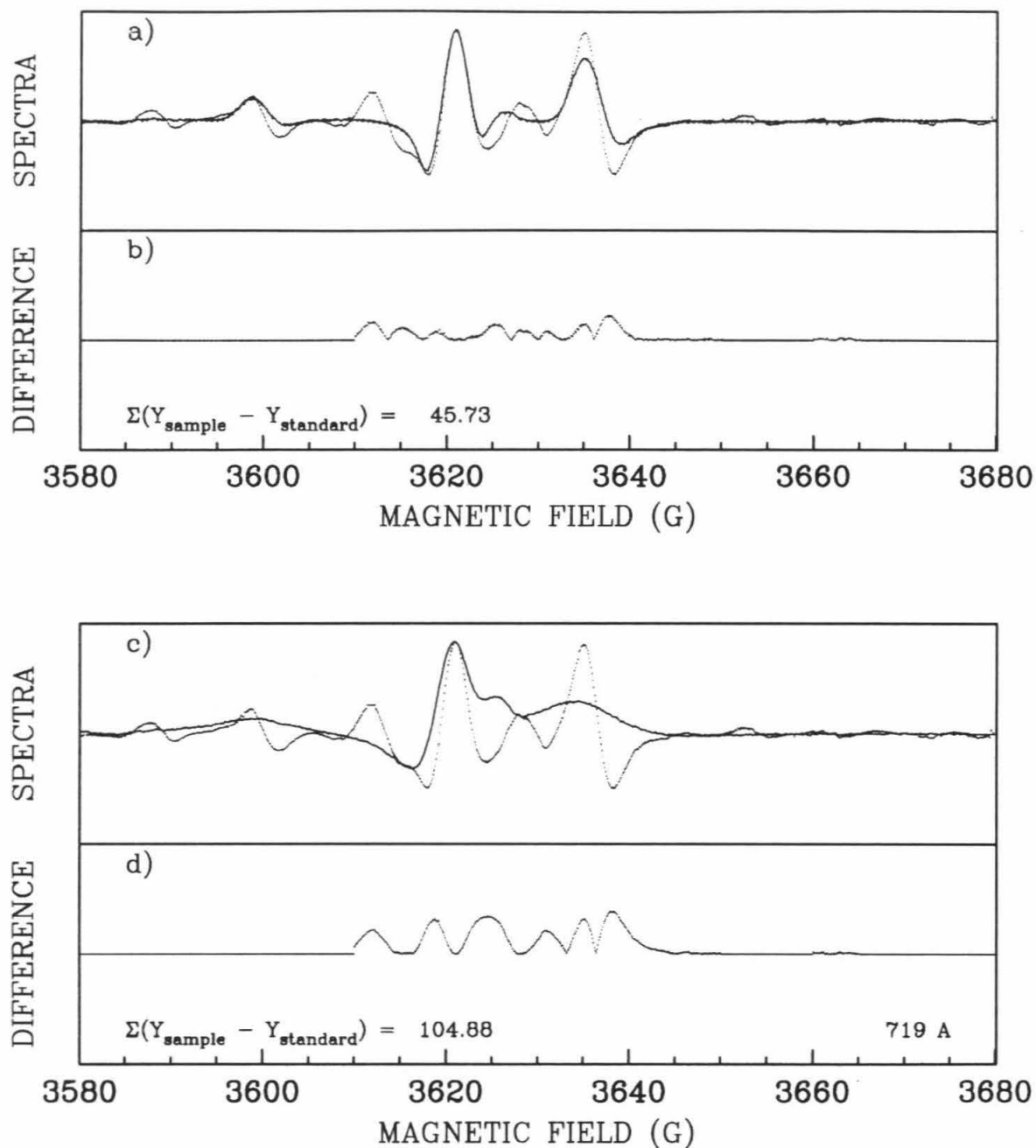


FIGURE 2.4 : Example of the differencing technique, showing a) an overlay of the standard spectra and an unshocked Solenhofen limestone sample, and b) a plot of the individual absolute differences at each point along the field. Frames c) and d) are the same as a) and b) for limestone shocked to 9.8 GPa.

SOLENHOFEN LIMESTONE

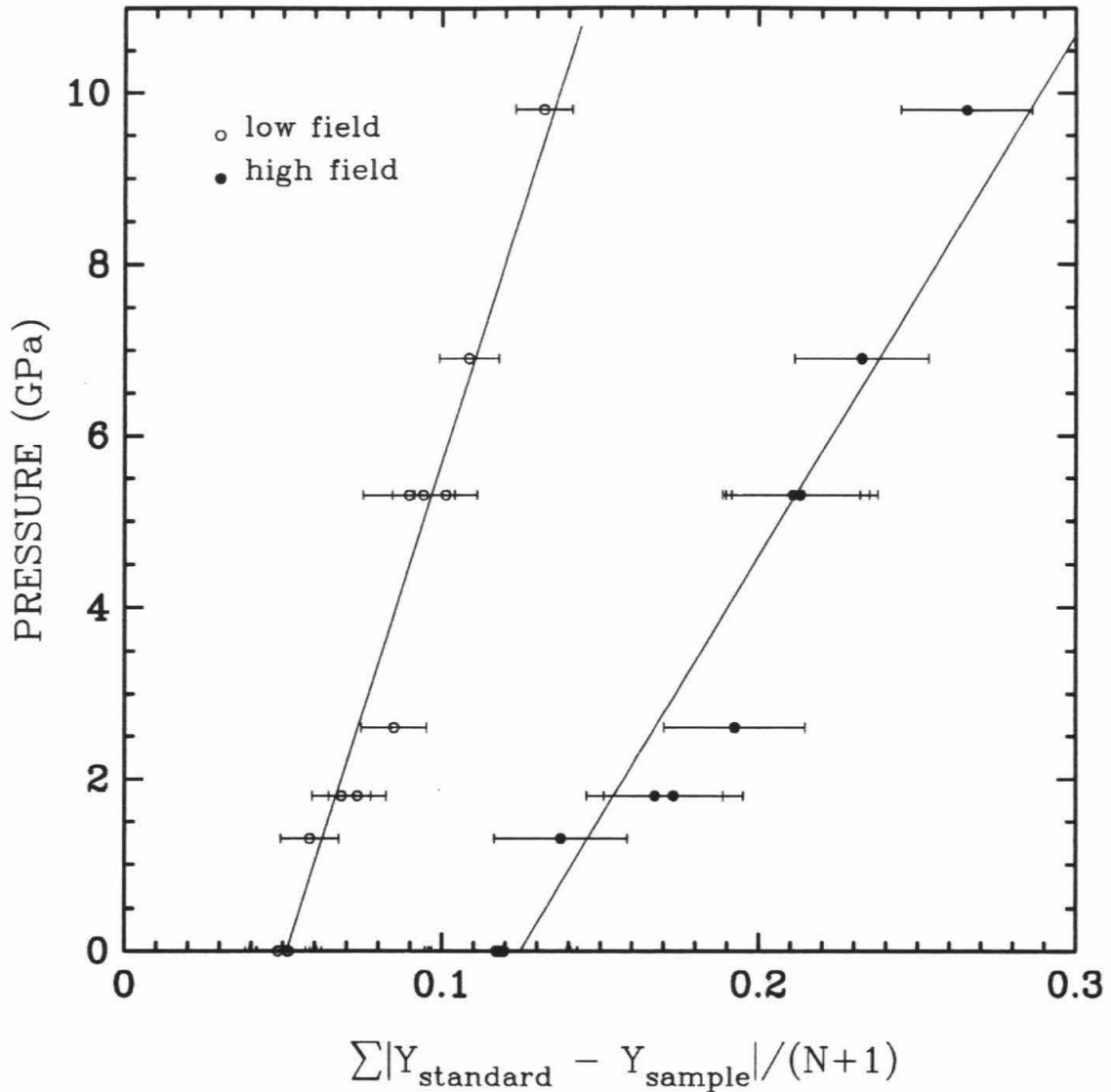


FIGURE 2.5a: Plot of the summed differences for the low and high field components of the Solenhofen limestone samples as a function of shock pressure. The ID value is calculated over a range of 40 G.

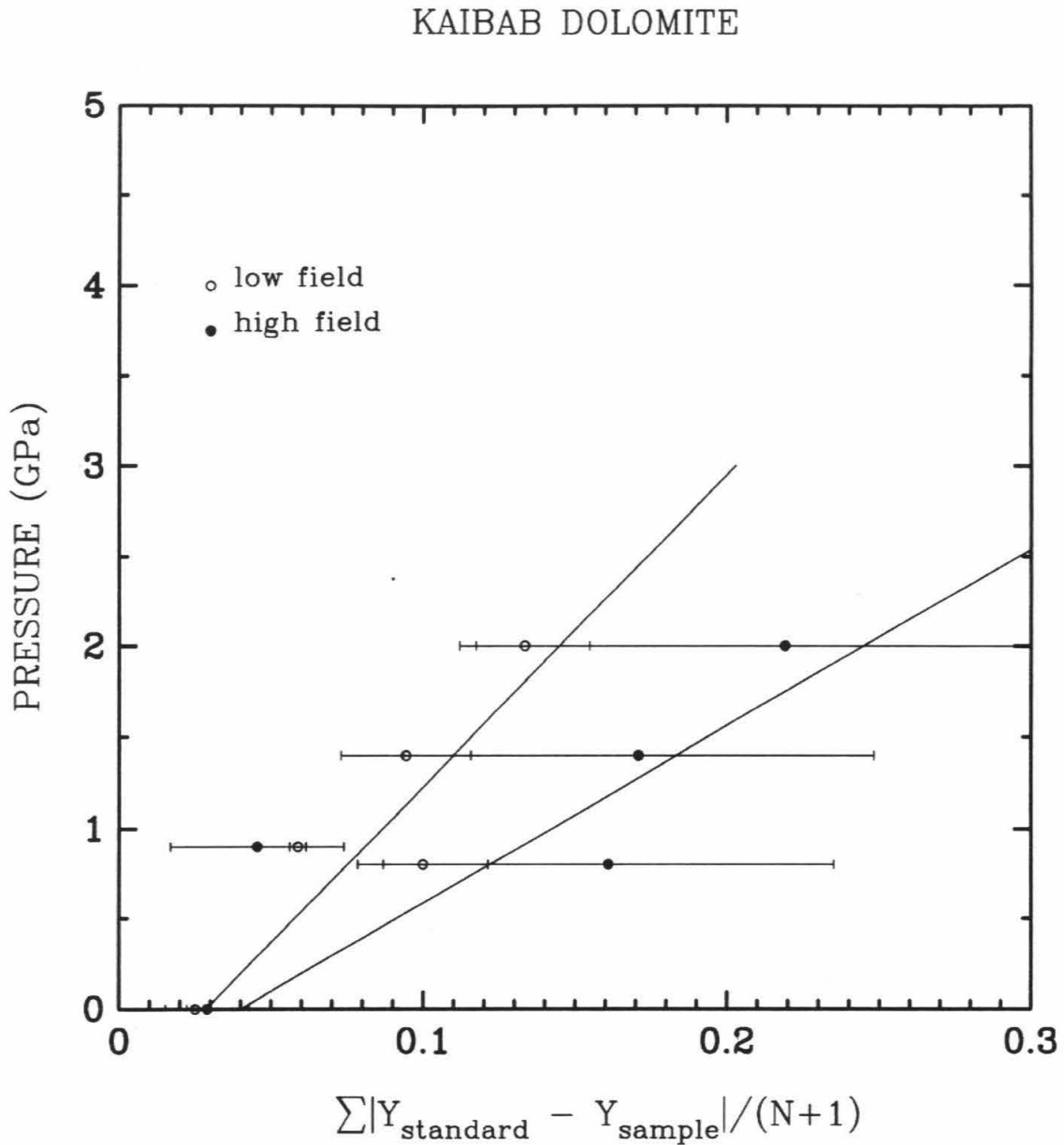


FIGURE 2.5b: Plot of the summed differences for the low and high field components of the Kaibab dolomitic limestone samples as a function of shock pressure. The ID value is calculated over a range of 60 G.

$$P_{Solenhofen}(GPa) = 61.0(ID) - 7.60 \quad \text{high field.} \quad (2b)$$

The correlation coefficients for the fit were 0.983 and 0.971, respectively. Table 2.2 contains a list of the ID results for the limestone experiments. The average ID values are given for shots where several samples were analyzed. Using the calibration curves above, shock pressures were then assigned to the OAK carbonate samples. In general, the carbonate samples have a much weaker EPR signal than the limestone. Therefore, it was necessary to adjust the intercept of the calibration curves to compensate for the average ID value of the unshocked carbonate samples. It follows that this method will then assign negative pressures to some samples, because the previous adjustment was made to accommodate the “average” background noise. To avoid this obviously unphysical result, and because this technique is not extremely sensitive for low shock damage, all samples with shock pressures calculated to be below 2.0 GPa were classified simply as unshocked. Similarly, the high-pressure cutoff was chosen to be 15 GPa. This is necessary because there are no data for very high shock pressures, and the intensity of the carbonate spectrum is low even at 10 GPa. In most cases, shock pressures were calculated for each sample using both the low and high field components of the spectrum. These values were then averaged to determine the final calculated pressure.

Similarly, a calibration curve was determined for the Kaibab experiments (Figure 2.5b). However, the Kaibab data covered only the low end of the pressure range sampled in the Solenhofen experiments. The fit to the Kaibab data is

$$P_{Kaibab}(GPa) = 17.2(ID) - 0.494 \quad \text{low field,} \quad (3a)$$

$$P_{Kaibab}(GPa) = 9.77(ID) + 0.391 \quad \text{high field,} \quad (3b)$$

where the correlation coefficients for these curves were 0.926 and 0.940, respectively. The slopes of Equations 3a and 3b are significantly less than the slopes calculated for

TABLE 2.2

Pressure (Giga Pascal) and Integrated Difference (ID) Data
for High-Resolution Spectra from Samples Shocked in Laboratory Recovery Experiments

Solenhofen limestone			
Shot #	P (GPa)	ID Low Field	ID High Field
—	0.0	0.0518	0.1187
726	1.3	0.0585	0.1375
727	1.8	0.0709	0.1701
720	2.6	0.0848	0.1924
717	5.3	0.0951	0.2123
718	6.9	0.1086	0.2324
719	9.8	0.1322	0.2654
Kaibab dolomite			
Shot #	P (GPa)	ID Low Field	ID High Field
—	0.0	0.0251	0.0290
729	0.8	0.0999	0.1610
726	0.9	0.0588	0.0454
731	1.4	0.0944	0.1709
728	2.0	0.1334	0.2190

the Solenhofen limestone experiments. One possible explanation is that this is the result of a sampling bias from computing the calibration for samples in the low-pressure regime. If the Solenhofen calibration was calculated based on only the data up to 2.6 GPa, the slopes would become 71.0 and 31.7 for the low and high field components, respectively. Another factor is that the width of each sextet of the Kaibab spectrum occurs over a greater range of magnetic field than its Solenhofen counterpart. This difference could contribute to higher ID values for Kaibab samples relative to Solenhofen samples experiencing similar shock pressures. Note that no attempt was made to defined low- or high-end pressure cutoffs for the Kaibab calibration because of the

small range of pressures used in the calibration.

2.6 OAK Crater

OAK crater is located along a reef at Enewetak Atoll in the Republic of the Marshall Islands (Figure 2.6). It was formed by an 8.9 Megaton explosive device detonated from a barge approximately 4m above the sea floor. The crater has a maximum radius and depth of 600 m and 60 m, respectively. A detailed description of OAK crater and the geophysical and material studies performed can be found in Folger (1986) and Henry and Wardlaw (1986).

Enewetak Atoll is composed of approximately 40 low-lying islands surrounding the lagoon. OAK is a complex crater formed near the reef of the island. The core samples from OAK were obtained through a drilling and coring effort performed from April through July 1985 (Henry *et al.*, 1986). The rock samples were provided in the form of drill cores 3 inches in inside diameter.

The rock types of the samples are classified according to the nomenclature of Dunham (1962) which describes their depositional fabric or texture. This terminology distinguishes between carbonate rocks bound (cemented or uncemented) by mud (particles of clay or fine-silt size), or by grains (sand -sized and coarser material, particle diameters greater than 20 μm). Rocks bound by mud are referred to as mudstone or wackestone, depending on whether the mud contains less than or greater than 10% grains, respectively. Grain- supported rocks are referred to as packstone or grainstone, where grainstones contain no mud. Other related terms used to describe sample material are "tea-brown micrite," which refers to dark-brown, fine-grained carbonate material, and "sand," which refers to uncemented carbonate fragments with diame-

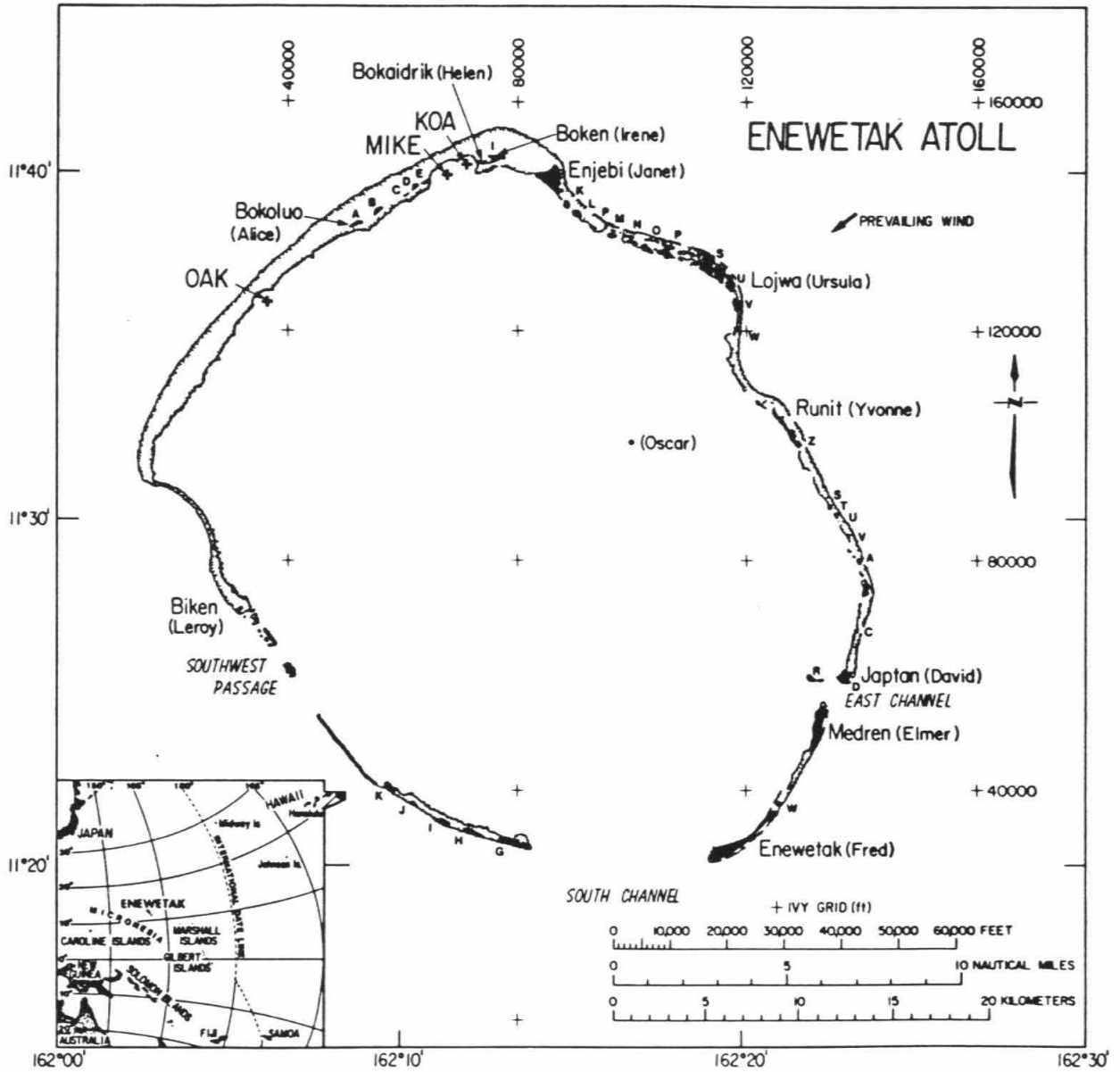


FIGURE 2.6 : Location map of Enewetak Atoll and OAK crater.

ters between $\frac{1}{16}$ and 2 mm. The carbonate rocks in this study have extremely high porosities.

A system of geologic zones defined by Henry and Wardlaw (1986) to describe the stratigraphy beneath the crater. This system will be used later when discussing the results of the borehole sample analysis. The ALPHA zone consists of late-stage sedimentation and slope failures along with material piped to the surface. The BETA 1 zone involves both early and late-stage collapse rubble, and also includes some piped material. The BETA 2 zone is referred to as the transition sands. It has limited lateral extent and contains pulverized sand. Beneath the BETA 2, the rock becomes increasingly less fractured and displaced comprising the BETA 3 and GAMMA zones.

2.6.1 Core sample selection

The core samples consisted of sediments and clasts from the six boreholes OAR-2A, OBZ-4, OCT-5, OET-7, OFT-8, and OPZ-18. These boreholes are located on a northeast crater radial, which is parallel to the geologic strike of the Atoll as illustrated in Figure 2.7. In this paper, core samples will generally be designated by a borehole name and a depth in meters below sea level (m bsl). However, previous works (Polanskey and Ahrens, 1987a; Henry *et al.*, 1986; and others) refer to these samples in feet below sea floor (ft bsf) and feet below sea level (ft bsl), so these depths are also listed for each sample in Appendix A.

The carbonate material from Enewetak is extremely inhomogeneous material containing both calcite and aragonite. As mentioned previously, aragonite does not have a detectable EPR spectrum (Low and Zeira, 1972), therefore, when possible samples were selected for high calcite content. For example, those samples containing

OAK CRATER BOREHOLES

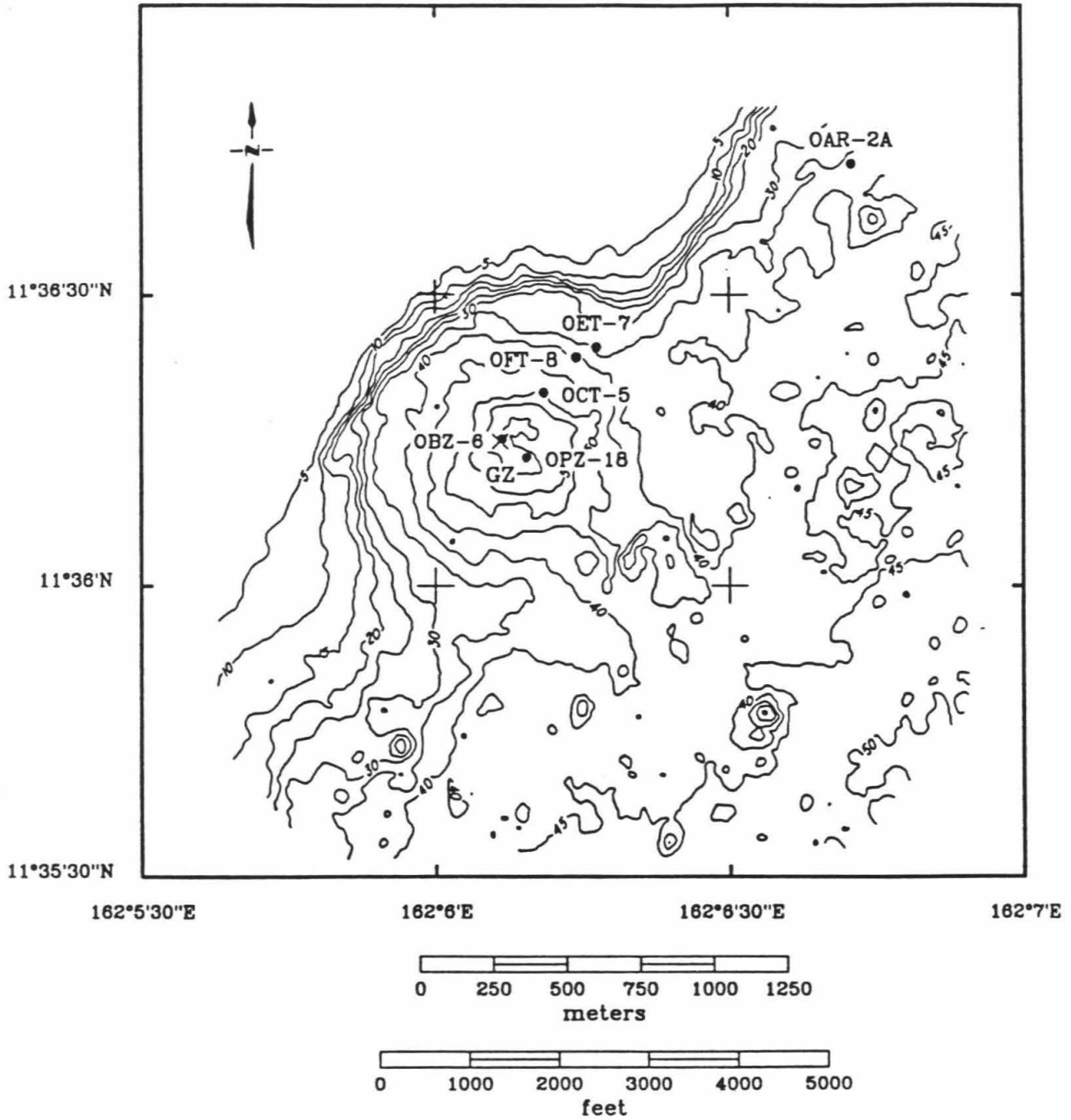


FIGURE 2.7 : Map of OAK crater showing the location of the boreholes sampled in this study.

coral replaced by solution-deposited calcite crystals were preferred, because they had stronger EPR signals. The choice of good sample material is important to the extent that it provides a consistent base for analysis, and guards against mistaking a sample with an inherently poor EPR spectrum as one being heavily shocked. The difference between the two cases can usually be recognized by visual inspection, but is more difficult to assess with numerical techniques. In each core, the majority of samples were taken from depths above the GAMMA geologic zone, defined by Wardlaw and Henry, (1986) as fractured and displaced. A more detailed description of each sample and its spectra can be found in Appendix A as well as Polanskey and Ahrens (1987a). Complete descriptions of the stratigraphy of each borehole are given in Henry *et al.* (1986).

2.6.2 Results of core sample analysis

The two boreholes located directly below the position of the explosive device, ground zero boreholes OBZ-4 and OPZ-18, were the most heavily sampled cores. A very highly shocked layer of uncemented material was found in OPZ-18 between 121.9 and 126.8 m bsl. This layer was visually distinguishable by the unusual greenish color of the carbonate sand. The shocked zone was broken at 125.7 m bsl by a thin zone of lighter colored material. The location and nature of this shocked material coincide with a zone of Holocene sediments described by Wardlaw and Henry (1986) as a possible example of material that has been injected. The present results are consistent with such a hypothesis since this material most likely originated near the pre-shot seafloor surface. Three other sand samples above this layer, 117.9, 112.3, and 108.9 m bsl, were shocked to low levels. The heavily shocked samples were located primarily in the geologic zone BETA 2, the transition sands, while the lightly shocked material came from the zone BETA 1 (Wardlaw and Henry, 1986). The remaining

24 of the 31 samples appear to be unshocked. Remarkably, not one of the samples from OBZ-4 showed signs of significant shock damage. There were 3 samples from the BETA 1 zone that did register marginally detectable degrees of shock damage. Sufficient samples were analyzed from the transition sands and vicinity to characterize the core; therefore, it appears that OBZ-4 did not share the same history as OPZ-18.

Thick zones of highly shocked material were found in each of the three north-eastern radial transition boreholes OCT-5, OET-7, and OFT-8. The transition sands have not been identified in any of these boreholes; however, the spectra of the shocked material are similar to those from the shocked material in OPZ-18.

Spectra were taken of 25 samples from borehole OCT-5. The results of 6 samples define a heavily shocked zone at least 7.5 m thick, extending from 87.0 to 94.4 m bsl. This region occurs within the BETA 1b (early-stage, collapse rubble) zone, and these samples are also primarily uncemented sands. Aside from the highly shocked material in this region, there are 4 widely dispersed samples that appear to be moderately shocked. However, one sample in particular, taken at 141.4 m bsl, is an example of the aforementioned situation, where poor signal quality biases a pressure determination. Simple visual analysis of its spectra suggests that it is actually unshocked. The elevated pressure calculated for this depth is a artifact of the noisiness of the sample.

Borehole OFT-8 is located just within the excavational crater (Henry *et al.*, 1986). In this case, the region of heavily shocked material begins near the top of the BETA 1b zone and extends downward for approximately 8 m. Included within this zone were 7 heavily shocked samples located between 46.8 and 55.1 m bsl. Bordering this region above and below are zones containing moderately shocked material. The next farthest borehole from ground zero was OET-7. Based on seismic reflection, paleontology and litho-stratigraphic analysis data, this borehole is thought to be located outside

OAK CRATER BOREHOLE RESULTS

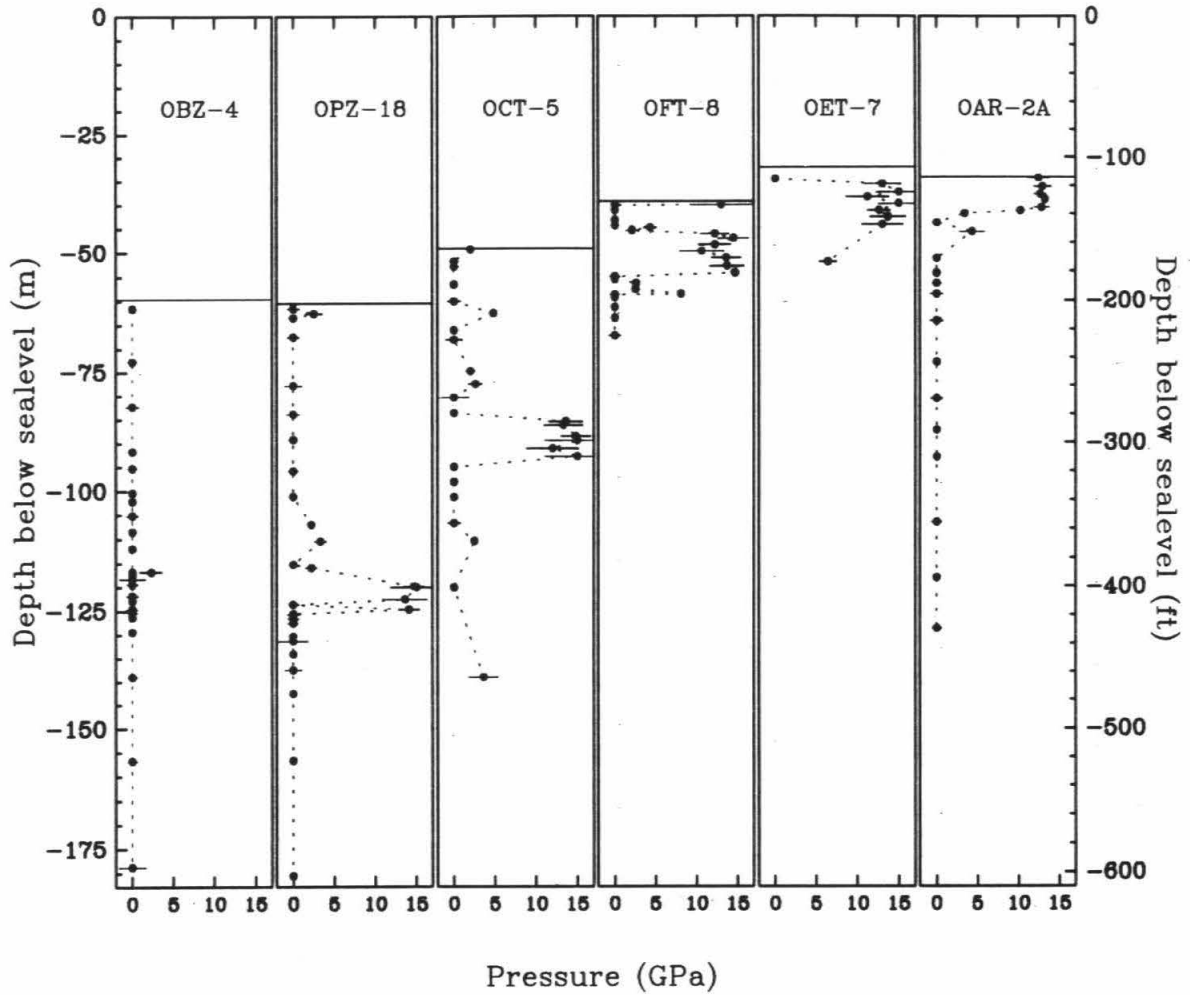


FIGURE 2.8a: Results of the borehole sample analysis showing shock pressure versus depth for each borehole.

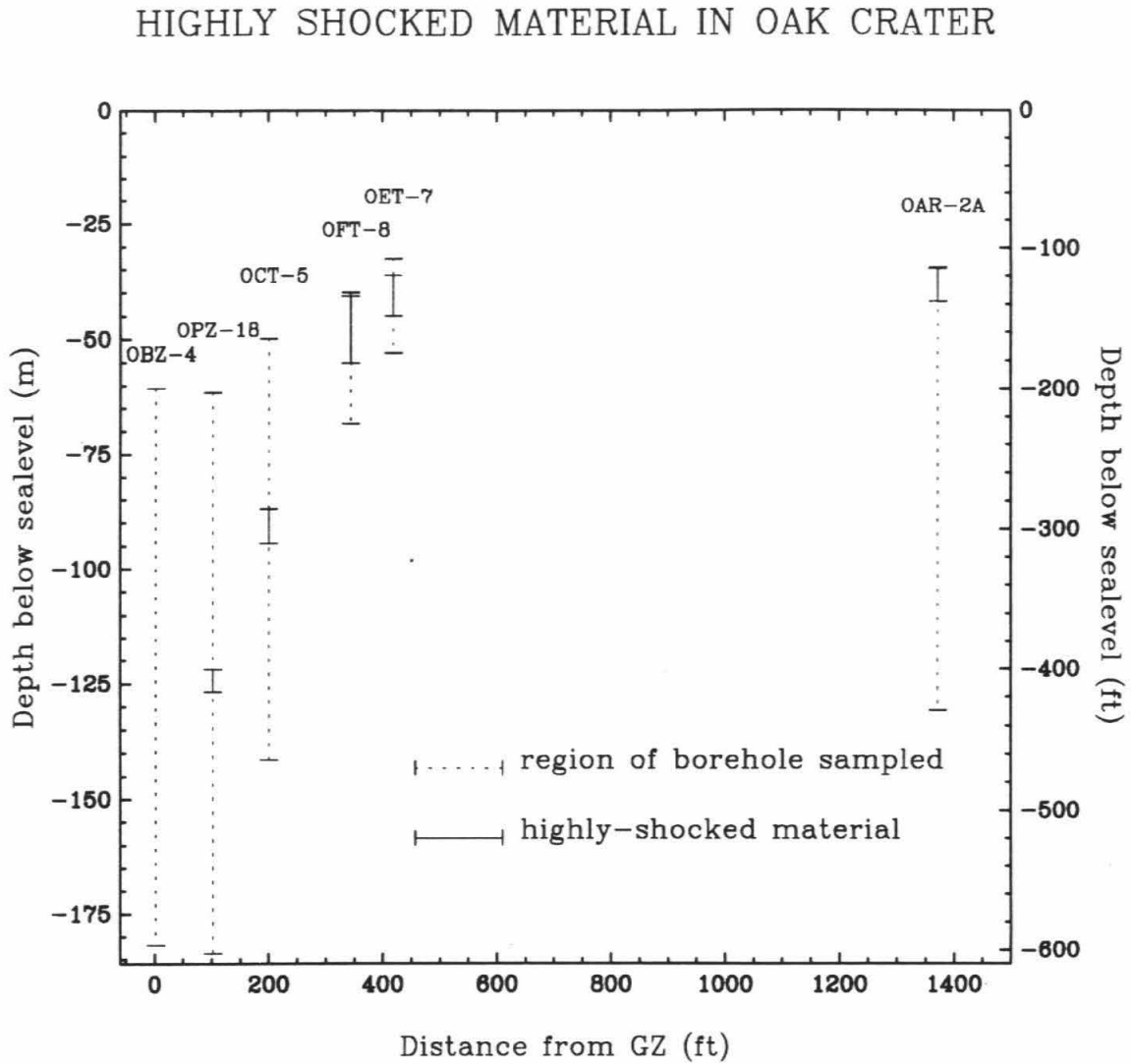


FIGURE 2.8b: Results of the core sample analysis showing the depth and thickness of each zone of highly shocked material as a function of distance from ground zero. The dotted line indicates the distance from the current sea floor to the top of the zone, whereas the solid line indicates the region containing highly shocked material.

of the excavational crater (Henry, *et al.*, 1986). The majority of the samples were from the GAMMA zone; however, all but the uppermost sample were heavily to moderately shocked. Of the highly shocked samples, 6 out of 7 were uncemented sediment samples. The highly shocked zone extended from 36.2 to 45.0 m bsl.

Borehole OAR-2A was initially sampled only as a reference core; however, 6 surface samples appear to have been heavily shocked. All of the shocked samples were located within the top 12 m of the core, 33.9 to 45.4 m bsl, with the most heavily shocked material within the first 7 m. The proximity of this borehole to the reef suggests that highly shocked, fine-grain ejecta may have been deposited from the slope at later times. The combined results from the OAK borehole sample analysis are presented in Figure 2.8a. The solid horizontal line in each panel indicates the present sea floor depth. The depth and thickness of each zone containing highly shocked material ($P = 10$ GPa) as a function of the distance of the borehole from ground zero are shown in a simplified manner in Figure 2.8b.

2.6.3 Results of the ejecta sample analysis

The ejecta in this study consist of 14 samples collected by a submersible from various sites throughout the crater and 3 samples collected by scuba divers from roughly a single site. The former samples are a subset of a series of ejecta samples analyzed by Halley *et al.*(1986). Figure 2.9 shows the locations from where each ejecta sample was recovered. The range values that will be discussed later were measured from this map. Unfortunately, the ejecta samples in this study were all taken from roughly the same distance from ground zero. There was only one sample, OAK 201, which was recovered at a significantly different range. The results of the ejecta analysis are plotted in Figure 2.10a. The majority of the ejecta samples were

OAK CRATER DEBRIS SAMPLES

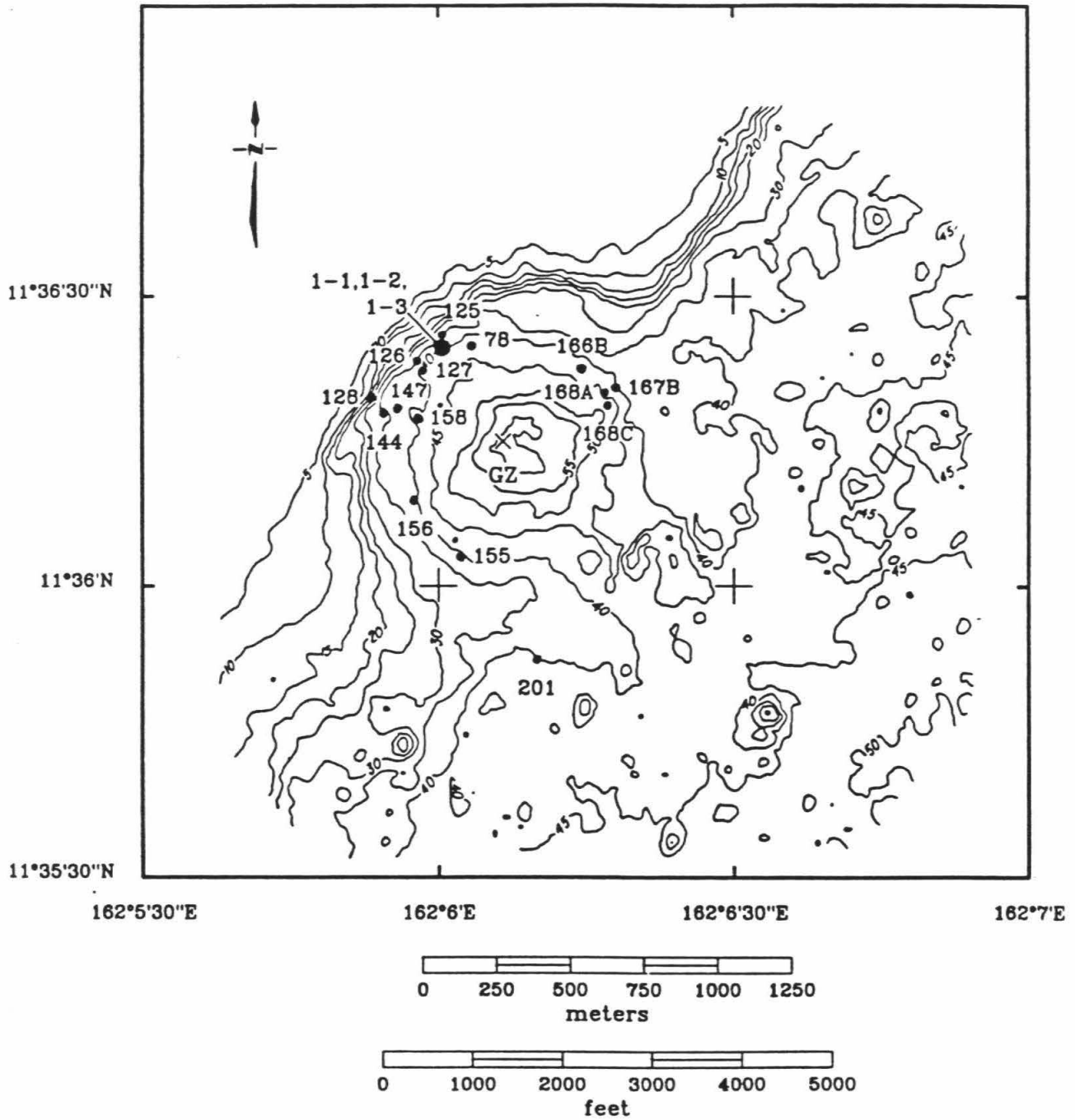


FIGURE 2.9 : Map of OAK crater showing ejecta recovery sites.

relatively unshocked; however, all of the highly shocked ejecta were found at the base of the reef slope. The reef may have blocked some highly shocked ejecta from leaving the crater, or the ejecta could have been transported down the reef slope some time after the crater was formed.

In addition to the range measurements, the estimated pre-explosion initial depth of a limited number of the ejecta samples was available from strontium isotopic analyses (Halley, *et al.*, 1986) and paleontology (Ristvet, 1981). The pre-explosion depth below seafloor is plotted against shock pressure for these samples in Figure 2.10 b. Although the pre-explosion depth estimates are crude in some cases, there is a strong correlation between shock pressure and depth for this limited data set. This is consistent, however, with the previous assertion that the surface material was the most severely shocked.

2.6.4 Interpretation of OAK Crater

With a few exceptions, the bulk of the samples analyzed can be split into two categories, unshocked and very heavily shocked. There were relatively few samples that are assigned to intermediate pressures. The lack of samples at intermediate shock pressures suggests that the majority of the shocked material shares a common origin. This material may represent a thin fallout layer such as that described by Roddy (1977) for SNOWBALL Crater. Presumably, the material right at or near the surface received the highest shock pressure from the blast. During the cratering event, this material became the lining of the transient crater cavity and was then buried almost immediately by the collapse of the cavity. Subsequent slumping and deformation of the crater would tend to mix this material with other rubble and breccia and consequently obscure the zone as an identifiable stratigraphic unit. This

OAK DEBRIS

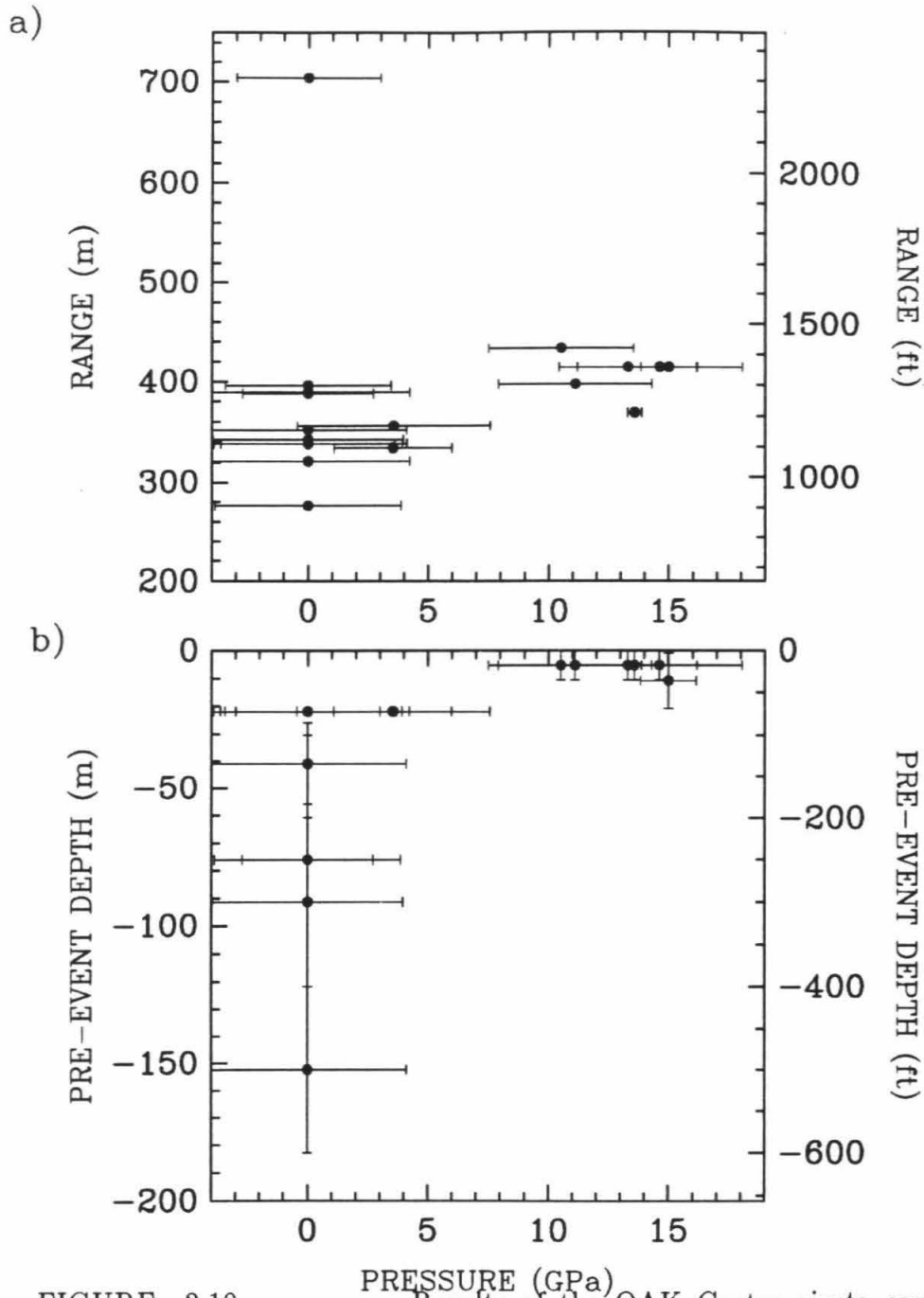


FIGURE 2.10 : Results of the OAK Crater ejecta sample analysis showing a) shock pressure as a function of range from ground zero, and b) estimated pre-explosion depth below seafloor versus shock pressure for a subset of the ejecta samples.

hypothesis can be applied to the presence of the shocked regions in OPZ-18 and the transition boreholes. Because slumping and collapse become increasingly more important towards the rim of the crater, it is not unreasonable that OPZ-18 is the only borehole to have the shocked material preserved in a unit such as the transition sands. The thickness of the region of highly shocked material does remain fairly constant throughout the three transition boreholes (Figure 2.8b), although the region is located at consistently shallower depths as the distance between the borehole and ground zero increases. This is a further indication that these regions were at one time related.

Late-stage debris slumping and the influence of sedimentation have also contributed to borehole stratigraphy. Post-event slumps from the reef have deposited at least 2.5 m of unshocked debris at OET-7, and possibly as much as 5 m at OFT-8. The location of the shocked ejecta samples collected from the floor of the crater suggest that highly shocked ejecta may also be deposited from the reef slope, and the shocked upper layer of OAR-2A could be the result of accumulated deposition over many years.

2.7 Meteor Crater

Meteor Crater is 180 m deep and 1.2 km in diameter. It is located in north-central Arizona in part of the Colorado Plateau. The crater was formed in flat-lying bedrock consisting of the Moenkopi, Kaibab, Coconino, and Toroweap Formations (Shoemaker and Kieffer, 1974). Thermoluminescence studies of the Coconino sandstone and the Kaibab dolomite give an age of 49,000 years for the crater (Sutton, 1985).

Unlike the previous discussion of OAK Crater, the analysis of the Meteor Crater

samples will be more qualitative than quantitative. The Kaibab data set is divided into five sections: pressure calibration experiments (discussed above), Diablo Canyon unshocked Kaibab standards, samples from the walls of Meteor Crater, Meteor Crater ejecta samples, and a miscellaneous category including breccia samples and highly shocked Kaibab ejecta subsequently redeposited inside the crater. A complete catalogue of these spectra is included in Appendix B.

Although the effects of shock pressure on Kaibab have been demonstrated in Figure 2.3b, shock pressure may not be the only variable. As mentioned previously, the Mn^{2+} may substitute in both the Mg and Ca sites of the dolomite structure. The distribution of Mn^{2+} between these sites will affect the shape of the resulting spectrum. Therefore, differences in the Mn^{2+} distribution between the various members of the Kaibab formation could confuse the effects of shock pressure. The spectra from a series of Kaibab samples taken from Diablo Canyon (10 miles east of Meteor Crater) are presented in Appendix B. Although the calibration Equations 3a and 3b were defined using the high-resolution spectra constructed from an average of the Diablo Canyon samples, the calibration was still applied to these samples as a test. The results are listed in Table B.1 and show that in most cases the expected zero pressure was obtained. The pressure of 0.1 GPa calculated for sample 2 illustrates the limitations in accuracy of this analysis. A sample of caliche was also processed in order to determine whether or not weathering products would influence the analysis. However, the caliche spectrum found following Table B.4 is clearly distinguishable from the Kaibab spectra.

2.7.1 Results of the Meteor Crater sample analysis

The results for the crater wall analysis are listed in Table B.2. There is a slight

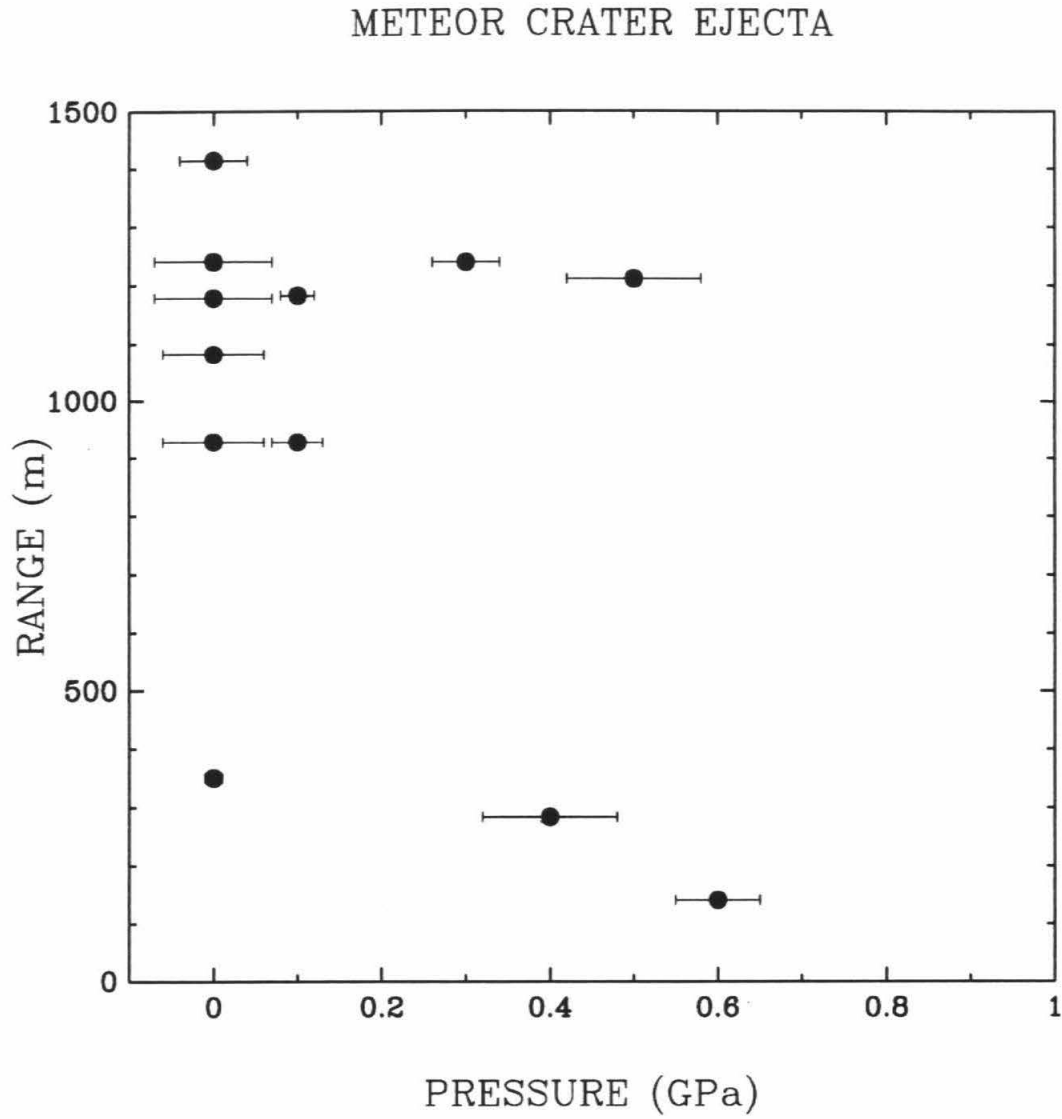


FIGURE 2.11 : Results of the Meteor Crater ejecta sample analysis showing shock pressure as a function of range from the crater rim.

indication of shock damage, 0.6 GPa, in the samples from the β member of the Kaibab formation. As an exercise, the value of 0.6 GPa was used to calculate a yield for the Meteor Crater impact event based on the results shown in Figure 1 of Moss (1988) for underground nuclear explosion craters. The plot from Moss (1988) is reproduced here in Figure 2.12. The plot includes two theoretical model curves as well as experimental data from underground nuclear explosions. Using the Moss's model curve gives a yield of 17 Mton, whereas the data included in the figure predict a yield of 72 Mton. The former value is within the range predicted by Roddy *et al.*(1980) from computer code simulations. However, caution must be used when interpreting these results because of the limited data in the present calibration equations.

There was also some evidence of light shock damage in the ejecta samples. Figure 2.11 shows a plot of shock pressure versus distance from the crater rim for the Meteor Crater ejecta. The results are also listed in Table B.3. As in the case of OAK Crater ejecta, the majority of the samples appear to be unshocked. However, there was some bias in the ejecta sampling technique. All the ejecta samples were taken from large boulders within the ejecta field. The results could change if more samples were taken over a complete distribution in ejecta size. No sign of the Mn^{2+} spectrum was found for ejecta samples which had been partially melted as a result of the impact (Table B.4).

2.8 Summary

The comparison of EPR spectra has been shown to be a useful technique in the analysis of both explosion and impact craters in carbonate rocks. In OAK Crater we were able to detect the highly shocked fallout layer underneath the crater in areas

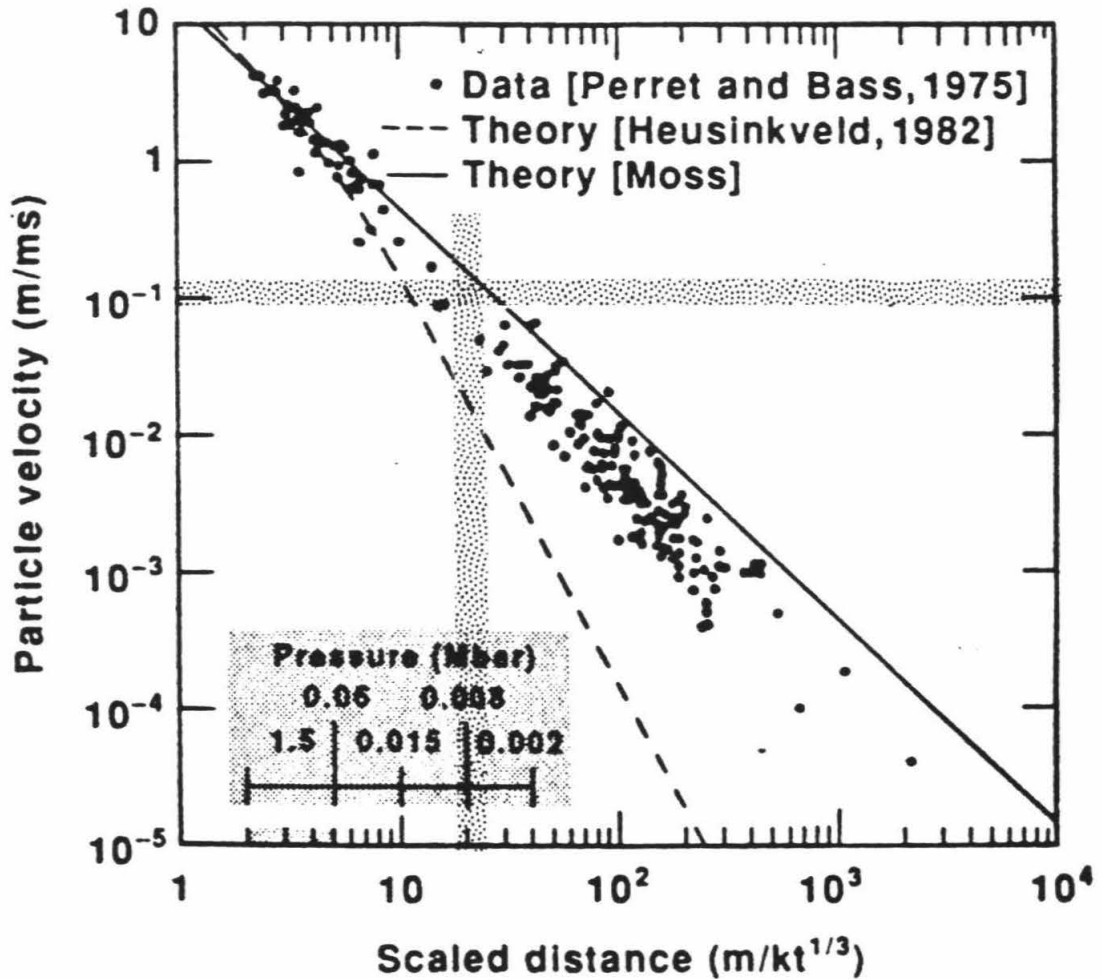


FIGURE 2.12 : Particle velocity at the shock front, as a function of the position of the shock front as taken from Moss (1988). The shaded horizontal band represents the range of particle velocities experienced by the walls of Meteor Crater as predicted from the EPR analysis.

where the unit had not been previously mapped. The Meteor Crater analysis suggests low levels of shock damage preserved in the crater walls. Although the sampling of Meteor Crater was less complete, the results of the combined analyses suggest that this technique could be applied to Meteor Crater in a more comprehensive study in the future.

Acknowledgements

The authors would like to thank Lt. Col. Robert Couch, Jr., for his general technical advice and support of the Enewetak project. We also thank Thomas W. Henry for his assistance with OAK borehole sample acquisitions; Robert Halley and Byron Ristvet for providing OAK ejecta samples; Gene Shoemaker and Dave Roddy for assistance in collecting samples from Meteor Crater; Ralph Hopkins for the Kaibab samples from Diablo Canyon; Papo Gelle, Mike Long, and Leon Young for preparing the recovery samples for the shock-wave experiments, and Sunney Chan for use of the EPR facilities.

2.9 References

- Ahrens, T. J. and V. G. Gregson (1964). Shock compression of crustal rocks: Data for quartz, calcite, and plagioclase rocks. *J. Geophys. Res.* 69, 4839-4874.
- Blanchard, S. C. and N. D. Chasteen (1976). Electron paramagnetic resonance spectrum of a sea shell. *Mytilus edulis*. *J. Phys. Chem.* 80, 1362-1367.
- Dunham, R. J. (1962). Classification of carbonate rocks according to depositional texture In *Classification of Carbonate Rocks, A Symposium*; (W. E. Ham, Ed.), pp. 1-8-121. American Association of Petroleum Geologists Memoir 1.
- Folger, D. W. (1986). *Sea-Floor Observations and Subbottom Seismic Characteristics of OAK and KOA Craters, Enewetak Atoll, Marshall Islands*: U.S. Geological Survey Bulletin 1678. 301 pp.
- Grady, D. E., W. J. Murri, and K. D. Mahrer (1976). Shock compression of dolomite. *J. Geophys. Res.* 81, 889-893.
- Grieve, R.A.F. (1982). The record of impact on Earth: Implications for a major Cretaceous/Tertiary impact event In *Geological Implications of Impacts of Large Asteroids and Comets on the earth* (L.T. Silver and P.H. Schultz, Eds.), pp. 25-68. Geological Society of America Special Paper 190.
- Grolier, M.J. (1985). *Bibliography of Terrestrial Impact Structures* NASA Technical Memorandum 87567. 548 pp.
- Halley, R. B.; R. P. Major; K. R. Ludwig; Z. L. Peterman; and R. K. Matthews (1986). Preliminary analyses of OAK debris samples; In *Sea-floor observations and subbottom seismic characteristics of OAK and KOA craters, Enewetak Atoll,*

Marshall Islands: U.S. Geological Survey Bulletin 1678. (Folger, D.W., Ed.), pp. G1-G11.

Henry, T. W.; B. R. Wardlaw; B. Skipp; R. P. Major; and J. I. Tracey, Jr. (1986). In *Pacific Enewetak Atoll Crater Exploration (PEACE) Program Enewetak Atoll, Republic of the Marshall Islands; Part 1: Drilling operations and descriptions of boreholes in vicinity of KOA and OAK craters*: U.S. Geological Survey Open-File Report 86-419.

Hurd, F. K.; M. Sachs; and W.D. Hershberger (1954). Paramagnetic resonance absorption of Mn^{++} in single crystals of $CaCO_3$. *Phys. Rev.* **93**, 373-380.

Isbell, W. M.; F. H. Shipman; and A. H. Jones (1966). *Hugoniot equation of state measurements for selected geological materials*. Quarterly Progress Report No. 2, NAS 2-3427. 8 pp.

Knowles, C. P. and H. L. Brode (1977). The theory of cratering phenomena, an overview. In *Impact and Explosion Cratering* (D. J. Roddy, R. O. Pepin, and R. B. Merrill, Eds.), pp. 869-895. Pergamon, Elmsford, N. Y.

Low, W. and S. Zeira (1972). ESR spectra of Mn^{++} in heat-treated aragonite *Am. Mineral.* **57**, 1115-1124.

Ludwig, K. R.; R. B. Halley; K. R. Simmons; and Z. E. Peterman (1986). Sr-isotope stratigraphy of disturbed and undisturbed carbonates In *Pacific Enewetak Atoll Crater Exploration (PEACE) Program Enewetak Atoll, Republic of the Marshall Islands; Part 3: Stratigraphic analysis and other geologic and geophysical studies in vicinity of OAK and KOA craters*: U.S. Geological Survey Open-File Report 86-555.

- Mankowitz, J. and W. Low (1970). Forbidden transitions ($\Delta m = \pm 1$) in the paramagnetic resonance absorption of Mn^{2+} in calcite. *Phys. Rev. B.* **2**, 28-32.
- Marsh, S. P. (Ed.) (1980). *LASL Shock Hugoniot Data* University of California Press, Berkeley. 658 pp.
- Moss, W. C. (1988). A method to estimate the yield of an underground nuclear explosion. *J. Appl. Phys.* **63**, 4771-4773.
- O'Keefe, J.D. and T. J. Ahrens (1982). Cometary and meteorite swarm impact on planetary surfaces. *J. Geophys. Res.* **87**, 6668-6680.
- Polanskey, C. A. and T. J. Ahrens (1987a). Electron paramagnetic resonance studies of selected borehole samples and debris material from OAK crater In *Pacific Enewetak Atoll Crater Exploration (PEACE) Program Enewetak Atoll, Republic of the Marshall Islands; Part 4: Analysis of borehole gravity survey and other geologic and bathymetric studies: U.S. Geological Survey Open-File Report 87-665.*
- Polanskey, C.A. and T. J. Ahrens (1987b). Shocked calcite from an explosion crater. (abstract). In *Lunar Planet. Sci. XVIII*, p. 794-795. Lunar and Planetary Institute, Houston.
- Prissok, F. and G. Lehmann (1986). An EPR study of Mn^{2+} and Fe^{3+} in dolomites. *Phys. Chem. Minerals* **13**, 331-336.
- Ristvet, B., 1981, Personal communication.
- Roddy, D. J. (1977). Large-scale impact and explosion craters: Comparisons of morphological and structural analogs. In *Impact and Explosion Cratering* (D. J. Roddy, R. O. Pepin, and R. B. Merrill, Eds.), pp. 185-246. Pergamon,

Elmsford, N. Y.

Roddy, D. J. and R. O. Pepin (1977). *Impact and Explosion Cratering* Pergamon Press, New York. 1301 pp.

Roddy, D. R.; S. H. Schuster; K. N. Kreyenhagen; and D. L. Orphal (1980). Computer code simulations of the formation of Meteor Crater, Arizona: Calculations MC-1 and MC-2. *Proc. Lunar Planet. Sci. Conf. 11th*, 2275-2308.

Shoemaker, E. M. and S. Kieffer (1974) Synopsis of the geology of Meteor Crater. In *Guidebook to the Geology of Meteor Crater*, Ann. Mtg. Meteoritical Society, Aug. 1974.

Short, N.M. and T. E. Bunch (1968). A worldwide inventory of features characteristic of rocks associated with presumed meteorite impact structures. In *Shock Metamorphism of Natural Materials* (B.M. French and N.M. Short, Eds.), pp. 255-266. Mono Book Corp, Baltimore.

Stoffler, D. (1972). Deformation and transformation of rock-forming minerals by natural and experimental shock processes. *Fortschr. Mineral.* 49, 50-113.

Sutton, S. R. (1985). Thermoluminescence measurements on shock-metamorphosed sandstone and dolomite from Meteor Crater, Arizona 2. Thermoluminescence age of Meteor Crater. *J. Geophys. Res.* 90, 3690-3700.

Tyburczy, J. A. and T. J. Ahrens (1986). Dynamic compression and volatile release of carbonates. *J. Geophys. Res.* 91, 4730-4744.

Vinokurov, V. M.; M. M. Zaripov; and V. G. Stepanov (1961). A study of some Mn-containing carbonates by the method of electron paramagnetic resonance. *Sov. Phys. Crystallogr.* 6, 83-86.

- Vizgirda, J.; T. J. Ahrens; and F. Tsay (1980). Shock-induced effects in calcite from Cactus Crater. *Geochim. Cosmochim. Acta.* 44, 1059-1069.
- Wardlaw, B. R. and T. W. Henry (1986). Geologic interpretation of OAK and KOA craters In *Pacific Enewetak Atoll Crater Exploration (PEACE) Program Enewetak Atoll, Republic of the Marshall Islands; Part 3: Stratigraphic analysis and other geologic and geophysical studies in vicinity of OAK and KOA craters*: U.S. Geological Survey Open-File Report 86-555.
- Wildeman, T. R. (1970). The distribution of Mn^{2+} in some carbonates by electron paramagnetic resonance. *Chem. Geol.* 5, 167-177.

Appendix A

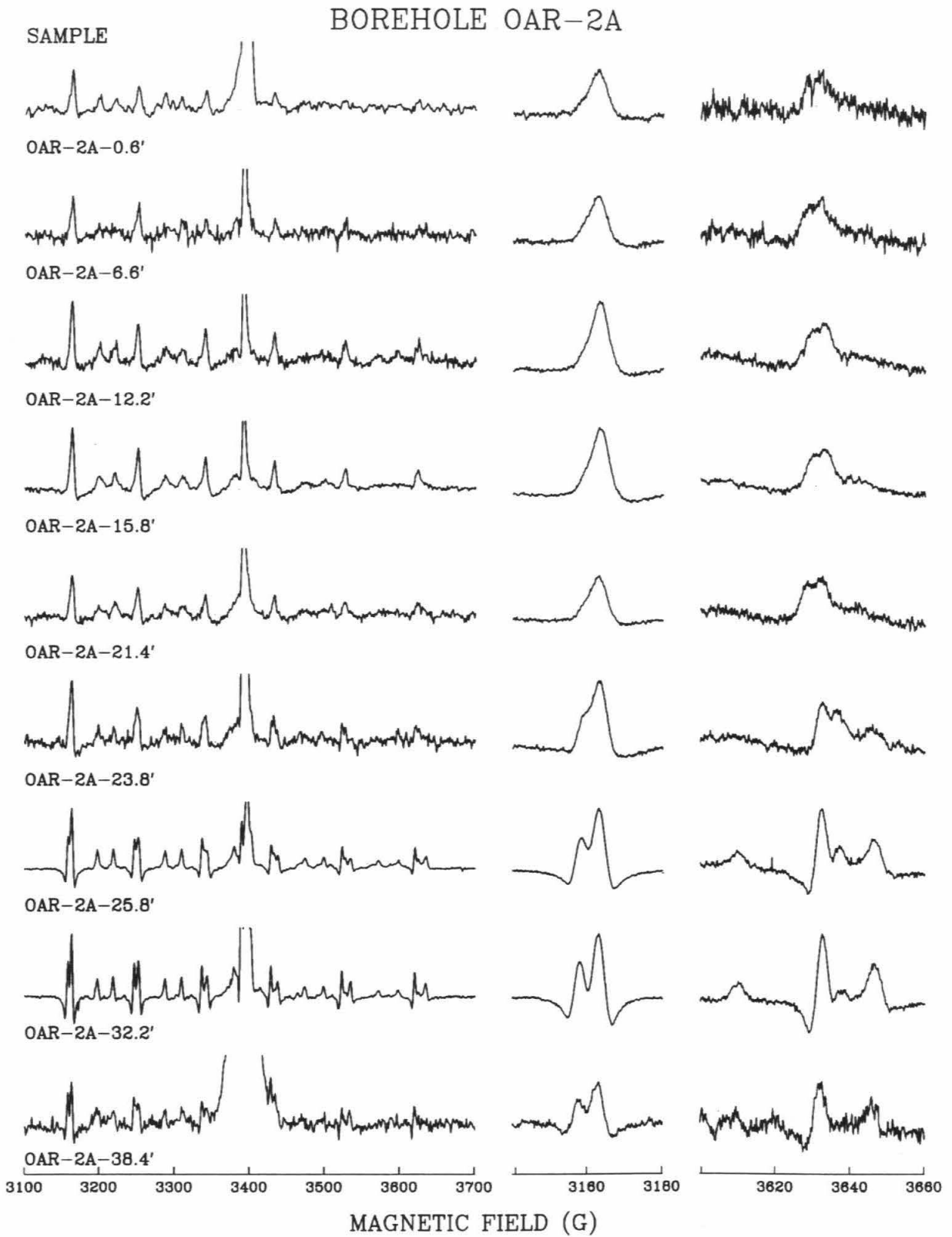
OAK Sample Descriptions, Results and Spectra

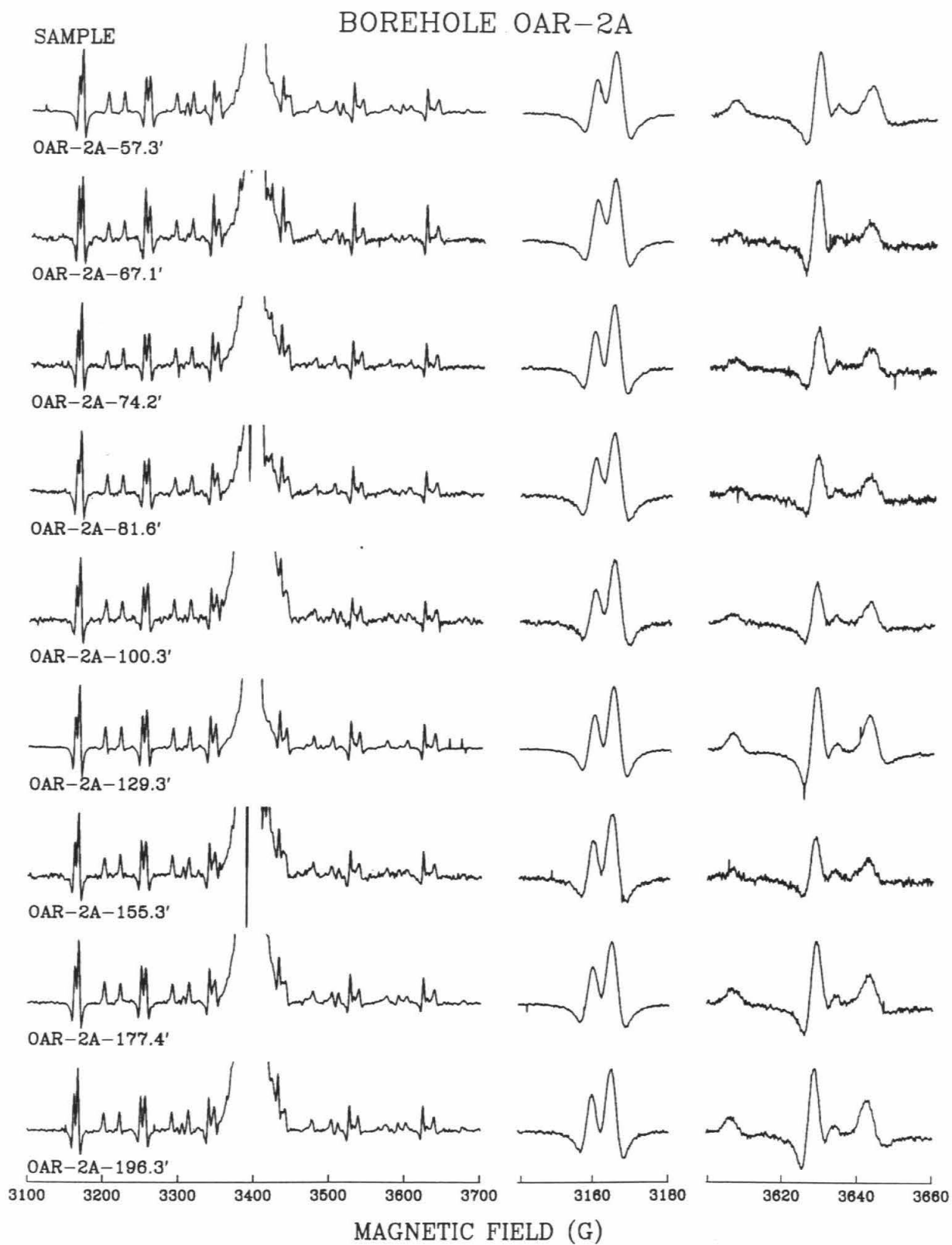
TABLE A.1

Results for Borehole OAR-2A Samples

The pressures and accompanying errors are given in Giga Pascal (GPa). Depths are provided in three sets of units: feet below sea floor (ft bsf), feet below sea level (ft bsl), and meters below sea level (m bsl). For explanation of carbonate petrographic names used under Description column in this and succeeding tables, see Henry *et al.* (1986, pp. 83-97).

Depth			P		Description
(ft bsf)	(ft bsl)	(m bsl)	(GPa)	± (GPa)	
0.6	111.1	33.9	12.4	2.6	uncemented sand
6.6	117.1	35.7	12.9	2.1	uncemented wackestone
12.2	122.7	37.4	12.6	1.4	uncemented wackestone
15.8	126.3	38.5	13.2	0.9	uncemented wackestone
21.4	131.9	40.2	12.8	1.8	uncemented packstone
23.8	134.3	40.9	10.2	1.0	uncemented wackestone/packstone
25.8	136.3	41.5	3.4	0.6	uncemented packstone
32.2	142.7	43.5	0.0	1.0	cemented packstone
38.4	148.9	45.4	4.3	3.0	poorly cemented packstone
57.3	167.8	51.1	0.0	0.7	cemented packstone
67.1	177.6	54.2	0.0	0.9	poorly cemented wackestone
74.2	184.7	56.3	0.0	1.0	uncemented wackestone
81.6	192.1	58.6	0.0	1.5	uncemented wackestone
100.3	210.8	64.2	0.0	1.6	coral fragment, <i>Astreopora</i>
129.3	239.8	73.1	0.0	0.6	cemented wackestone
155.3	265.8	81.0	0.0	1.4	spar-replaced coral
177.4	287.9	87.8	0.0	0.7	well-cemented mudstone
196.3	306.8	93.5	0.0	0.8	cemented wackestone
241.6	352.1	107.3	0.0	1.2	uncemented grainstone
280.0	390.5	119.0	0.0	0.9	cemented wackestone burrow
315.3	425.8	129.8	0.0	1.1	cemented wackestone





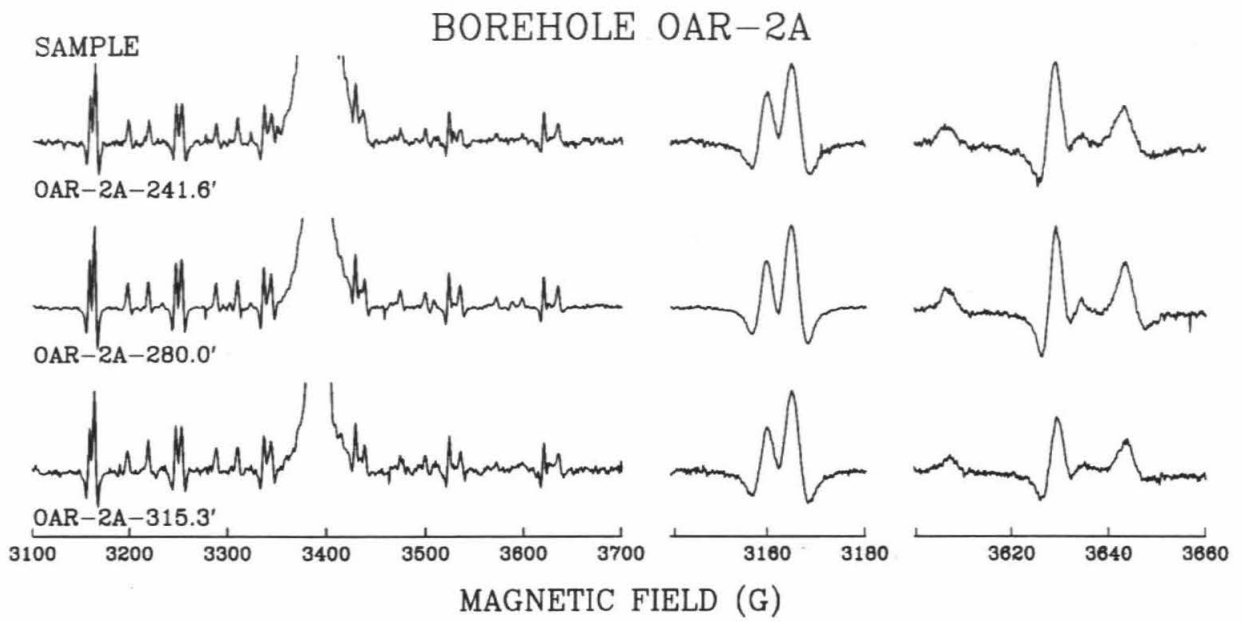


TABLE A.2

Results for Borehole OBZ-4 Samples

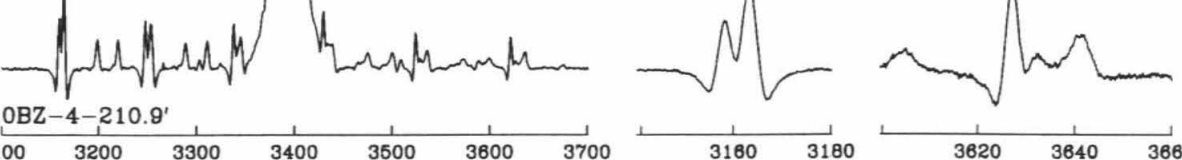
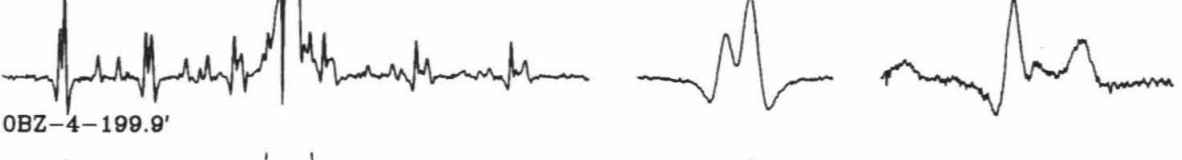
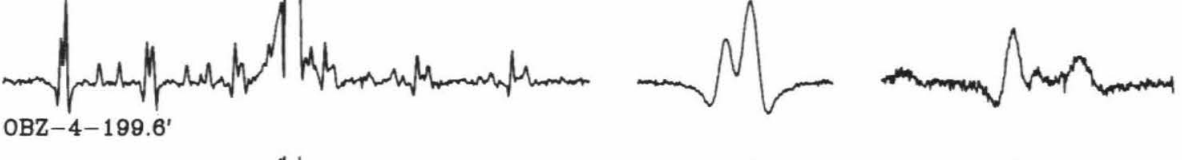
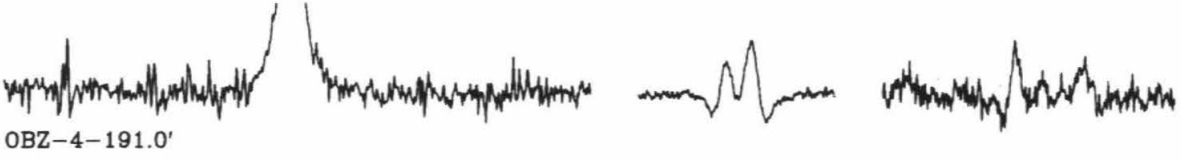
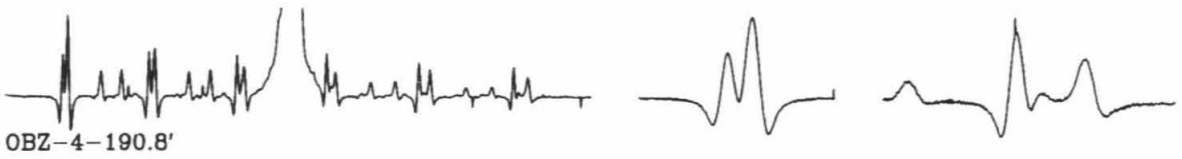
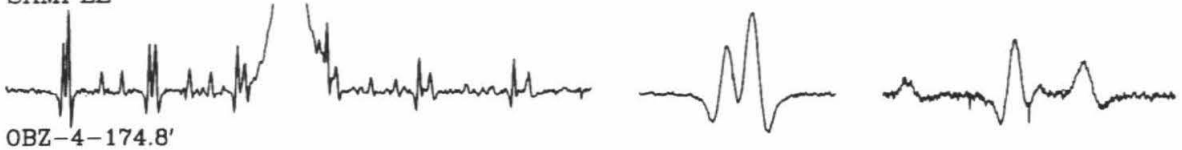
The pressures and accompanying errors are given in Giga Pascal (GPa). Depths are provided in three sets of units: feet below sea floor (ft bsf), feet below sea level (ft bsl), and meters below sea level (m bsl).

Zone	Depth			P \pm		Description
	(ft bsf)	(ft bsl)	(m bsl)	(GPa)	(GPa)	
α_1	6.7	205.4	62.6	0.0	0.9	mud
α_2	44.0	242.7	74.0	0.0	1.0	wackestone
β_{1a}	75.9	274.6	83.7	0.0	1.5	coarse-grain packstone
	107.5	306.2	93.3	0.0	1.0	cemented packstone
β_{1b}	119.1	317.8	96.9	0.0	1.0	cemented packstone
	136.0	334.7	102.0	0.0	0.6	cemented packstone
	141.8	340.5	103.8	0.0	0.5	cemented packstone
	152.1	350.8	106.9	0.0	1.4	cemented packstone
	163.3	362.0	110.3	0.0	0.8	cemented packstone
	174.8	373.5	113.8	0.0	0.9	spar
	190.8	389.5	118.7	0.0	0.7	cemented wackestone burrow
	191.0	389.7	118.8	2.3	2.6	lithoclast and spar
	193.2	391.9	119.4	0.0	0.6	cemented packstone
	196.1	394.8	120.3	0.0	3.1	spar-replaced <i>Favia</i>
	199.6	398.3	121.4	0.0	1.3	fine-grain muddy sand
β_2	199.9	398.6	121.5	0.0	0.7	uncemented wackestone
	207.7	406.4	123.9	0.0	1.4	cemented wackestone burrow
	210.9	409.6	124.8	0.0	0.7	cemented packstone burrow
β_3	216.6	415.3	126.6	0.0	0.7	recrystallized <i>Tridacna</i>
	217.1	415.8	126.7	0.0	1.2	well-cemented tea-brown micrite
	219.4	418.1	127.4	0.0	1.1	spar-replaced coral
	222.7	421.4	128.4	0.0	0.7	cemented packstone
	233.0	431.7	131.6	0.0	0.7	uncemented packstone
	265.1	463.8	141.4	0.0	1.2	poorly cemented packstone
γ	324.0	522.7	159.3	0.0	1.1	cemented burrow
	397.7	596.4	181.8	0.0	3.2	spar-replaced coral



BOREHOLE OBZ-4

SAMPLE



3100 3200 3300 3400 3500 3600 3700 3160 3180 3620 3640 3660
MAGNETIC FIELD (G)

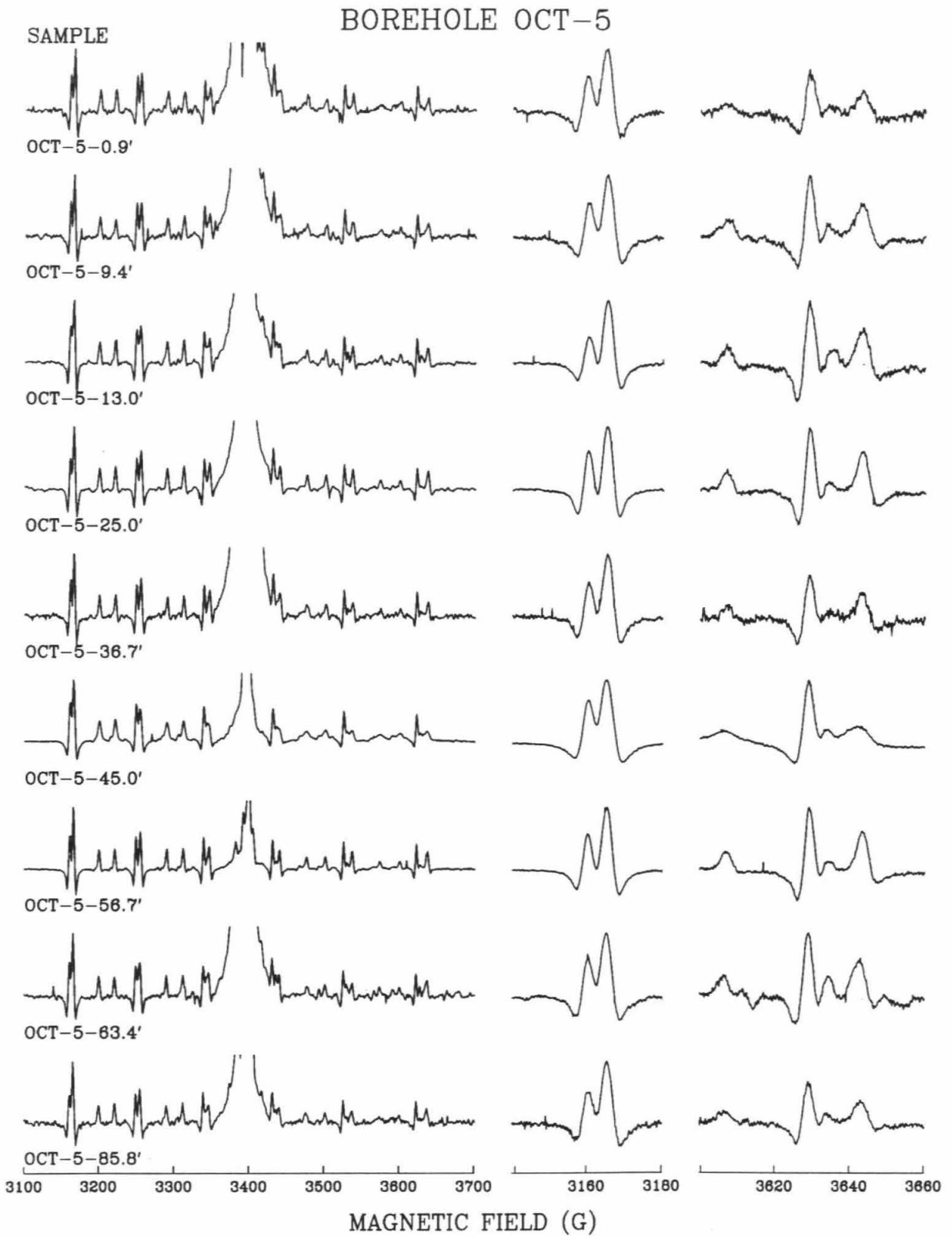


TABLE A.3

Results for Borehole OCT-5 Samples

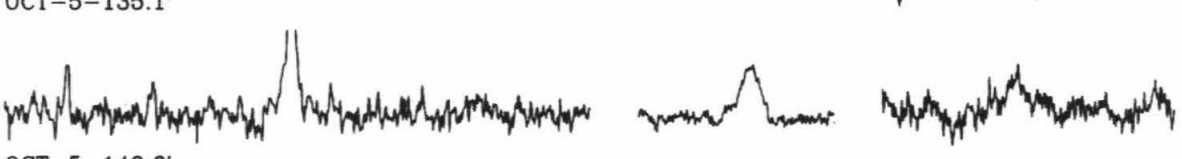
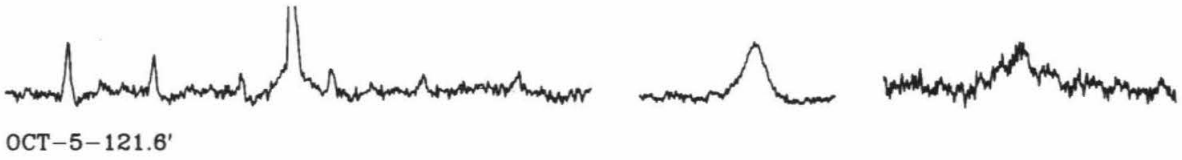
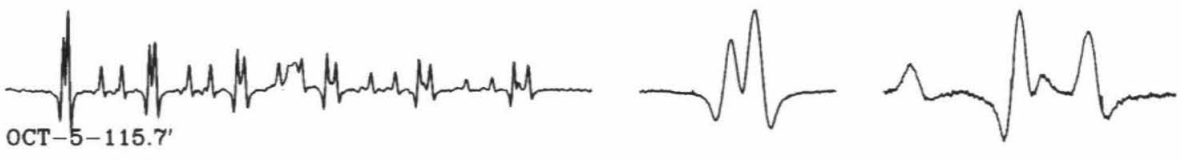
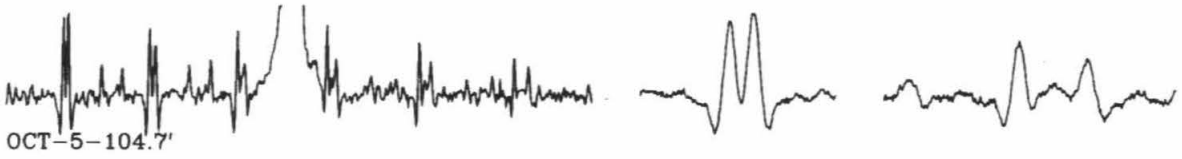
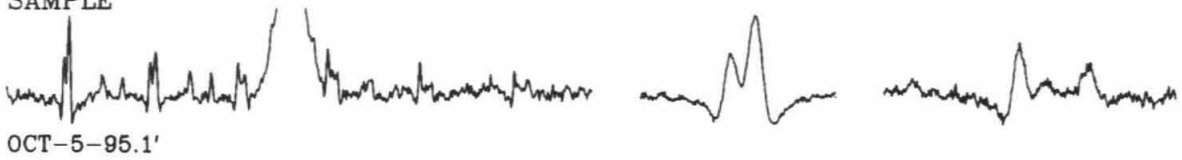
The pressures and accompanying errors are given in Giga Pascal (GPa). Depths are provided in three sets of units: feet below sea floor (ft bsf), feet below sea level (ft bsl), and meters below sea level (m bsl).

Zone	Depth			P (GPa)	\pm (GPa)	Description
	(ft bsf)	(ft bsl)	(m bsl)			
α_1	0.9	164.6	50.2	0.0	1.0	uncemented grainstone
α_2	9.4	173.1	52.8	0.0	1.1	coarse-grain packstone
β_{1a}	13.0	176.7	53.8	0.0	1.0	uncemented packstone
	25.0	188.7	57.5	0.0	0.9	fall-in (?)
	36.7	200.4	61.1	0.0	1.5	cemented wackestone burrow
	45.0	208.7	63.6	4.8	0.6	echinoid spine
	56.7	220.4	67.2	0.0	0.8	cemented packstone lithoclast
	63.4	227.1	69.2	0.0	2.0	rounded cemented burrow
	85.8	249.5	76.0	0.0	1.0	cemented packstone
β_{1b}	95.1	258.8	78.9	2.6	1.6	<i>Cardium</i> with internal filling
	104.7	268.4	81.8	0.0	3.5	spar-replaced <i>Cardium</i>
	115.7	279.4	85.2	0.0	0.8	cemented wackestone
	121.6	285.3	87.0	13.6	4.2	uncemented medium grainstone
	124.3	288.0	87.8	13.3	4.7	uncemented coarse grainstone
	131.9	295.6	90.1	14.8	3.6	uncemented grainstone
	135.1	298.8	91.1	15.0	8.0	cemented grainstone
	140.6	304.3	92.8	12.0	6.3	uncemented <i>Halimeda</i> packstone
	146.2	309.9	94.4	15.0	7.8	uncemented <i>Halimeda</i> packstone
	153.4	317.1	96.6	0.0	0.6	cemented burrow
	163.6	327.3	99.8	0.0	0.6	cemented packstone
	174.1	337.8	103.0	0.0	0.8	cemented packstone
γ	192.6	356.3	108.6	0.0	1.6	cemented packstone
	204.7	368.4	112.3	2.5	0.4	tea-brown cemented rhizolith
	237.0	400.7	122.1	0.0	0.8	tea-brown cemented packstone
	300.3	464.0	141.4	3.6	3.5	spar-replaced coral



BOREHOLE OCT-5

SAMPLE



3100 3200 3300 3400 3500 3600 3700 3180 3180 3620 3640 3660
MAGNETIC FIELD (G)



TABLE A.4

Results for Borehole OET-7 Samples

The pressures and accompanying errors are given in Giga Pascal (GPa). Depths are provided in three sets of units: feet below sea floor (ft bsf), feet below sea level (ft bsl), and meters below sea level (m bsl).

Zone	Depth			P (GPa)	\pm (GPa)	Description
	(ft bsf)	(ft bsl)	(m bsl)			
α_2	8.3	115.2	35.1	0.0	0.7	pebble-sized lithoclast uncemented grainstone
	12.0	118.9	36.2	13.0	4.5	
γ	17.8	124.7	38.0	15.0	5.5	coral pebble
	21.2	128.1	39.0	11.2	5.2	uncemented <i>Halimeda</i> grainstone
	25.9	132.8	40.5	15.0	4.8	uncemented packstone-grainstone
	30.7	137.6	41.9	12.6	2.7	uncemented packstone-grainstone
	35.3	142.2	43.3	13.7	4.3	uncemented packstone-grainstone
	40.6	147.5	45.0	13.0	5.0	uncemented fine-grain packstone
	66.7	173.6	52.9	6.4	2.1	cemented pebble-sized

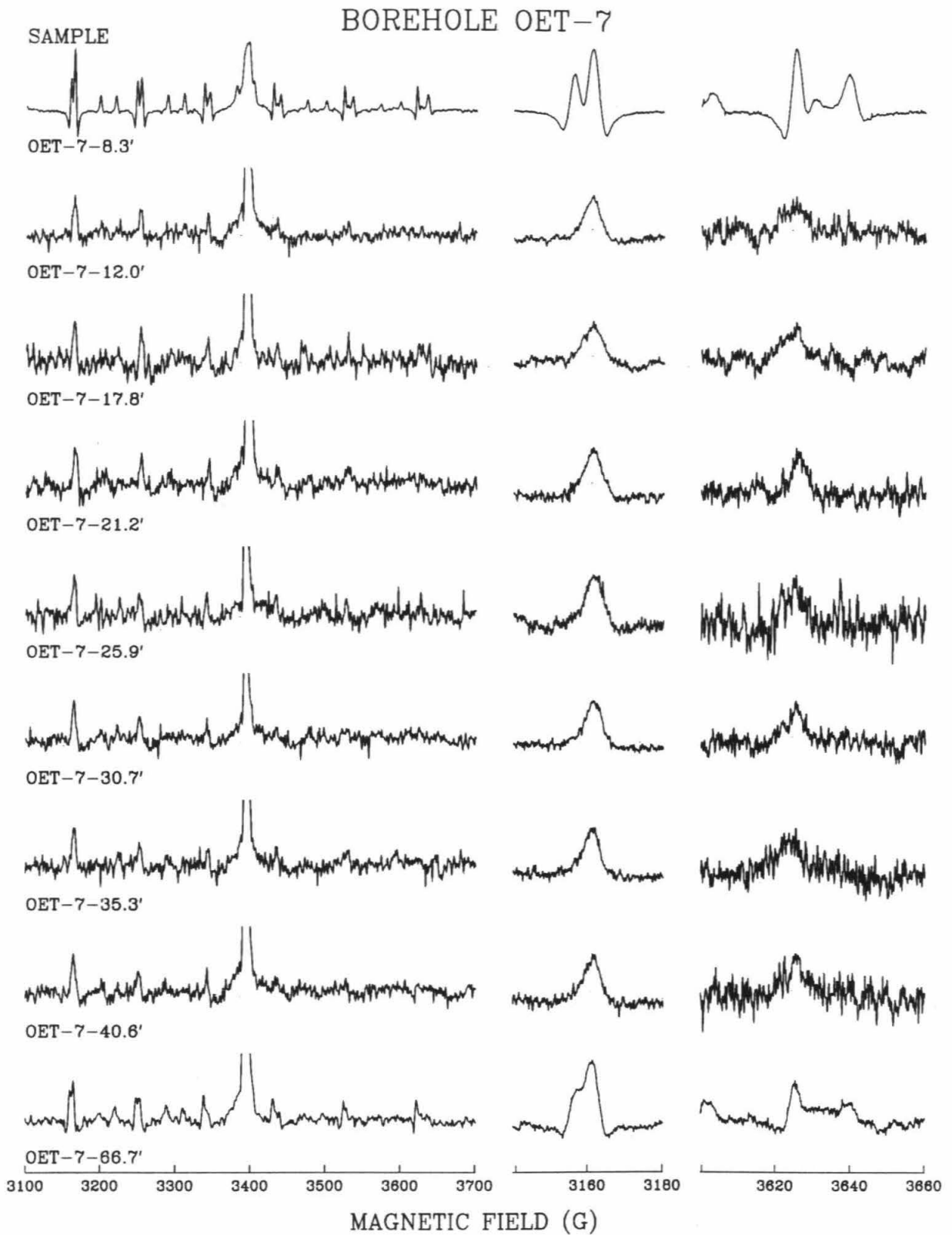


TABLE A.5

Results for Borehole OFT-8 Samples

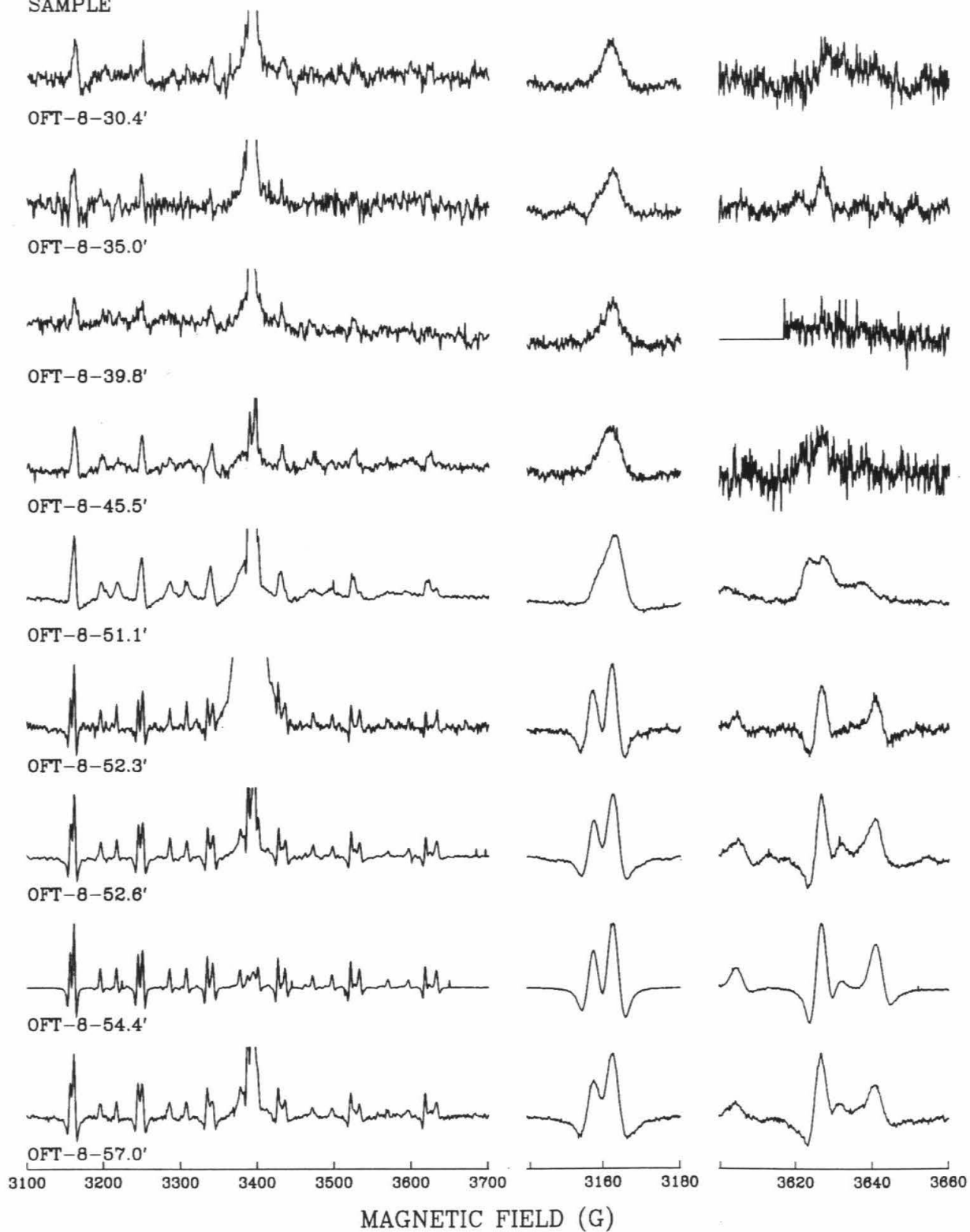
The pressures and accompanying errors are given in Giga Pascal (GPa). Depths are provided in three sets of units: feet below sea floor (ft bsf), feet below sea level (ft bsl), and meters below sea level (m bsl).

Zone	Depth			P		Description
	(ft bsf)	(ft bsl)	(m bsl)	(GPa)	± (GPa)	
α_2	2.6	133.4	40.6	13.0	7.5	
	2.7	133.5	40.7	0.0	0.6	tea-brown cemented rhizolith
	6.4	137.2	41.8	0.0	0.6	tea-brown cemented lithoclast
β_{1a}	13.1	143.9	43.9	0.0	0.6	tea-brown cemented packstone
	17.0	147.8	45.0	0.0	0.9	cemented packstone
	18.4	149.2	45.5	4.3	1.6	cemented matrix within pelecypod
	20.5	151.3	46.1	2.1	1.4	partly spar-replaced coral
β_{1b}	22.8	153.6	46.8	12.2	3.4	uncemented packstone
	26.0	156.8	47.8	14.5	3.7	uncemented grainstone
	30.4	161.2	49.1	12.2	3.9	uncemented <i>Halimeda</i>
	35.0	165.8	50.5	10.6	5.3	uncemented packstone
	39.8	170.6	52.0	13.6	3.6	uncemented packstone
	45.5	176.3	53.7	13.7	4.1	partly spar-replaced coral
	50.1	180.9	55.1	14.7	1.0	uncemented packstone
	52.3	183.1	55.8	0.0	1.2	<i>Cardium</i> with cemented matrix
	52.6	183.4	55.9	0.0	0.9	partly spar-replaced coral
	54.4	185.2	56.4	0.0	0.6	moderately cemented packstone
	57.0	187.8	57.2	2.7	0.7	moderately cemented <i>Halimeda</i>
	61.1	191.9	58.5	2.6	0.9	poorly cemented packstone
	64.5	195.3	59.5	8.1	0.8	cemented shell rubble
	64.9	195.7	59.6	0.0	1.1	spar-replaced <i>Astreopora</i>
67.0	197.8	60.3	0.0	1.0	mudstone filled cemented burrow	
γ	73.8	204.6	62.4	0.0	0.4	moderately cemented packstone
	81.2	212.0	64.6	0.0	0.5	cemented packstone
	93.5	224.3	68.4	0.0	1.4	spar-replaced <i>Porites</i>



BOREHOLE OFT-8

SAMPLE



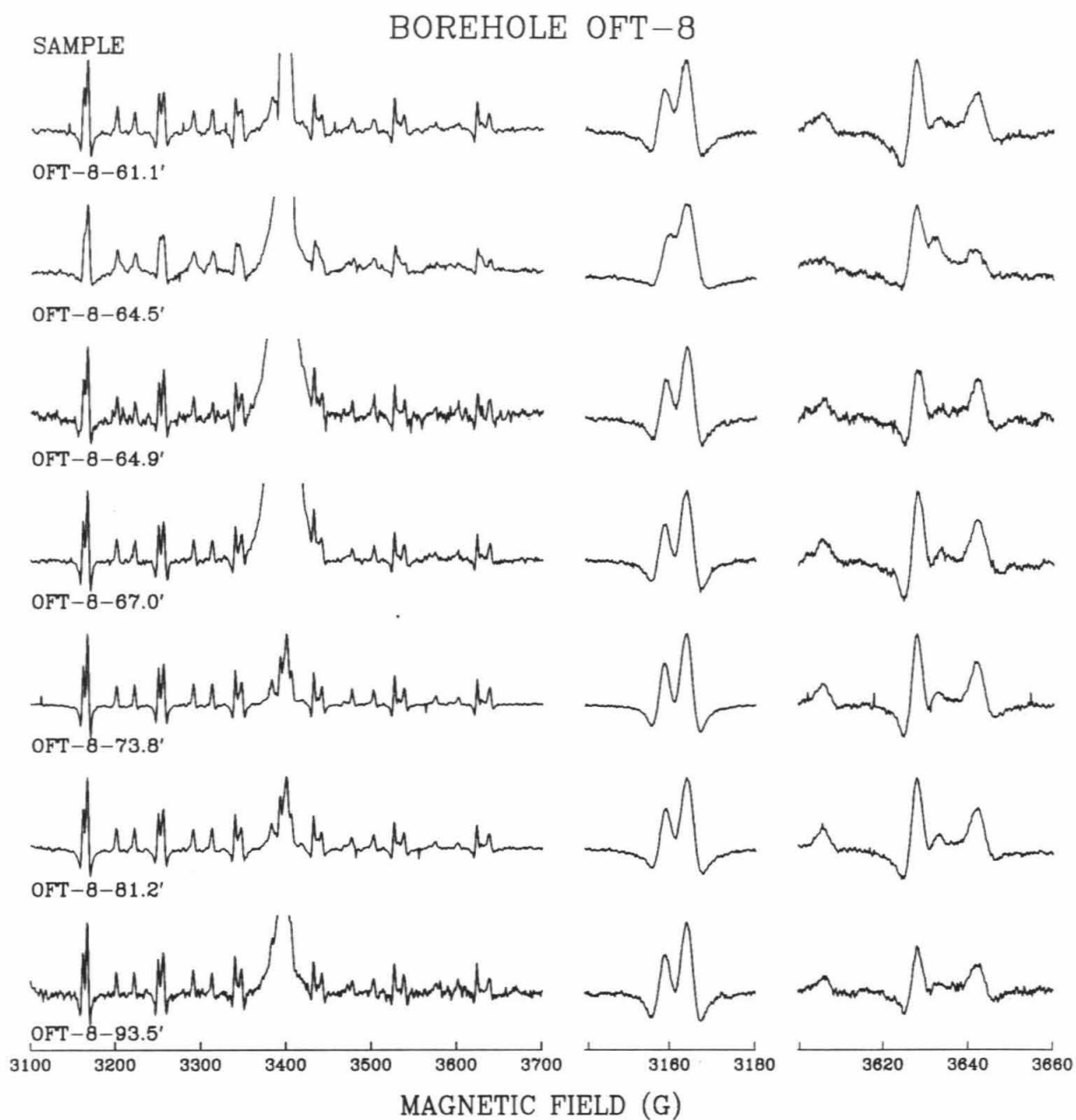
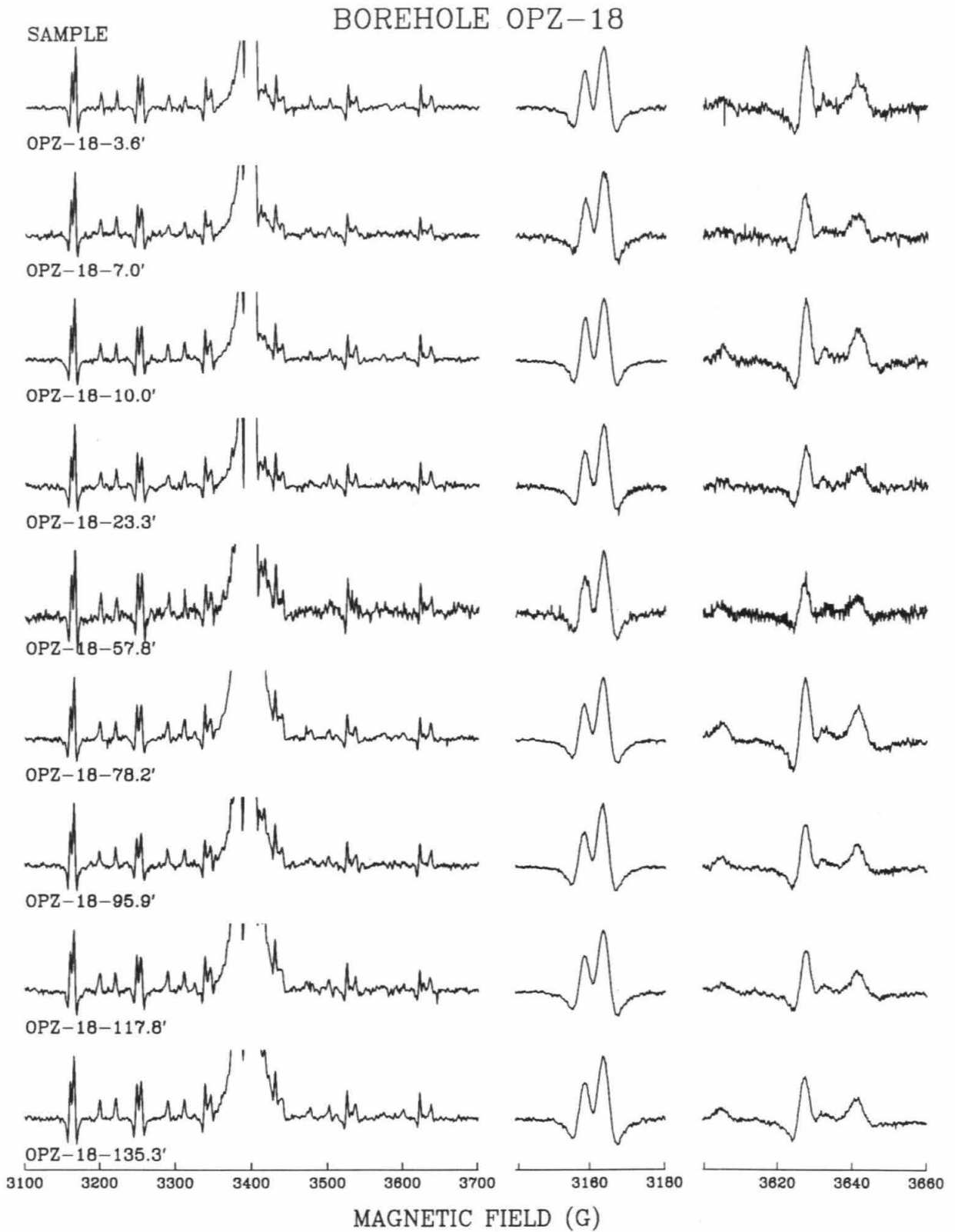


TABLE A.6

Results for Borehole OPZ-18 Samples

The pressures and accompanying errors are given in Giga Pascal (GPa). Depths are provided in three sets of units: feet below sea floor (ft bsf), feet below sea level (ft bsl), and meters below sea level (m bsl).

Zone	Depth (ft bsf)	Depth (ft bsl)	Depth (m bsl)	P (GPa)	\pm (GPa)	Description
α_1	3.6	205.5	62.6	0.0	1.4	uncemented mudstone
	7.0	208.9	63.7	2.5	2.1	uncemented mudstone
	10.0	210.9	64.3	0.0	1.0	uncemented mudstone
	23.3	225.2	68.6	0.0	1.4	uncemented mudstone
β_{1a}	57.8	259.7	79.2	0.0	2.1	uncemented wackestone
	78.2	280.1	85.4	0.0	1.4	uncemented grainstone
	95.9	297.8	90.8	0.0	1.0	uncemented grainstone
	117.8	319.7	97.4	0.0	1.1	uncemented grainstone
	135.3	337.2	102.8	0.0	0.9	uncemented grainstone
β_{1b}	155.3	357.2	108.9	2.2	0.9	uncemented packstone
	166.6	368.5	112.3	3.3	1.4	uncemented packstone
β_2	182.6	384.5	117.2	0.0	0.8	spar-cemented grainstone
	185.0	386.9	117.9	2.2	1.3	uncemented
	198.0	399.9	121.9	14.7	2.5	uncemented
	198.6	400.5	122.1	15.0	6.3	green Holocene wackestone mud
	207.0	408.9	124.6	13.6	5.4	uncemented
β_3	210.5	412.4	125.7	0.0	1.1	cemented packstone burrow
	214.0	415.9	126.8	14.1	2.5	uncemented
	217.0	418.9	127.7	0.0	0.9	tea-brown cemented packstone
	217.1	419.0	127.7	0.0	0.7	cemented wackestone
	217.5	419.4	127.8	0.0	1.4	cemented wackestone burrow
	220.4	422.3	128.7	0.0	1.3	coarse-grain spar
	220.5	422.4	128.7	0.0	0.8	cemented packstone
	223.5	425.4	129.7	0.0	1.2	cemented packstone burrow
	232.9	434.8	132.5	0.0	0.9	poorly cemented packstone
	236.3	438.2	133.6	0.0	3.5	partially spar-replaced coral
	245.4	447.3	136.3	0.0	0.6	cemented wackestone
	256.9	458.8	139.8	0.0	2.0	spar-replaced coral
	273.8	475.7	145.0	0.0	0.7	spar-cemented packstone burrow
320.5	522.4	159.2	0.0	0.7	spar-filled gastropod	
γ	400.5	602.4	183.6	0.0	0.6	cemented wackestone



BOREHOLE OPZ-18

SAMPLE

OPZ-18-155.3'

OPZ-18-166.6'

OPZ-18-182.6'

OPZ-18-185.0'

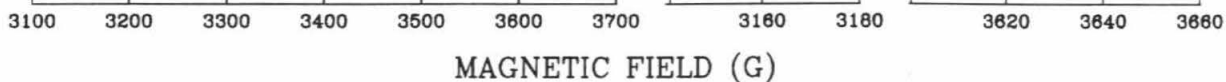
OPZ-18-198.0'

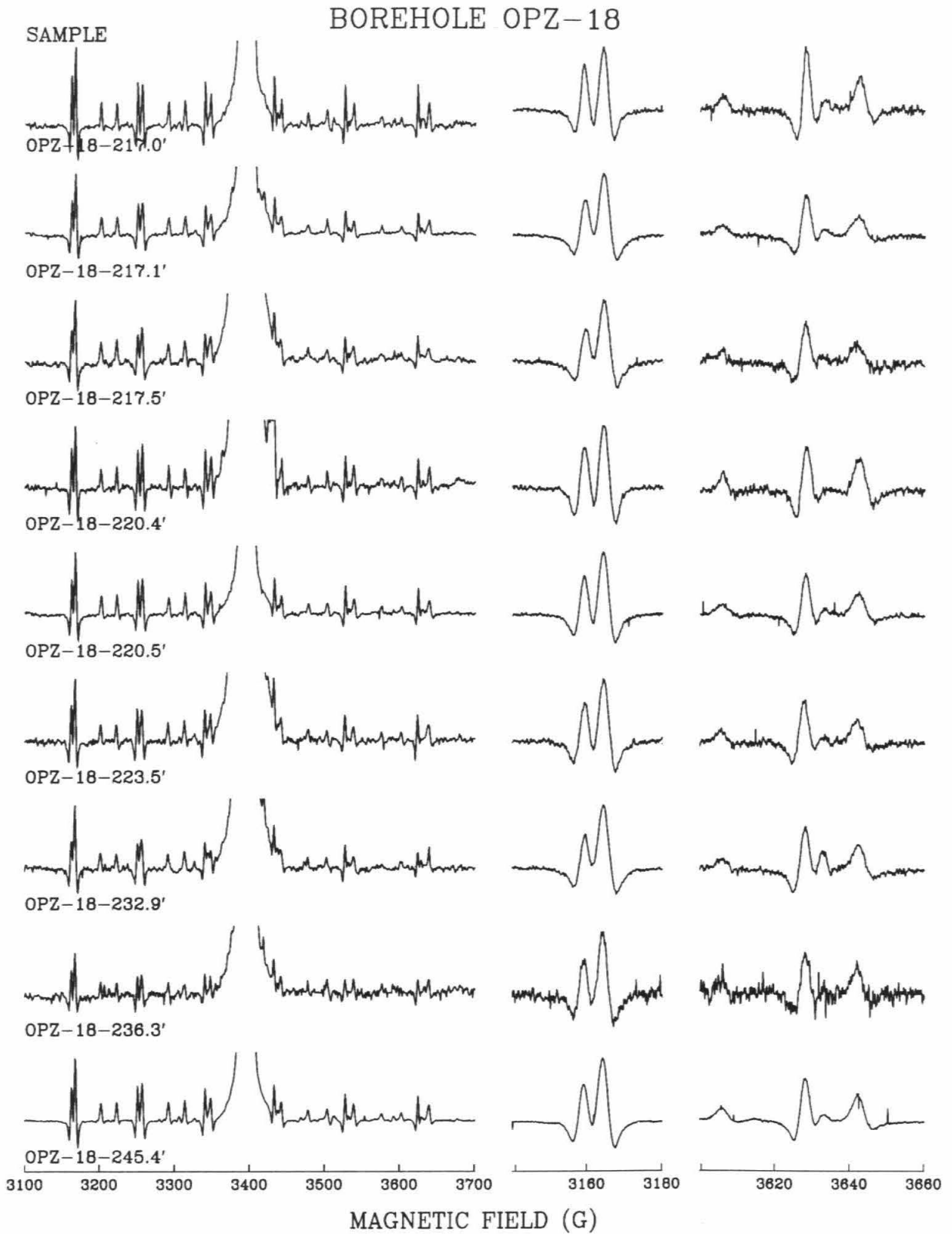
OPZ-18-198.6'

OPZ-18-207.0'

OPZ-18-210.5'

OPZ-18-214.0'





BOREHOLE OPZ-18

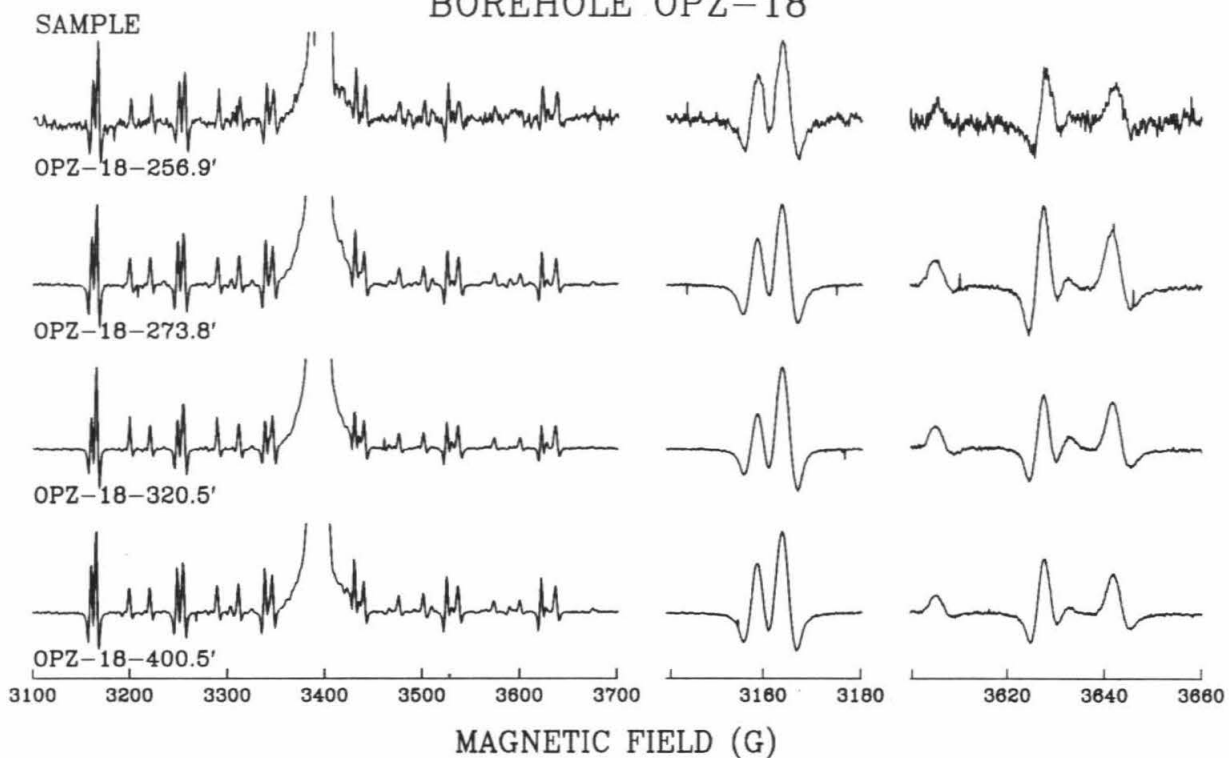
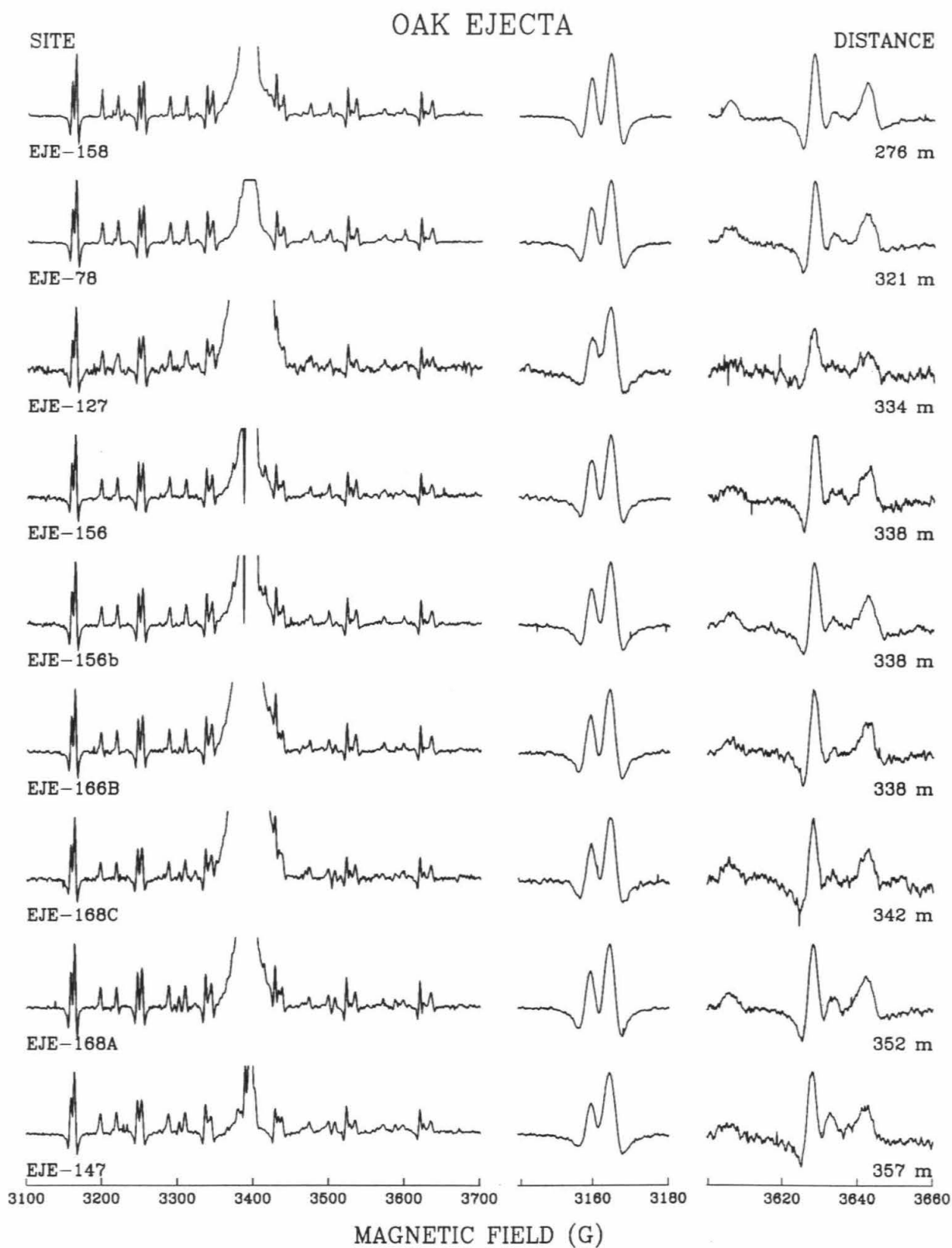


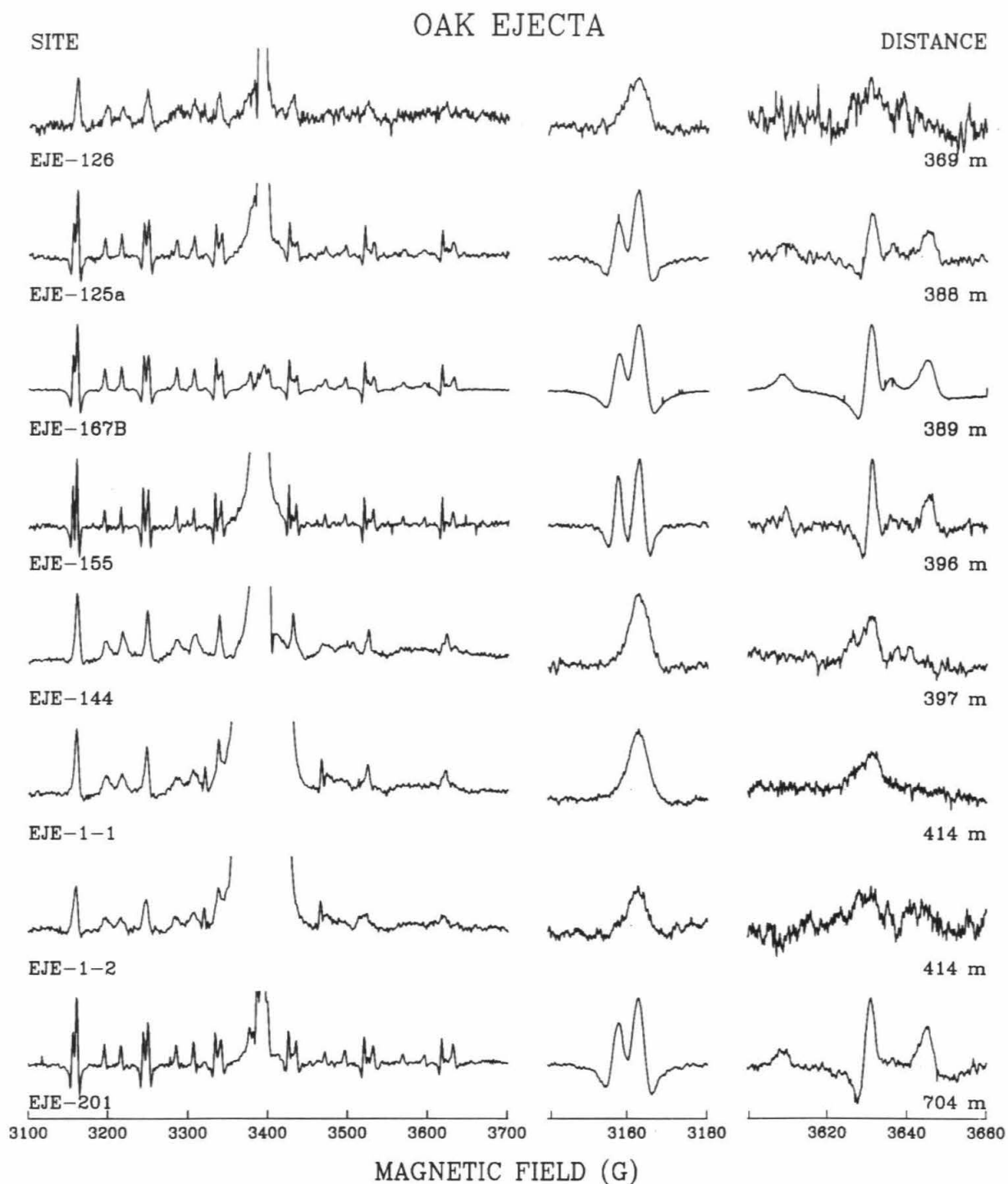
TABLE A.7

Results for OAK Debris Samples

The pressures and accompanying errors are given in Giga Pascal (GPa). Source-depths are converted to meters below sea level from Ludwig *et al.*(1986) and Ristvet (1981).

Sample	Range (m)	\pm (m)	P (GPa)	\pm (GPa)	Source- Depth (m bsl)
78	321	4	0.0	0.9	-
125a	388	4	0.0	1.8	61-150
126	369	4	13.6	4.2	32-43
127	334	4	3.0	2.0	-
128	433	4	10.5	8.0	32-43
144	397	4	12.5	2.3	32-43
147	357	9	2.7	0.9	-
155	396	4	0.0	1.4	-
156	338	4	0.0	1.1	-
156b	338	4	0.0	0.9	-
158	276	4	0.0	1.0	61-150
166B	338	4	0.0	1.0	150-210
167B	389	4	0.0	0.6	-
168A	352	4	0.0	0.8	-
168C	342	4	0.0	1.4	91-150
201	704	5	0.0	1.4	130
1-1	414	48	13.1	1.6	32-43
1-2	414	48	15.0	3.4	>43
1-3	414	48	14.6	1.6	32-43





Appendix B

Meteor Crater Sample Descriptions, Results, and Spectra

TABLE B.1

Results for Diablo Canyon Samples

Sample #	P (GPa)	\pm (GPa)	Description
1	0.0	0.03	mid α member - near surface
2	0.1	0.01	lower α member
3	0.0	0.05	upper β member - near contact to α member
4	0.0	0.01	mid β member - 30 ft into member
5	0.0	0.03	60-70 ft into β member

DIABLO CANYON SAMPLES

DESCRIPTION

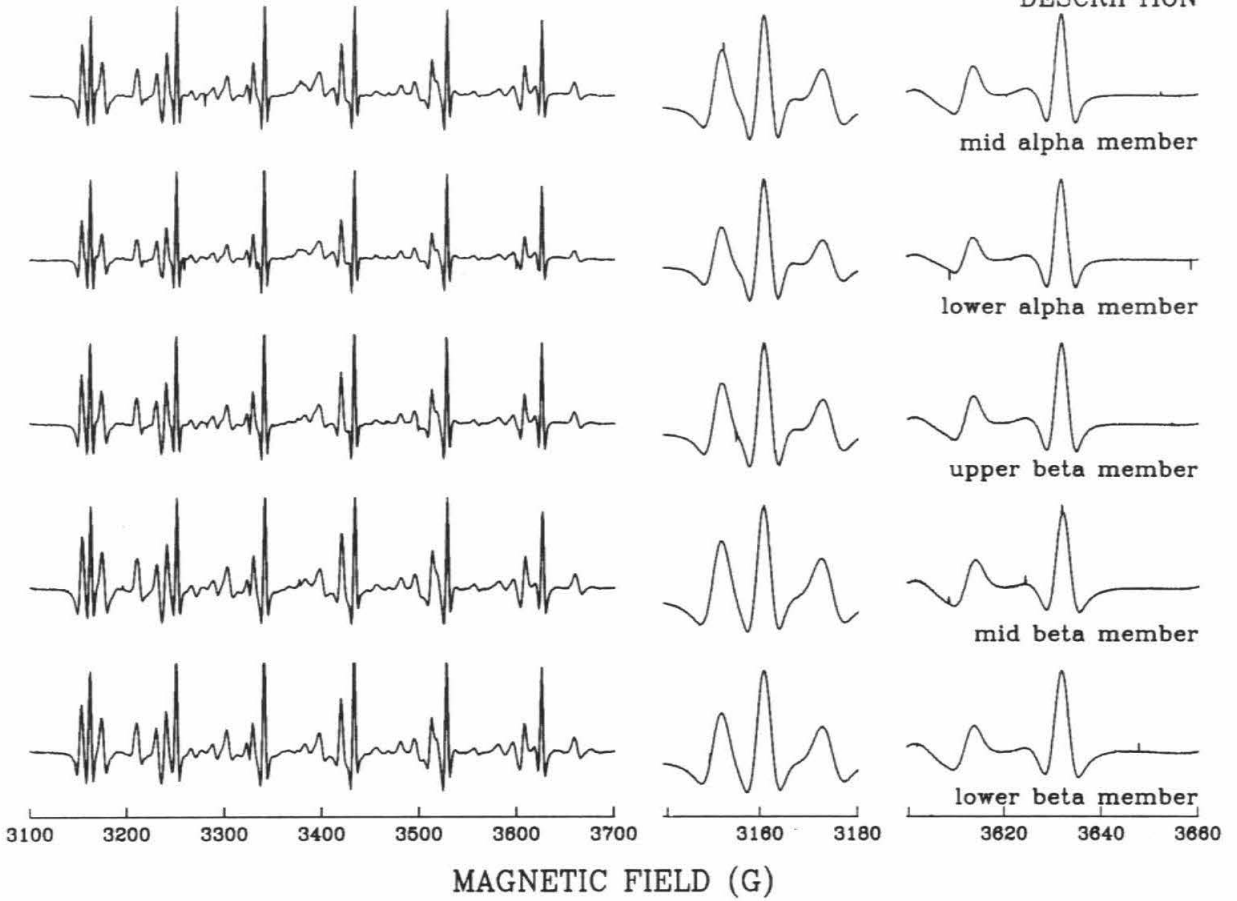


TABLE B.2

Results for Meteor Crater Wall Samples

Sample #	P (GPa)	\pm (GPa)	Description
1	0.0	0.02	uppermost α member - contact Kaibab/Moenkopi
2	0.0	0.02	upper α member - below yellow vuggy dolomite
3	0.1	0.02	lower α member - below breccia
4	0.3	0.04	uppermost β member - above promontory
5	0.5	0.06	upper β member - above promontory
6	0.6	0.08	lower β member - near promontory
7	0.4	0.05	lower β member - near Astronaut trail
8	0.1	0.02	γ member - base of promontory

METEOR CRATER WALL

UNIT

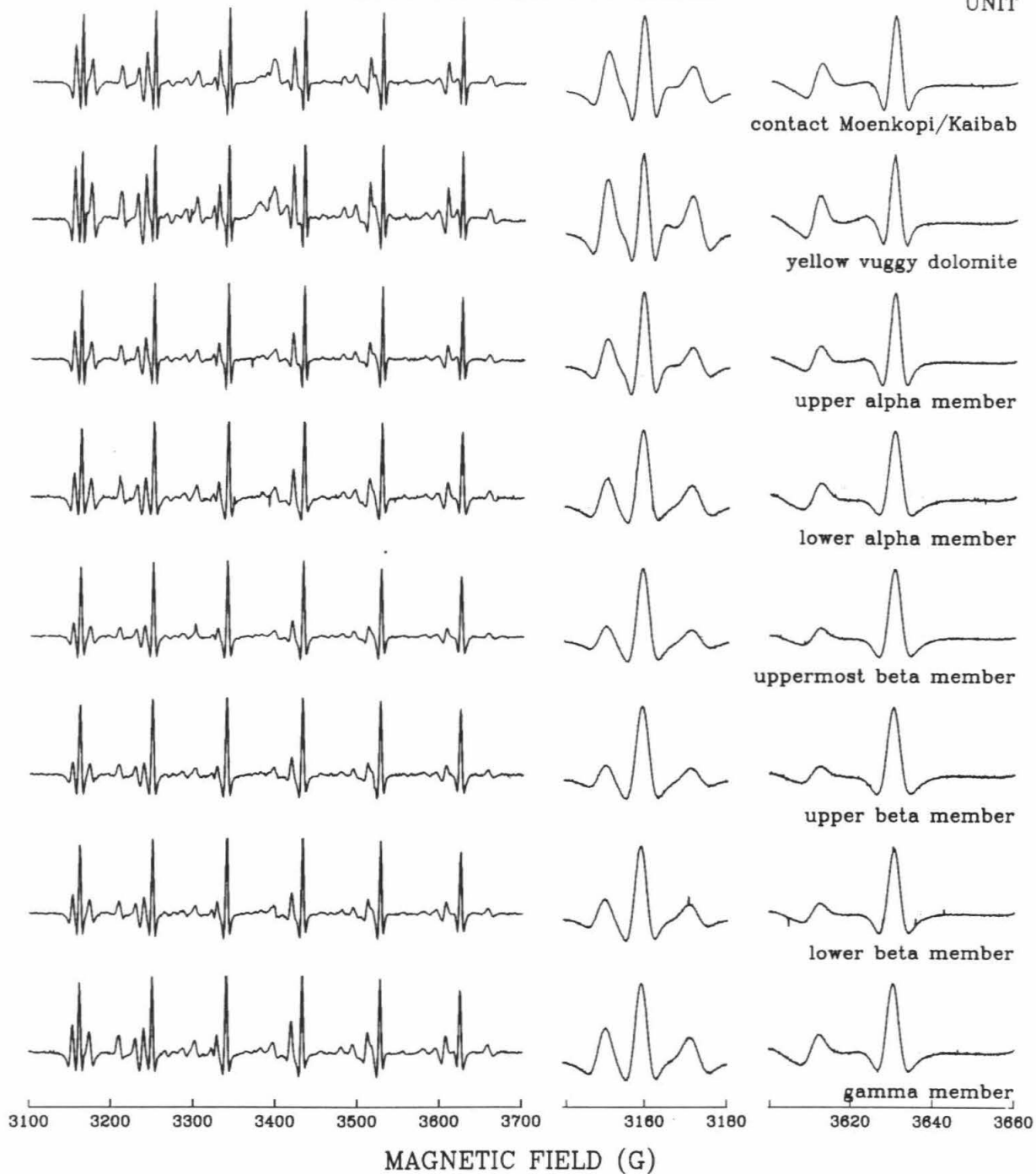
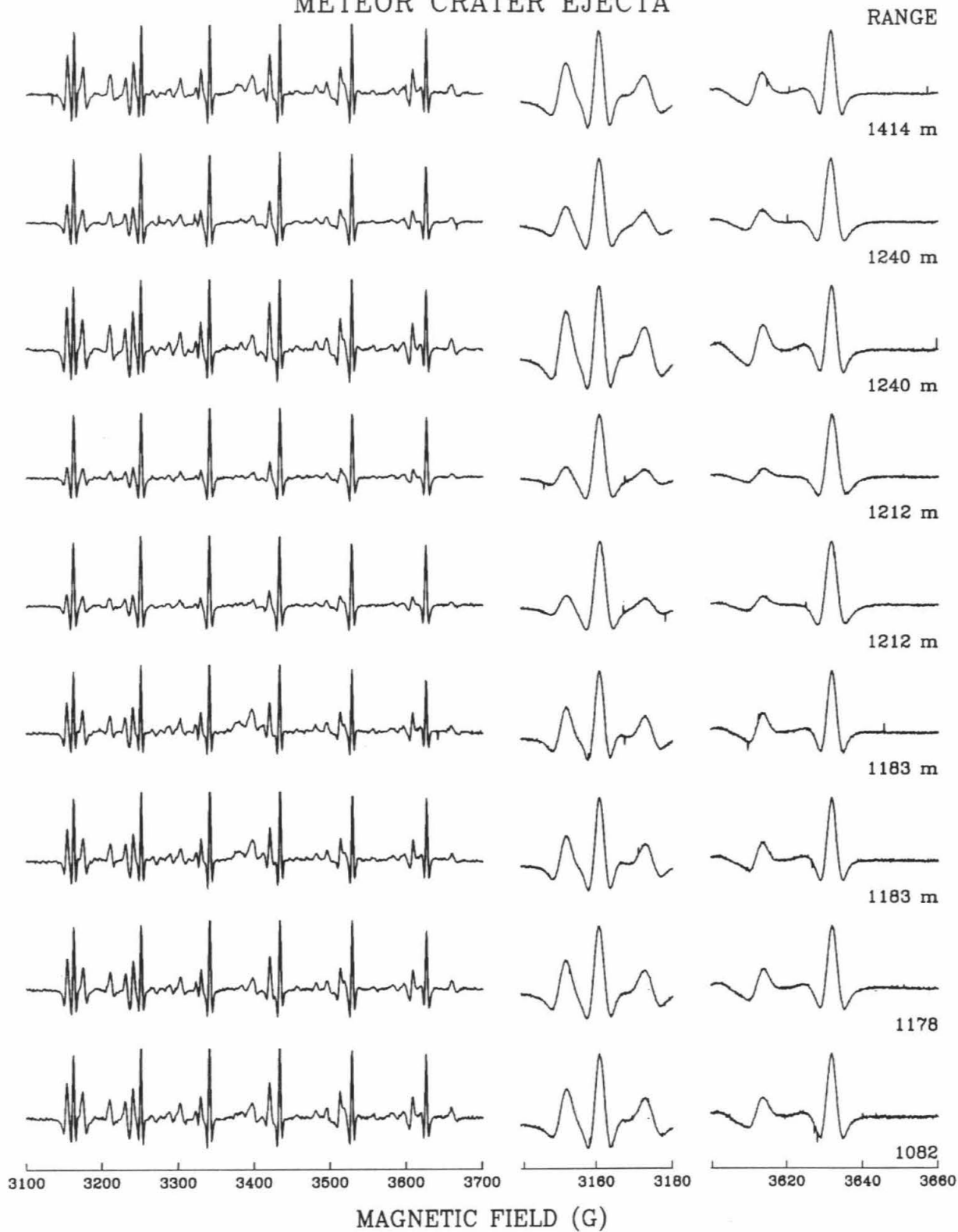


TABLE B.3

Results for Meteor Crater Ejecta Samples

Sample #	P (GPa)	\pm (GPa)	Range (m)
1	0.0	0.04	1414
2	0.3	0.04	1240
3	0.0	0.07	1240
4	0.5	0.08	1212
5	0.1	0.02	1183
6	0.0	0.07	1178
7	0.0	0.06	1082
8A	0.0	0.06	928
8B	0.1	0.04	928
9	0.0	0.01	350
10	0.4	0.08	284
11	0.6	0.05	140

METEOR CRATER EJECTA



METEOR CRATER EJECTA

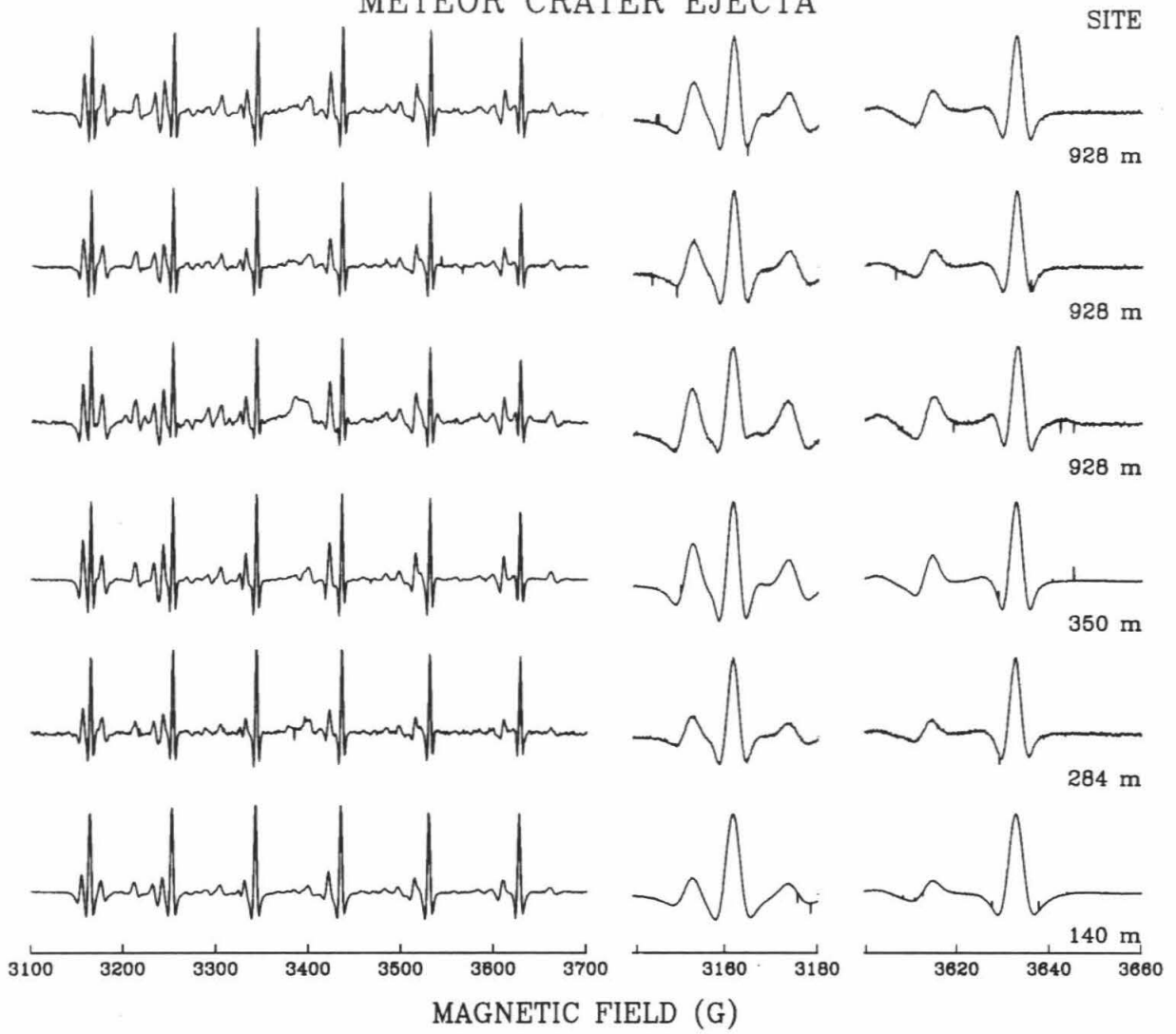


TABLE B.4

Results for Miscellaneous Meteor Crater Samples

Sample #	P (GPa)	\pm (GPa)	Description
1	0.7	0.09	<i>in-situ</i> breccia
2	0.5	0.05	relocated breccia
3A	1.0	0.14	stream redeposited highly shocked ejecta
3B	1.1	0.14	stream redeposited highly shocked ejecta
3C	1.0	0.14	stream redeposited highly shocked ejecta
3D	1.1	0.17	stream redeposited highly shocked ejecta
3E	1.1	0.16	stream redeposited highly shocked ejecta
4	—	—	caliche
5	—	—	melted ejecta sample (200 m from crater rim)

ADDITIONAL METEOR CRATER SAMPLES DESCRIPTION

